

A STUDY OF THE REACTIONS $\bar{p}p \rightarrow \pi^+\pi^-$ AND
 $\bar{p}p \rightarrow k^+k^-$ FROM 0.7 TO 2.4 GeV/c

Thesis by

Howard White Nicholson, Jr.

In partial fulfillment of the requirements
for the Degree of
Doctor of Philosophy

California Institute of Technology
Pasadena, California
1971

(Submitted 18 January, 1971)

ACKNOWLEDGMENTS

The author wishes to thank his advisor Professor Barry Barish for advice and encouragement. The author also wishes to thank Professors Alvin V. Tollestrup and Jerome Pine for their assistance during and after the running of the experiment.

The author is also indebted to the other members of the collaboration involved with the experiment. These include Drs. J.K. Yoh of CERN, Robert H. Phillips of SLAC, Claude Delorme of the University of Madagascar, Fred Lobkowitz and Adrian C. Melissinos of the University of Rochester, Alan S. Carroll of Brookhaven National Laboratory, and Yori Nagashima of Caltech.

The author also wishes to thank the support personnel of the three institutions, in particular Messrs William Friedler and Hans Grau of Caltech and Jack Sanders of the University of Rochester. The aid and support from the BNL computer center staff and the AGS EAO group are also gratefully acknowledged.

This research was supported by the U.S. Atomic Energy Commission.

ABSTRACT

Differential cross sections for the annihilation reactions $\bar{p}p \rightarrow \pi^+\pi^-$ and $\bar{p}p \rightarrow k^+k^-$ have been measured in the angular region $0.65 \lesssim |\cos \theta_{\text{cm}}| \lesssim 1.0$ at 14 incident antiproton momenta at intervals of approximately .1 GeV/c between 0.7 and 2.4 GeV/c. In the angular region $.90 \leq |\cos \theta_{\text{cm}}| \leq 1.00$ the forward going particle traversed a magnet and the differential cross sections for its charge sign could be measured. In the remaining angular region only the folded cross sections $[d\sigma/d\Omega(\theta_{\text{cm}}) + d\sigma/d\Omega(\pi - \theta_{\text{cm}})]$ could be obtained. The data which, when binned in $\cos \theta_{\text{cm}}$ bins which varied between .02 and .05 gave differential cross sections with statistical errors between 10 and 30%, were obtained in a counter experiment at the Alternating Gradient Synchrotron of the Brookhaven National Laboratory during the fall and winter of 1968.

At extreme angles the two pion annihilations show considerable structure, while the two kaon annihilations fall approximately exponentially. Between 0.7 and 1.34 GeV/c the positive meson has a larger cross section for moving in the \bar{p} beam direction; between 1.34 and 2.40 GeV/c the situation reverses. The data from this experiment have been combined with the data from a previous Caltech experiment to give complete folded angular distributions and total annihilation cross sections at 12 momenta. The folded pion cross sections show dramatic energy dependence changing from a single dipped distribution at low momenta to a doubled dipped distribution at the higher momenta. The folded two kaon cross sections also

show considerable energy dependence but its distribution remains predominately single peaked over the momentum range of this experiment.

The folded two pion annihilation data have been fit by a simple resonance model with two resonances. The two kaon data have been interpreted in terms of particle exchanges.

TABLE OF CONTENTS

	<u>Page</u>
Acknowledgments	ii
Abstract	iii
List of Tables	vii
List of Figures	ix
CHAPTER I Introduction	1
CHAPTER II Experimental Apparatus	13
Introduction	13
1. The Beam	16
2. The Target	30
3. The Bending Magnet	31
4. Trigger Logic	34
5. The Wire Spark Chambers	41
6. Over-all Timing, the Interface and the PDP-8 Computer	51
7. Monitoring the Experiment	56
CHAPTER III Analysis of the Data	61
Introduction	61
1. The Reconstruction Procedure	62
2. Event Determination	66
3. The Detection Efficiency of the Apparatus	76
4. Systematic Corrections	79
5. Cross Section Calculation	86
CHAPTER IV Results	90

	<u>Page</u>
CHAPTER V	135
Discussion of the Results	135
Introduction	135
1. Resonance and background interpretation of the folded data.	136
2. Comparison of the Extreme Angle Annihi- lation Data with πp - and $k p$ Backward Scattering Data Using Crossing Relations	160
3. Conclusions	165
APPENDIX A	169
The Beam Transport System	169
APPENDIX B	172
The Wire Spark Chambers	172
B-1. Memory Time and D.C. Clearing Field	172
B-2. Recovery Time	173
B-3. Spark Formation and Track Resolution	173
B-4. Two Track Resolution	174
APPENDIX C	176
PDP-8 Wire Spark Chamber Efficiency Calculations	176
APPENDIX D	177
The Wire Spark Chamber Efficiency Calculation	177
APPENDIX E	181
Annihilation Reaction Asymmetry Produced by a Polarized Proton Target	181
APPENDIX F	184
Notation	184
FOOTNOTES AND REFERENCES	186

	<u>List of Tables</u>	<u>Page</u>
Table 2.1	Beam fluxes and rates.	22
Table 2.2	Sizes and position of beam counters.	29
Table 2.3	Sizes and positions of trigger counters.	39
Table 2.4	Sizes and positions of the sensitive areas of the wire spark chambers.	47
Table 2.5	Wire spark chamber event efficiencies.	59
Table 2.6	Scintillation counter efficiencies.	60
Table 3.1	Beam absorption corrections.	83
Table 3.2	Nuclear interaction corrections.	85
Table 3.3	Uncertainty in normalization.	88
Table 4.1	Pion data.	94
Table 4.2	Kaon data.	108
Table 4.3	Pion Legendre expansion coefficients.	124
Table 4.4	Kaon Legendre expansion coefficients.	125
Table 4.5	Pion extreme angle differential cross sections.	128
Table 4.6	Kaon extreme angle differential cross sections.	129
Table 4.7	Total cross section for the reactions $\bar{p}p \rightarrow \pi^+\pi^-$ and $\bar{p}p \rightarrow k^+k^-$ from other experiments.	134
Table 5.1	Resonance parameters of reported $B = 0$ structures between 1990 and 2570 MeV.	153
Table 5.2	Isotopic spin decomposition.	154
Table 5.3	$\bar{p}p \rightarrow 2\pi^0$ Data.	155
Table 5.4	Resonance parameters of best fits to $\pi\pi$ annihilation data.	156

	<u>Page</u>
Table 5.5 Minimum antiproton momenta required to produce an angular momentum ℓ as a function of proton scattering radius R_s (in units of 10^{-15} m).	157

	<u>List of Figures</u>	<u>Page</u>
Figure 1.1a	Direct (s) channel resonance formation for the $\bar{p}p \rightarrow \bar{\pi}\pi$, $\bar{p}p \rightarrow \bar{k}k$, $\pi p \rightarrow \pi p$, $kp \rightarrow kp$.	8
Figure 1.1b	Exchange diagrams for the four pairs of backward scattering and annihilation reactions.	9
Figure 1.2a	Angular distribution for the reactions $\bar{p}p \rightarrow \pi^+\pi^-$ and $\bar{p}p \rightarrow k^+k^-$ as a function of the center of mass angle between the incident antiproton and outgoing negative track.	10
Figure 1.2b	Differential cross section for $\bar{p}p \rightarrow \pi^+\pi^-$ based on the sum of the data in Figure 1.2a.	11
Figure 1.3	Total cross sections for $\bar{p}p \rightarrow \pi^+\pi^-$ and $\bar{p}p \rightarrow k^+k^-$ between 350 and 600 GeV/c incident antiproton momentum.	12
Figure 2.1	Layout of the apparatus.	15
Figure 2.2	Layout of the separated beam transport system.	21
Figure 2.3	Schematic drawing of the beam liquid differential Čerenkov counter.	23
Figure 2.4	(a) % of Čerenkov coincident vs. diaphragm mirror position. (b) % of beam time-of-flight coincidence vs. time-of-flight delay.	24
Figure 2.5	Diagram of Čerenkov counter and time-of-flight logic.	25

Figure 2.6	Momentum distribution of incident \bar{p} 's at 2.0 GeV/c nominal momentum for (a) \bar{p} 's hitting a particular mass slit counter (b) all \bar{p} 's (c) all \bar{p} 's corrected according to which mass slit counter it hits.	26
Figure 2.7	Distribution of momentum, positions, and slopes of the incident \bar{p} beam.	27
Figure 2.8	Rectangular field model for a dipole magnet.	33
Figure 2.9	Flow diagram of trigger logic.	37
Figure 2.10	Horizontal and vertical distribution of sparks in wire spark chambers 1-8 for straight tracks.	48
Figure 2.11	Schematic of the operation and components of the wire spark chambers.	49
Figure 2.12	The wire spark chamber signals and the digitizer operation.	50
Figure 2.13	Trigger and event recording timing diagram.	54
Figure 3.1	Coplanarity distribution.	71
Figure 3.2	Z vertex distribution.	72
Figure 3.3	Mass squared distribution of final state particles. Events plus background.	73
Figure 3.4	Mass squared distribution of final state particles. Background.	74
Figure 3.5	Mass squared distribution for final state particles. Background subtracted.	75

	<u>Page</u>	
Figure 3.6	Solid angle acceptance of experimental apparatus.	78
Figure 3.7	Flow chart of analysis procedure.	89
Figure 4.1	Folded pion cross sections with Legendre fit.	122
Figure 4.2	Folded kaon cross sections with Legendre fit.	123
Figure 4.3	Pion and kaon total cross sections.	126
Figure 4.4	Pion and kaon Legendre expansion coefficients.	127
Figure 4.5	Pion extreme angle $d\sigma/d\Omega$.	130
Figure 4.6	Kaon extreme angle $d\sigma/d\Omega$.	131
Figure 4.7	Pion extreme angle $d\sigma/du$.	132
Figure 4.8	Kaon extreme angle $d\sigma/du$.	133
Figure 5.1	Pion total cross section times antiproton center-of-mass momentum squared.	148
Figure 5.2	Kaon total cross section times antiproton center-of-mass momentum squared.	149
Figure 5.3	Resonance fit to pion folded differential cross sections.	150
Figure 5.4	Resonance fit to pion total cross sections.	151
Figure 5.5	Resonance fit to Legendre expansion coefficients.	152
Figure 5.6	Expected mass states of the $q\bar{q}$ model plotted against a) J, b) L, and c) allowed decay modes.	158
Figure 5.7	Angular momentum barrier for the a) $\bar{p}p$, and b) πN system.	159

	<u>Page</u>
Figure 5.8 Comparison of annihilation and backward scattering reactions at extreme angles as a function of s .	163
Figure 5.9 Comparison of annihilation and backward scattering reactions at extreme angles as a function of u .	164
Figure A.1 Ray traces of the trajectories of extreme angle particles passing through the beam transport system.	171

Chapter I

INTRODUCTION

One of the more interesting phenomena of experimental high energy physics is the large number of short-lived particles or resonances currently being discovered in reactions involving strongly interacting particles at high energy particle accelerators throughout the world. At present no classification schemes exist for all the experimentally established resonances although a number of regularities in the masses and quantum numbers of many of these resonances have been discovered by the application of unitary symmetry to the resonance spectrum (as in the quark model of Gell-Mann and Zweig). Furthermore, no satisfactory theory exists of the dynamics of reactions involving strongly interacting particles and resonances and many of the fundamental principles of strong interaction theories have so far proved useful only in finding relationships between reactions involving different types of particles.

Although many resonances of mass < 2.0 GeV have been discovered and studied experimentally, previous limitations on beam energies and fluxes have made it difficult to search for resonances of mass > 2.0 GeV. Recently, however, high flux antiproton beams have been built at CERN and Brookhaven Labs and have been used as an effective means for searching for boson resonances with masses > 2.0 GeV.

This thesis reports on the results of a counter experiment performed at Brookhaven National Laboratory in 1968. Antiprotons with momenta between 0.7 and 2.4 GeV/c produced in the Brookhaven

AGS annihilated protons in a liquid hydrogen target producing occasional two charged pi meson or two charged k meson final states. Wire chambers were used to measure the laboratory angular distributions of the two final state mesons.

These data were used to obtain cross sections for the two anti-proton-proton annihilation reactions

$$\bar{p} + p \rightarrow \pi^+ + \pi^- \quad (1.1a)$$

$$\bar{p} + p \rightarrow k^+ + k^- \quad (1.1b)$$

in the angular region $0.65 < |\cos \theta_{cm}| < 1.0$ at 14 momenta between 0.7 and 2.4 GeV/c. These cross sections, combined with those of Fong et al.¹⁾ for $|\cos \theta_{cm}| \leq 0.70$ give complete folded²⁾ angular distributions for 12 momenta in this momentum range. In addition, in the angular region $0.90 < |\cos \theta_{cm}| < 1.0$ the forward going particle traversed a bending magnet and the sign of its charge could be determined.

The cross section of these reactions are of interest for two principle reasons. First, the proton-antiproton annihilation channel with its high center of mass energy (1.88 GeV at threshold) provides a way to search for high mass boson resonances in the vicinity of the S, T, and U resonances reported by the CERN missing mass spectrometer group³⁾. Second, previous cross section measurements of the elastic scattering reactions

$$\pi^\pm + p \rightarrow \pi^\pm + p \quad (1.2a)$$

$$k^\pm + p \rightarrow k^\pm + p \quad (1.2b)$$

in the forward and backward directions⁴⁾ can be compared to the annihilation reaction cross sections in the forward and backward

directions to test such fundamental theoretical principals of strong interaction theories as crossing symmetry and line reversal.

Figure 1.1 gives the Feynman diagrams for reactions 1 and 2. Groups at Brookhaven Lab (Abrams et al.⁵⁾, Anderson et al.⁶⁾, CERN⁷⁾, and Michigan⁸⁾ have reported many $B = 0$ structures of masses between 1990 and 2570 MeV which may be candidates for s channel resonances in the annihilation reactions (1.1a,b). Some of these such as the bumps in the $\bar{p}p$ total cross section reported by Abrams et al. have widths of 140 MeV while the S, T, and U structures in the missing mass spectrum of the reaction $\pi^-\bar{p} \rightarrow pX^-$ reported by the CERN group have widths less than 35 MeV.

The broad structures in the $\bar{p}p$ total cross section measurements reported by Abrams may not indicate resonances; they may also be interpreted as inelastic threshold effects. For example, the structure reported at 2190 MeV could be interpreted as an effect of the threshold in $\Delta(1236)$ or $\bar{\Delta}(1236)$ production and the structures reported at 2350 and 2380 MeV may both be due to $N^*(1400)$ or $\bar{N}^*(1400)$ production⁹⁾. On the other hand, narrow structures or enhancements in the total cross section of a particular channel would be expected to be resonances. Differential and total cross section data for $pp \rightarrow \bar{\pi}\pi$ and $\bar{p}p \rightarrow \bar{k}k$ over a range of total center-of-mass energy between 1990 and 2570 MeV help to determine which of the above structures, if any, can be interpreted as direct channel $I = 0$ or 1 meson resonances in these reactions or whether other heavy mass meson resonances are needed to explain the data.

Since the antinucleon-nucleon ($\bar{N}N$) system is an $I = 0$ or $I = 1$ system and the space symmetry of the antimeson-meson system ($\bar{M}M$) is $(-1)^J$ where J is the total spin, structures which could be s channel resonances in the reaction $\bar{N}N \rightarrow \bar{M}M$ have $I = 0$ with even J or $I = 1$ with odd J . The J of those structures which strongly couple to the $\bar{p}p$ system along with whatever new structures are found can be studied using the combined differential cross section data of this experiment and the one of Fong et al. When J can be found, the parity and I spin quantum numbers P and I of the structures are determined as well.

Figure (1.1b) shows how the amplitude for the backward elastic scattering reaction $MN \rightarrow MN$ can be related via crossing symmetry and the assumption of dominant u channel exchanges to the amplitude for the annihilation reaction $\bar{N}N \rightarrow \bar{M}M$. With the usual definitions

$$s = (p_1 + p_2)^2 = (p_3 + p_4)^2 \quad (1.3a)$$

$$t = (p_1 - p_4)^2 = (p_2 - p_3)^2 \quad (1.3b)$$

$$u = (p_1 - p_3)^2 = (p_2 - p_4)^2 \quad (1.3c)$$

the energy variable in the backward elastic scattering reaction s becomes t in the annihilation reaction while the u variable remains the same. At energies where a single u channel or fermion Regge pole exchange dominates the cross section, u channel amplitudes in the backward elastic scattering reaction can be used to obtain the u channel amplitudes in the annihilation reaction by making the replacement $z_u \rightarrow -z_u$ where $z_u = \cos \theta_u$.

In the limit of infinite energy Van Hove has shown by an

extension of the Pomeranchuk theorem that the s channel amplitude in elastic scattering becomes equal to the u channel amplitude¹⁰⁾.

Assuming the annihilation cross section $d\bar{\sigma}/du$ is dominated by the same u channel exchanges as the backward scattering cross section $d\sigma/du$, the relation between them is

$$\lim_{t \rightarrow \infty} \frac{d\bar{\sigma}}{du}(t,u) = \frac{1}{2} \lim_{s \rightarrow \infty} \frac{d\sigma}{du}(s,u) \quad (1.4)$$

The factor 1/2 is the ratio of initial spin states for the meson-nucleon system to the antiproton-proton system.

In the Regge theory of fermion trajectory exchanges, the signature τ is related to the orbital angular momentum ℓ of the Legendre polynomials $P_{\ell}(\cos \theta_u)$ appearing in the amplitude before analytic continuation by $\pm (-)^{\ell}$, the sign depending on the type of trajectory exchanged. Assuming the exchange of a single Regge trajectory, the relation between the u channel annihilation amplitude $\bar{f}_1(\sqrt{u},s)$ and the u channel backward elastic scattering amplitude $f_1(\sqrt{u},s)$ is¹¹⁾

$$\bar{f}_1(\sqrt{u},s) = \tau f_1(\sqrt{u},s). \quad (1.5)$$

Equation (5) can be used to relate the backward elastic cross section to the annihilation cross section. First the differential cross section for meson-nucleon scattering is written in terms of the s-channel invariant amplitudes $f_1(\pm\sqrt{s},u)$ and the kinematic factors s and u. Crossing symmetry related these s channel amplitudes to the u channel amplitudes $f_1(\pm\sqrt{u},s)$. The annihilation u channel cross sections can then be obtained by replacing $f_1(\pm\sqrt{u},s)$ by $\bar{f}_1(\pm\sqrt{u},s)$ and s by t. The assumption of a single trajectory exchange permits the use of equation (5). Finally, the assumption that the invariant

amplitudes $f_1(\pm\sqrt{u}, s)$ are even functions of \sqrt{u} ¹²⁾ enables the annihilation cross section to be related to the backward elastic scattering cross section at all energies where a single u channel exchange dominates the amplitudes. This relation at equal energies ($t = s$) is

$$\frac{d\bar{\sigma}}{du} = \frac{1}{2} \frac{d\sigma}{du} \frac{[s - (M + \mu)^2][s - (M - \mu)^2]}{s[s + 2D^2]} \quad (1.6)$$

where M is the nucleon mass, μ is the meson mass, and $D^2 = M^2 - \mu^2$. In the limit $s \rightarrow \infty$, this expression reduces to equation 1.4.

Annihilation data from this experiment can be compared to backward elastic scattering data from other experiments for $3.98 \leq S \leq 6.39$ (GeV/c)² and $u \approx 0$ to check whether the assumptions which went into the derivation of equation 1.6 are valid at these energies. Furthermore, if cross section data in the reactions $k^- p \rightarrow pk^-$ and $\bar{p} p \rightarrow k^+ k^-$ (reactions 4) satisfy equation 1.6, they could be interpreted as evidence for $S = +1$ baryon exchange (in this case the Z^{*++}) which has not previously been observed. ($S = +1$ baryons do not fit the usual quark model interpretation that baryons are made up of three quarks.)

Previously published $\bar{p} p \rightarrow \bar{M} M$ data is scanty primarily because high flux \bar{p} beams have been unavailable until recently and cross sections are small ($\sigma_{\bar{p} p \rightarrow \pi\pi}^{\text{tot}} \sim 200 \mu\text{b}$) relative to other processes which can occur ($\sigma_{\bar{p} p}^{\text{tot}} \sim 100 \text{mb}$). In 1963 Lynch¹³⁾ et al. found 20 events fitting $\bar{p} p \rightarrow \bar{\pi}\pi$ kinematics and 11 fitting $\bar{p} p \rightarrow \bar{k}k$ kinematics at incident antiproton momentum 1.61 GeV/c from the over 20,000 antiproton-proton interactions seen in the Berkeley bubble chamber.

In a 1968 bubble chamber exposure at Michigan, Chapman et al.¹⁴⁾ measured differential and total cross sections for these annihilation reactions between 1.6 and 2.2 GeV/c. Figure 1.2b is an energy averaged plot of the angular distributions. The dashed curve is a plot of the spherical harmonic $|Y_4^0|^2$. The experimenters interpreted these data as suggestive of a $J = 4$ resonance in this momentum region except for the absence of large peaks at $\cos \theta_{\text{cm}} = \pm 1$.

Total cross sections and angular distributions for the $\bar{p}p \rightarrow \bar{M}M$ reactions have also been measured between .22 and .62 GeV/c by Bizzarri et al.¹⁵⁾ A plot of the total cross sections is given in Figure 1.3.

The angular distributions for reaction (1.1a) obtained in this experiment are consistent with the Lynch data and Chapman data and are also consistent with the interpretation that the principal features of the data result from two resonances in the $\bar{p}p$ system which decay in the two charged pion channel. The resonances which best reproduce the data have masses of 2.12 and 2.29 GeV, widths of .320 and .159 GeV, and spin J of 3 and 5, respectively.

Good agreement has been found between reactions (1.1b) and (1.2b) using equation (1.6). Although the backward k^+p scattering was expected to be dominated by u-channel exchanges down to ~ 1 GeV/c,¹⁶⁾ the agreement for backward k^-p scattering does not rule out the possibility of a $S = +1$ baryon exchange. Future experiments should help to clarify the status of the $S = +1$ baryons.

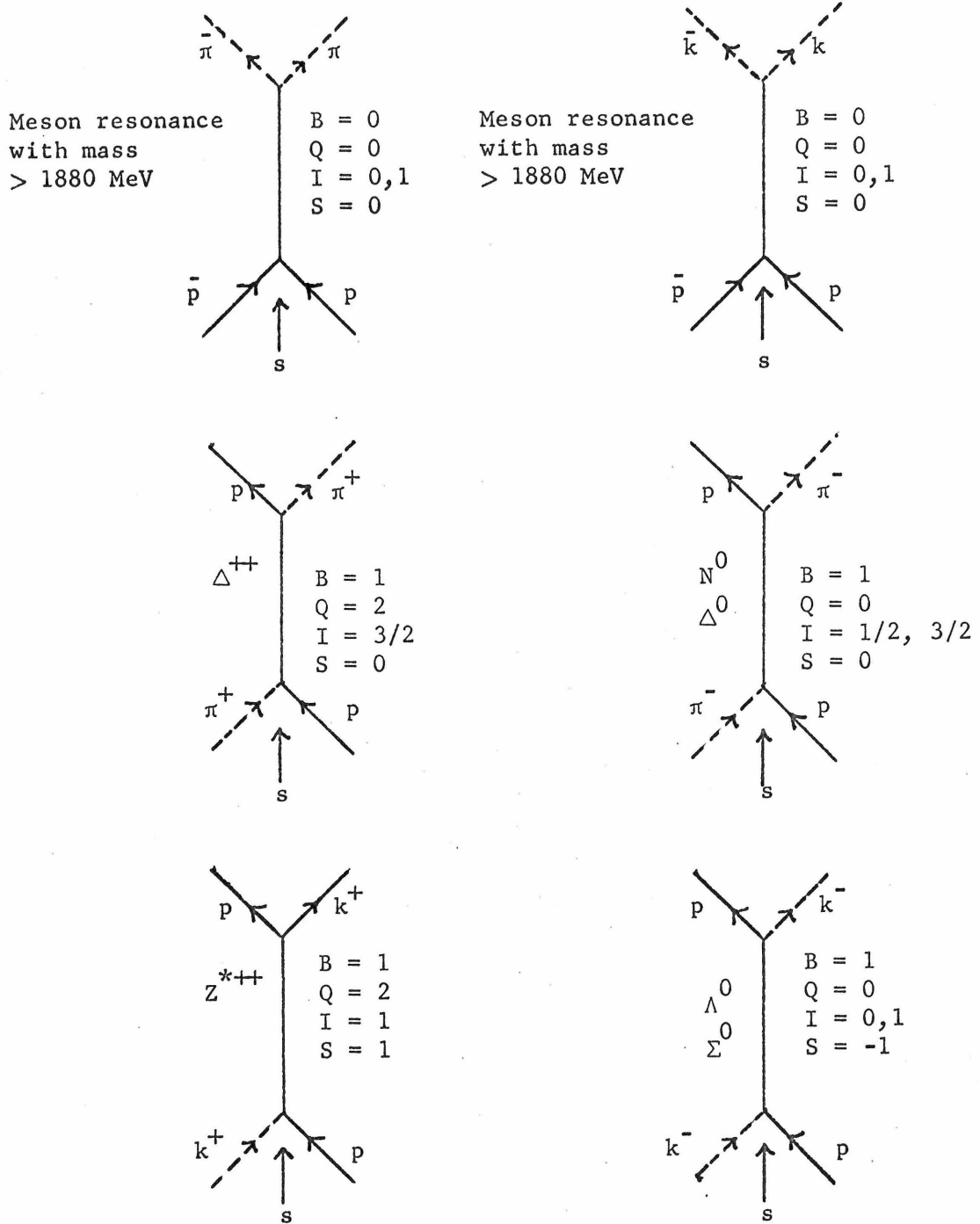


Figure 1.1a

Direct (s) channel resonance formation for the reactions $\bar{p}p \rightarrow \bar{\pi}\pi$
 $\bar{p}p \rightarrow \bar{k}k$, $\pi p \rightarrow \pi p$, $kp \rightarrow kp$.

Backward Elastic Scattering Reactions

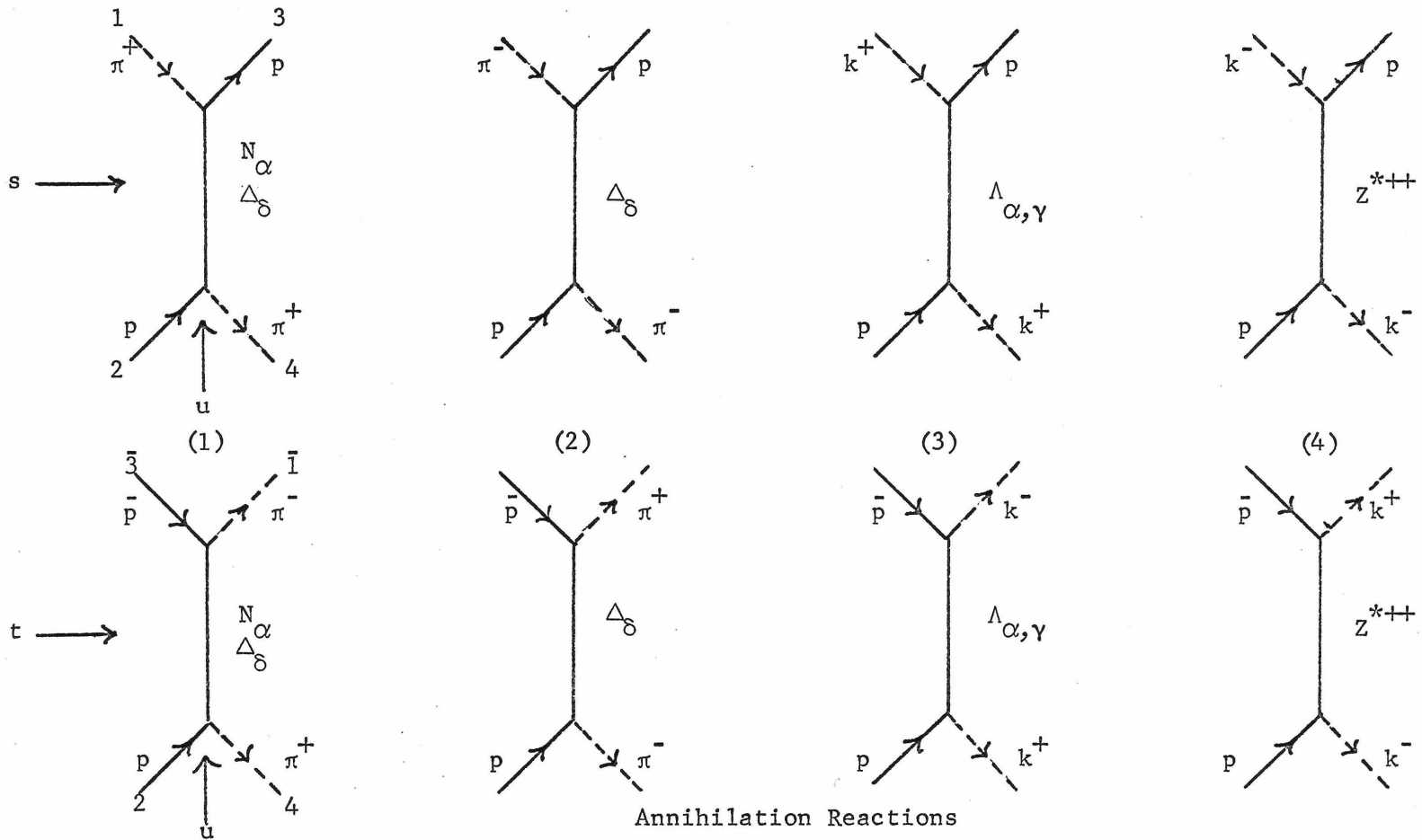


Figure 1,lb Exchange diagrams for the four pairs of backward-scattering and annihilation reactions. Reaction (1) indicates how the top two arms of the diagram are interchanged to give the s and t channels. Some of the possible exchanged baryon trajectories are included.

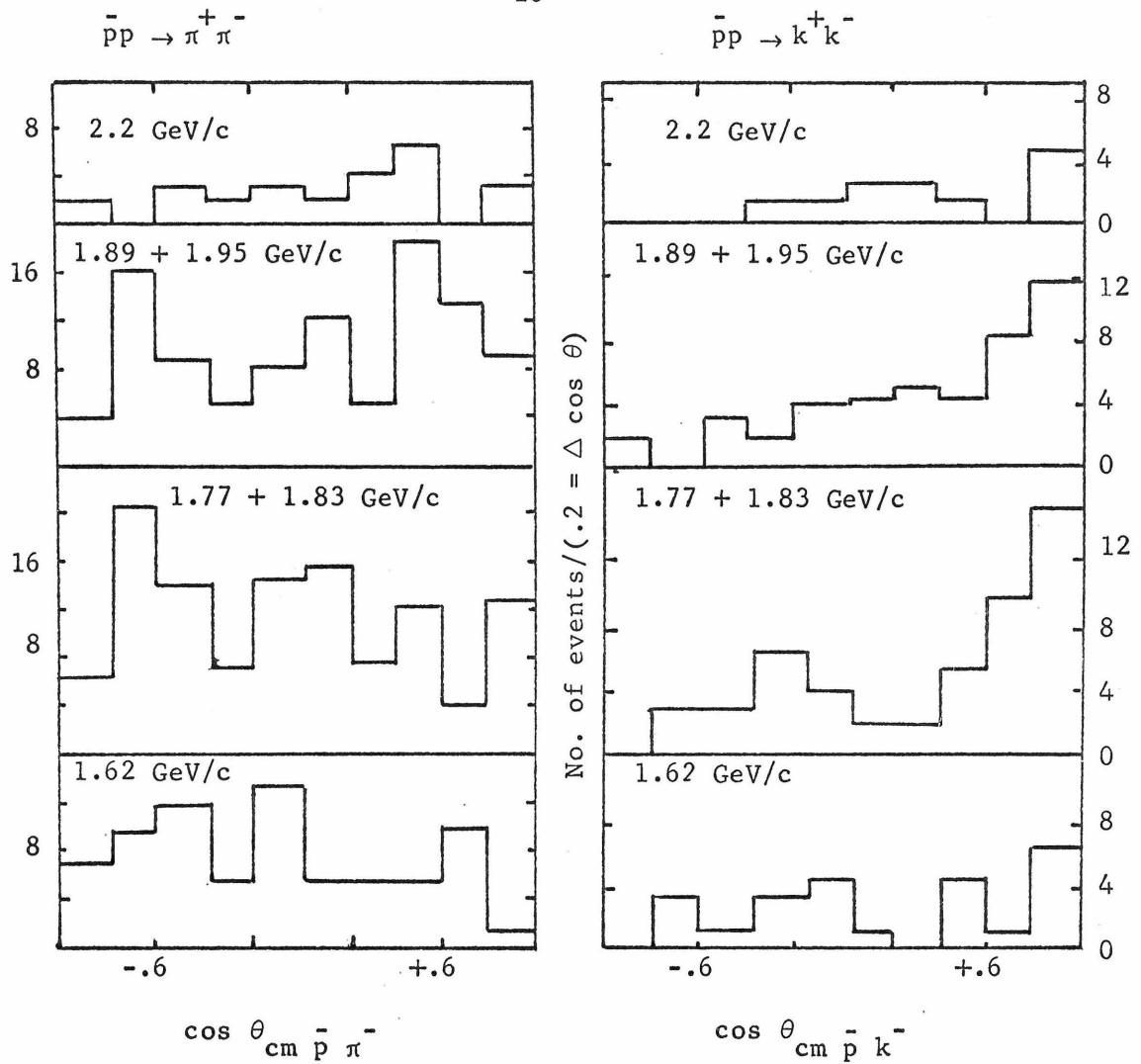


Figure 1.2a

Angular distribution for the reactions $\bar{p}p \rightarrow \pi^+ \pi^-$ and $\bar{p}p \rightarrow k^+ k^-$ as a function of the center of mass angle between the incident antiproton and outgoing negative track. From Chapman et al.¹⁴⁾

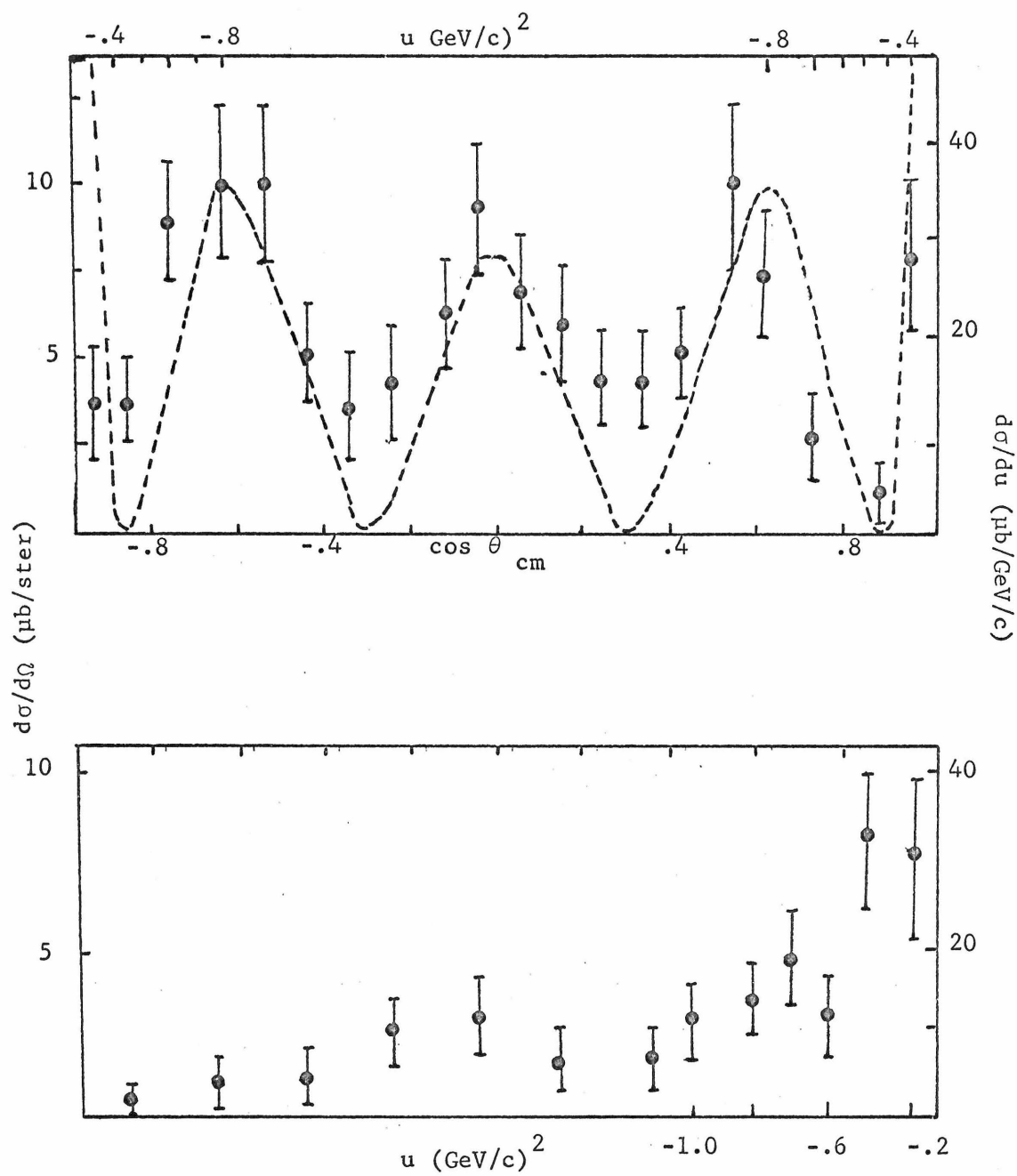


Figure 1.2b

Differential cross section for $\bar{p}p \rightarrow \pi^+\pi^-$ based on the sum of the data in Figure 1.2a. The dashed curve is the spherical harmonic $|Y_4^0|^2$.
 From Chapman et al.¹⁴⁾

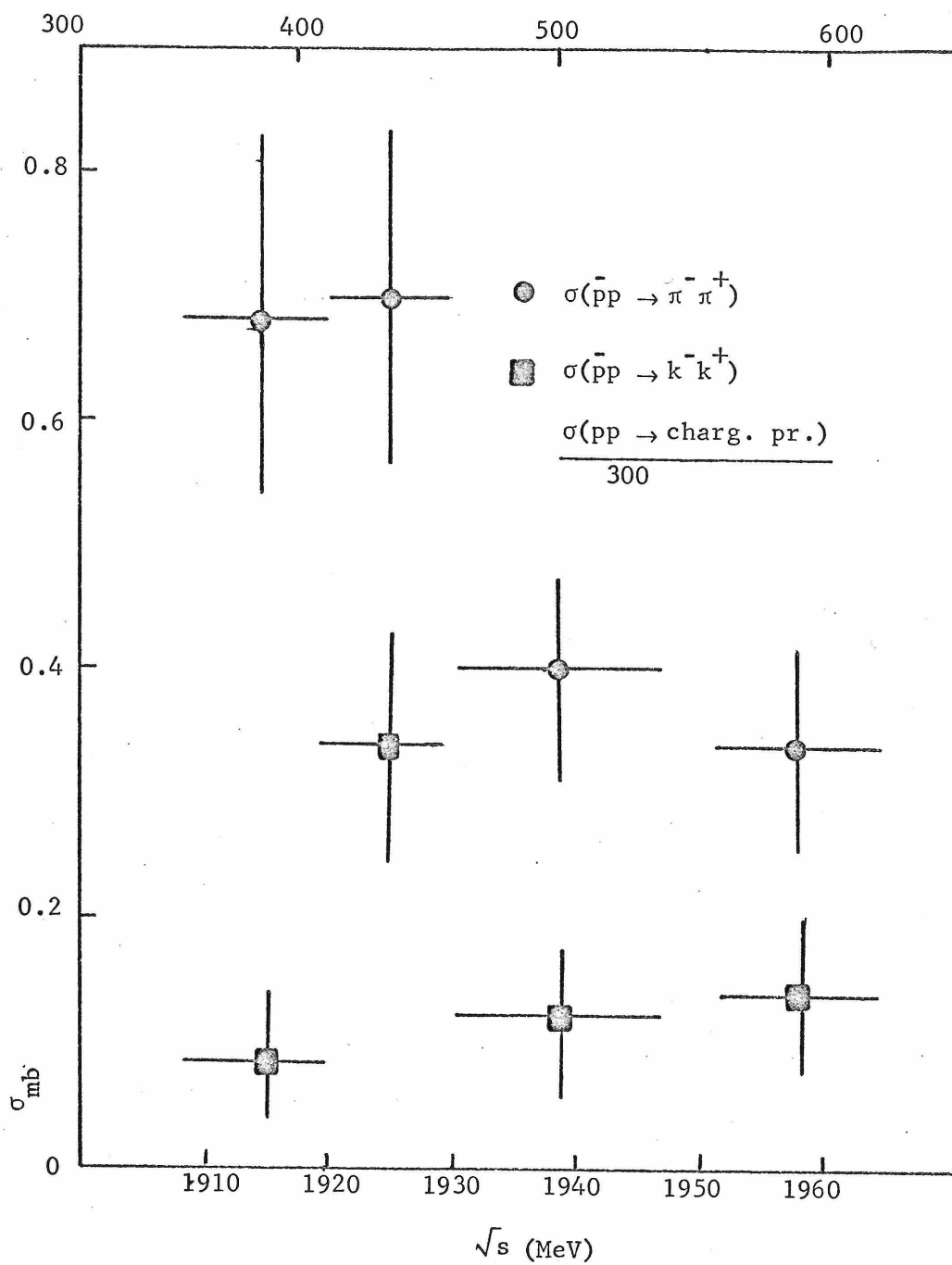
$P_{\text{lab}} (\text{MeV}/c)$ 

Figure 1.3

Total cross sections for $\bar{p}p \rightarrow \pi^+ \pi^-$ and $\bar{p}p \rightarrow k^+ k^-$ between 350 and 600 MeV/c incident antiproton momentum. (From Bizzarri et al.¹⁵)

CHAPTER II

EXPERIMENTAL APPARATUS

Introduction

In order to measure the differential cross sections for proton-antiproton annihilations into two charged mesons in a counter experiment it is necessary to have

- a) An antiproton beam with sufficient flux to measure the small cross sections.
- b) A proton or liquid hydrogen target.
- c) A fast logic or triggering circuit which discriminates against unwanted reactions and enriches the recorded data sample with events of interest.
- d) Apparatus which measures the numbers and trajectories of incoming and outgoing particles in space sufficiently accurately so angular distributions can be determined.
- e) A method for recording data for subsequent off-line analysis.
- f) A system for monitoring the experimental equipment during the actual running of the experiment.

This experiment was performed on the short branch of the partially separated branch of beam 5 of the AGS at the Brookhaven National Laboratory¹⁷⁾. The \bar{p} fluxes of this beam per machine pulse ranged between 500 \bar{p} 's at .68 GeV/c to 45000 \bar{p} 's at 2.37 GeV/c with each pulse lasting the order of .5 sec at a machine repetition rate of 25 pulses/minute. Scintillation counters arrays upstream¹⁸⁾ of

the target, downstream of the target and upstream of the bending magnet and downstream of the bending magnet were used to trigger twelve wire spark chambers, 4 in each of the above regions, which measured the positions of the incident and outgoing particles with a spacial resolution of the order of 1 mm. The wire chamber pulses were read out on magnetostrictive lines, digitized and read into a PDP-8 computer which wrote the digitized coordinate positions on magnetic tape for subsequent analysis. Data taking was divided into 30 to 120 minute time intervals called runs. At the end of each run, the PDP-8 printed out run summary data which was used to check counter and wire chamber efficiency. A diagram of the experimental apparatus is given in Figure 2.1.

This chapter and the Appendices A and B describe in detail the beam and beam transport system, the target, the bending magnet, the scalar counters, the trigger counters and fast logic, the wire chambers and wire chamber readout system, the over-all interface, and the PDP-8 computer data recording and data monitoring system.

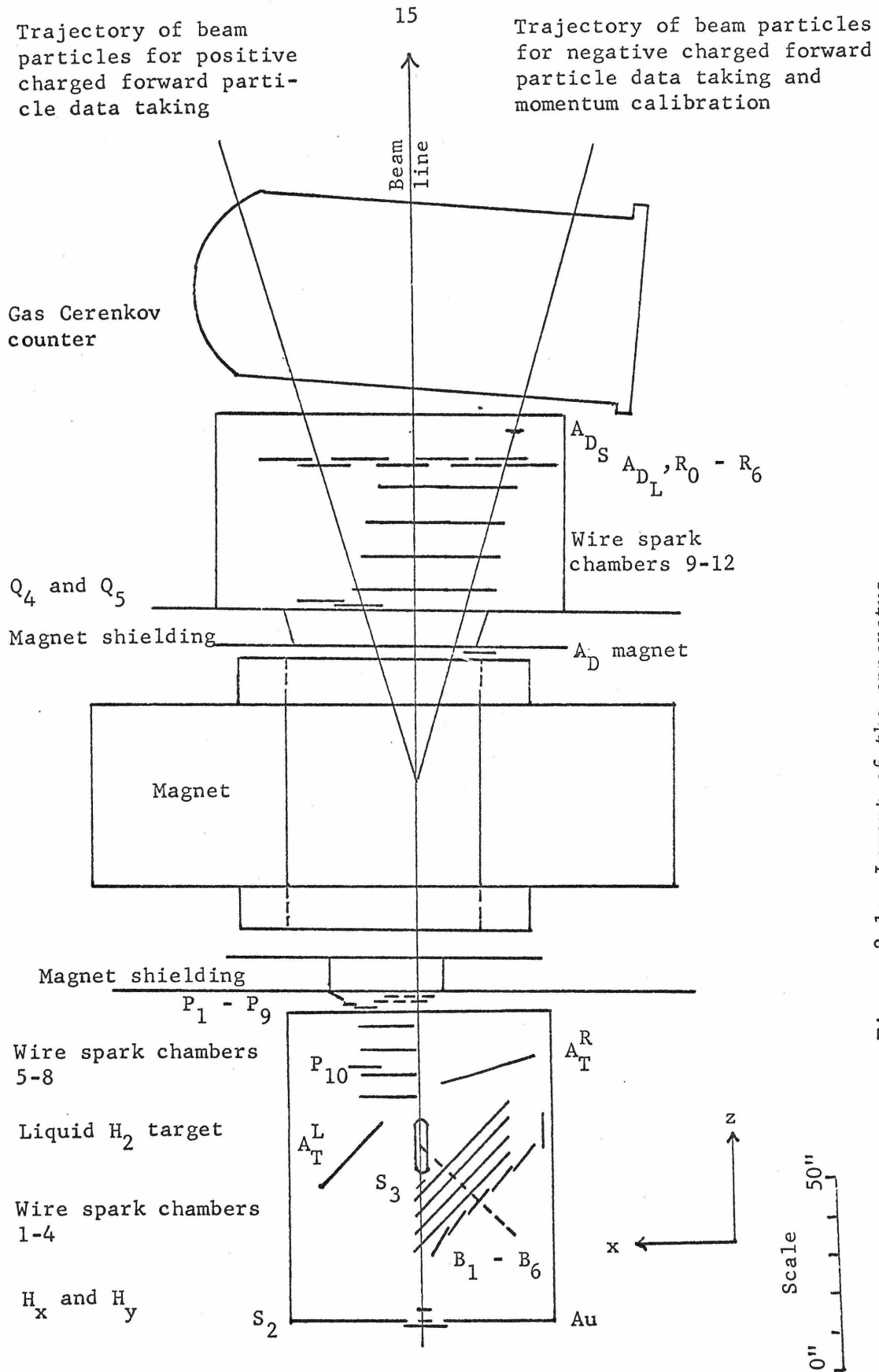


Figure 2.1: Layout of the apparatus

1. The Beam

Beam 5 of the AGS at Brookhaven National Laboratory which is described in detail in Appendix A is composed of 7 quadrupoles, 3 dipoles, 2 electrostatic beam separators, 2 beam stops and a mass slit. Figure 2.2 shows the arrangement and positions of these magnets and beam separators. Beam fluxes and pion contaminations as a function of momentum are given in Table 2.1 The typical momentum acceptance of the beam was $\pm 3\%$ nominal beam momentum.

In order to insure that an incident beam particle traversed the hydrogen target, a threefold coincidence in three beam defining counters S_1 , S_2 , and S_3 was required. These counters were arranged so that any straight line drawn through all three intersected all of the liquid hydrogen target. A beam particle was defined as a particle which satisfied this coincidence requirement.

To eliminate unwanted π^- contamination in the beam and the corresponding background reaction $\pi^- p \rightarrow p\pi^-$ which is kinematically similar to the reaction $\bar{p}p \rightarrow k^+k^-$ at extreme angles, a liquid radiator Č counter¹⁹⁾ and a time-of-flight system were also used to identify incident \bar{p} 's. Figure 2.3 is a schematic drawing of the beam liquid differential Č counter. Čerenkov light from antiprotons moving through the radiator cell was reflected to the Č photomultiplier tubes by means of the movable diaphragm mirror (the dashed line) whereas Čerenkov light from the faster moving pions came off with a larger cone angle and was reflected to the anti Č(C) photomultiplier tubes (the dot-dashed line). Figure 2.4a is a plot of the percentage

of beam particles giving a \check{C} counter signal as a function of diaphragm mirror position at a typical momentum. The pion contamination under the \bar{p} peak is seen to be less than 5%. At 2 GeV/c, the \bar{p} efficiency was better than 90%.²⁰⁾

At low incident \bar{p} momenta (.7 to 1.0 GeV/c) limitations on the magnitude of the index of refraction of available liquids and increased probability for scattering reduced the efficiency of the differential \check{C} counter. However, the relatively low β of the \bar{p} compared to that of the pion below 1.0 GeV/c ($\beta_{\bar{p}} \sim .7$, $\beta_{\pi} \sim 1.0$) made it possible to use time-of-flight (TOF) to identify \bar{p} 's. A set of 7 counters near the mass slit about 41 feet upstream of the target was used in conjunction with the S_3 counter to give a time-of-flight measurement of the beam particle velocity. The difference in flight time over this distance between \bar{p} 's and pions at low energies was ~ 4 sec. Figure 2.4b shows the response of this system as a function of time delay.

At low momenta the time-of-flight system was used in anticoincidence with the \check{C} counter set to accept pions. At momenta above 1 GeV/c when the time-of flight difference between \bar{p} 's and pions is less than 4 nsec, the \check{C} counter was set to accept \bar{p} 's and to reject pions and was used above. A beam \bar{p} was thus defined at low momenta as a beam particle in coincidence with the TOF system set to accept \bar{p} 's and in anticoincidence with the \check{C} counter set to accept pions and at momenta greater than 1.0 GeV/c as a beam

particle in coincidence with the \checkmark counter set to accept \bar{p} 's and to reject pions. The over-all pion contamination in number of beam \bar{p} 's was reduced in this way to less than 1% at all momenta (Figure 2.5).

Spurious sparking in the wire spark chambers upstream of the liquid hydrogen target was undesirable because the wire spark chamber efficiency for trackfinding was considerably lower when there were spurious sparks in the chambers and more than two particle tracks in the upstream chambers 1-4 increased the complexity of event recognition in the event reconstruction procedure. In order to reduce the number of sparks and tracks not associated with events of interest in these chambers, a special beam gating system was used.

On the average, a wire spark chamber triggered at $t = .3$ μsec (the real event satisfying all the trigger criteria actually occurring in the apparatus at $t = 0$) will break down at all points where the particles have passed through it as long before as $t = -.7$ μsec . Therefore, a .5 to .7 μsec dead time circuit which typically reduced the amount of usable beam by 10-30% was used to reduce the number of triggered events with spurious tracks.

This pile-up system worked as follows: whenever a particle passed through beam counter S_2 or beam halo counter A_u it generated

a pulse rendering the threefold beam counter coincidence circuit dead for .5 to .7 μ sec. This pulse came too late to prevent an event satisfying all the trigger logic criteria from triggering the wire chambers; however, it guaranteed that no beam particle not producing a trigger had passed through the apparatus between $t = - (.5 \text{ to } .7) \mu\text{sec}$ and $t = 0$. Hence, only those beam particles and scatterings occurring between $t = .0$ and $t = .3 \mu\text{sec}$, the approximate delay time in the fast logic to produce a wire spark chamber trigger, could give spurious tracks in the chamber.

Since some extra beam tracks in the wire chambers upstream of the target were unavoidable, two arrays of 4 $2'' \times 1/2'' \times 1/4''$ scintillation counters called beam hodoscopes arranged in horizontal and vertical rows and located just downstream of beam defining counters S_2 (Figure 2.1) were used to remove beam track ambiguities in the analysis of upstream wire chamber data. Coincidences between event trigger pulses and beam hodoscope pulses delayed .3 μ sec were recorded on magnetic tape as counter bits. Extra tracks in the upstream wire spark chambers having slopes less than 50 mrad which did not extrapolate back to a beam hodoscope satisfying the time coincident requirement could be removed from further consideration.

After the wire chambers were triggered, a gate pulse from an interface acting as a buffer between event recognition and data recording system prevented another trigger during a 20 msec interval to allow the wire chambers to recover. No \bar{p} beam particles incident on the apparatus during this time were included in the

\bar{p} flux used in the cross section calculation. Two 100 megacycle scalars were used simultaneously to count this gated \bar{p} beam particle flux. Other scalars used to monitor the beam counted particles at a 30° AGS beam monitor, beam particles without the pile-up gate, gated and ungated beam particles, ungated \bar{p} beam particles, and beam halo particles.

Since too many beam particles incident on the apparatus would have saturated the electronics and increased the number of extra tracks in the wire spark chambers, the sum of the number of particles passing through the beam halo counter A_u and the beam defining counter S_2 was kept below 200 K per pulse. Consistent results between runs at these beam rates and lower rates indicated that 200 K was an acceptable upper limit.

In order to determine the momentum of the incident beam particle to better than 3% of the average beam momentum, an array of 7 scintillation counters called the mass slit counters were placed in the beam just upstream of the bending magnet D_3 (Figure 2.2). Using the fact that beam particles of different momentum must have different horizontal positions in space at the vertical focus point (mass slit) the momentum distribution of particles traversing a given counter were experimentally determined and a typical result is shown in Figure 2.6.

The distributions of the horizontal and vertical position and slopes of beam particles at three representative momenta are given in Figure 2.7. Sizes and positions of beam counters are given in Table 2.2.

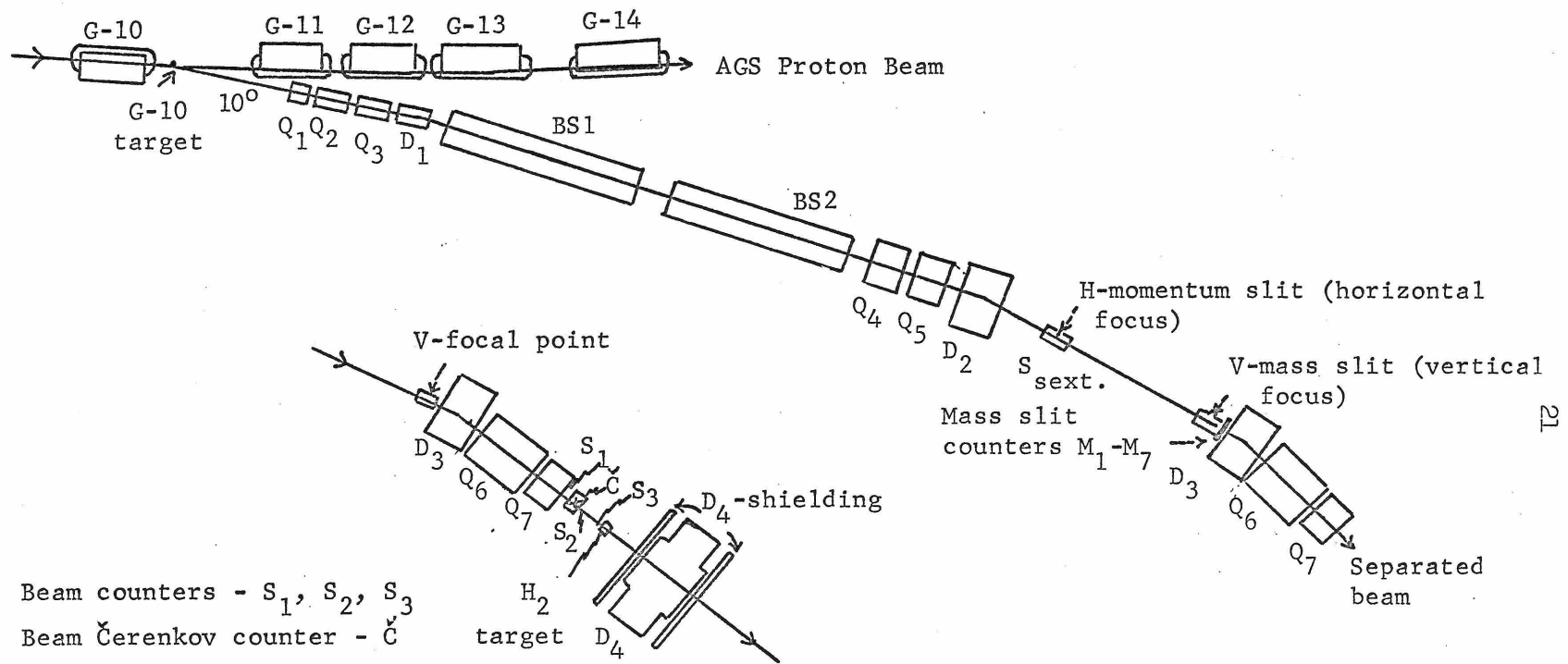


Figure 2.2: Layout of the separated beam transport system. Q₁ - Q₇ are quadrupole magnets, D₁ - D₃ are dipole magnets, S_{sext} is a sextupole magnet (not used), and BS1 and BS2 are electrostatic separators. Also shown is the experimental area with the beam telescope, the Čerenkov counter (Č), the liquid H₂ target, and the large aperture, momentum analyzing magnet (D₄).

Table 2.1

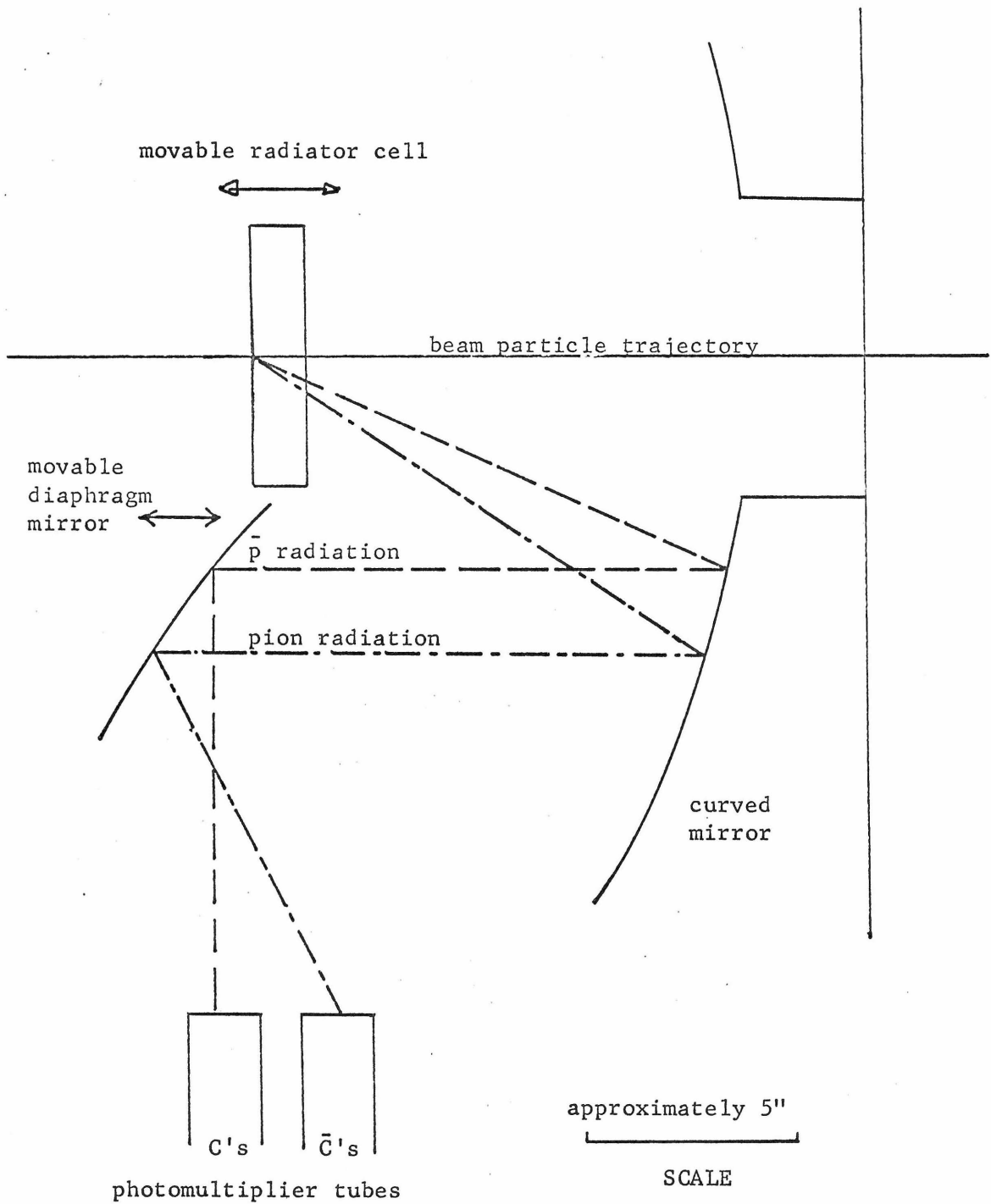
Beam fluxes and rates for each momentum. The actual momentum is the momentum of the beam particle incident on the target. A typical AGS pulse corresponded to about 1.5×10^{12} circulating \bar{p} 's in the primary beam.

<u>Momentum</u>		<u>Total \bar{p} flux in millions</u>	<u>Beam Particles per typical</u>	<u>\bar{p} pulse</u>	<u>π/\bar{p}</u>	<u>Positive Particle Forward</u>		<u>Negative Particle Forward</u>	
<u>Nominal (GeV/c)</u>	<u>Actual (GeV/c)</u>					<u>Trigger</u>		<u>Trigger</u>	
					<u>Regular</u>	<u>Wide Angle</u>	<u>Regular</u>	<u>Wide Angle</u>	
.680	.700	12.6	8K	.5K	15.0	.20	1.10	.45	1.10
.770	.810	5.6	20K	.9K	21.0	.20	1.05		
.890	.870	44.0	13K	1.0K	12.0	.29	.43	.29	.45
.970	.990	101.7	46K	3.5K	12.0	.20	.95	.35	.95
1.090	1.120	77.8	26K	4.0K	5.5	.17	.37	.35	.85
1.340	1.340	113.4	24K	8.0K	1.9	.19	.27	.29	.29
1.450	1.450	92.5	24K	8.5K	1.8	.20	.80	.70	.80
1.585	1.590	130.0	30K	11.0K	1.8	.20	.36	.40	.37
1.700	1.710	98.7	35K	13.0K	1.8	.20	.75	.60	.75
1.815	1.815	234.8	55K	22.0K	1.5	.20	.70	1.00	.60
2.000	2.000	116.0	55K	22.0K	1.5	.20	.65	1.50	.70
2.125	2.160	187.3	55K	28.0K	1.0	.13	.27	.57	.45
2.250	2.260	40.1	37K	8.1K	3.6			.20	.70
2.365	2.400	123.7	75K	45.0K	.6	.27	.31	.82	.32

22

* Fluctuations in trigger rates for both triggers are due to beam steering and beam focusing fluctuations. In addition the number of trigger scintillation counters in the wide angle trigger was increased during the running of the experiment.

Figure 2.3: Schematic drawing of the beam liquid differential \bar{p} Cerenkov counter. The C's are the coincidence signal and the \bar{C} 's are the veto signal. All scales are approximate.



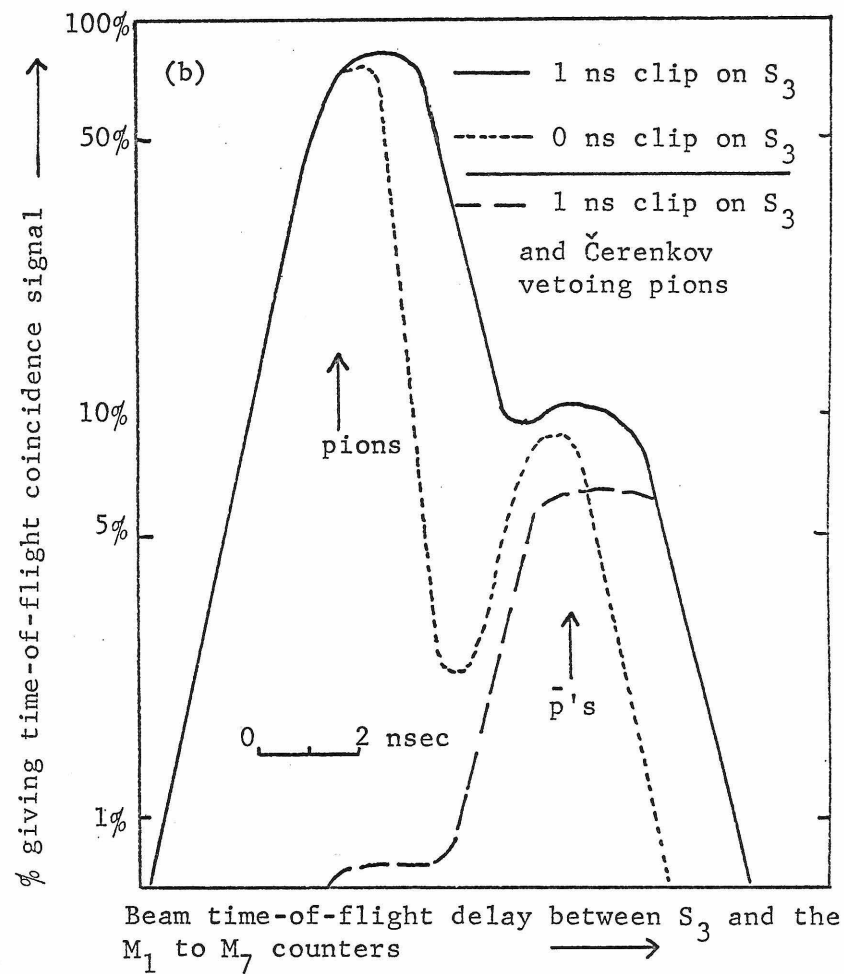
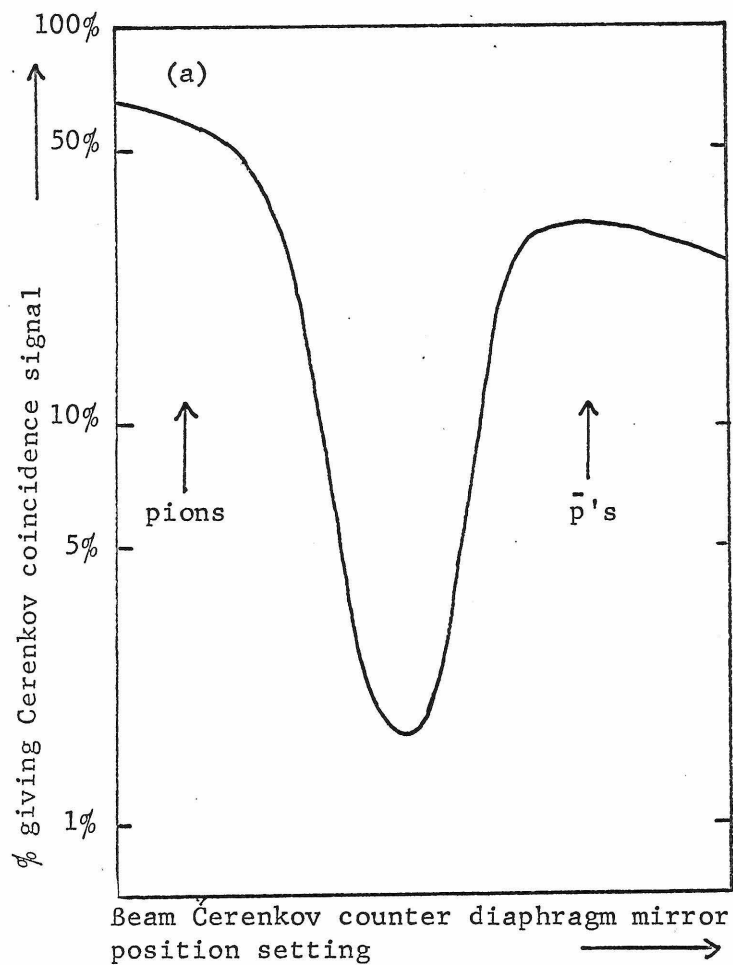


Figure 2.4: (a) % of Čerenkov coincidence vs. diaphragm mirror position. If, in the Figure 2.3, the diaphragm mirror moves to the left, the C's would then receive the pion radiation. (b) % of beam time-of-flight coincidence vs. time-of-flight delay.

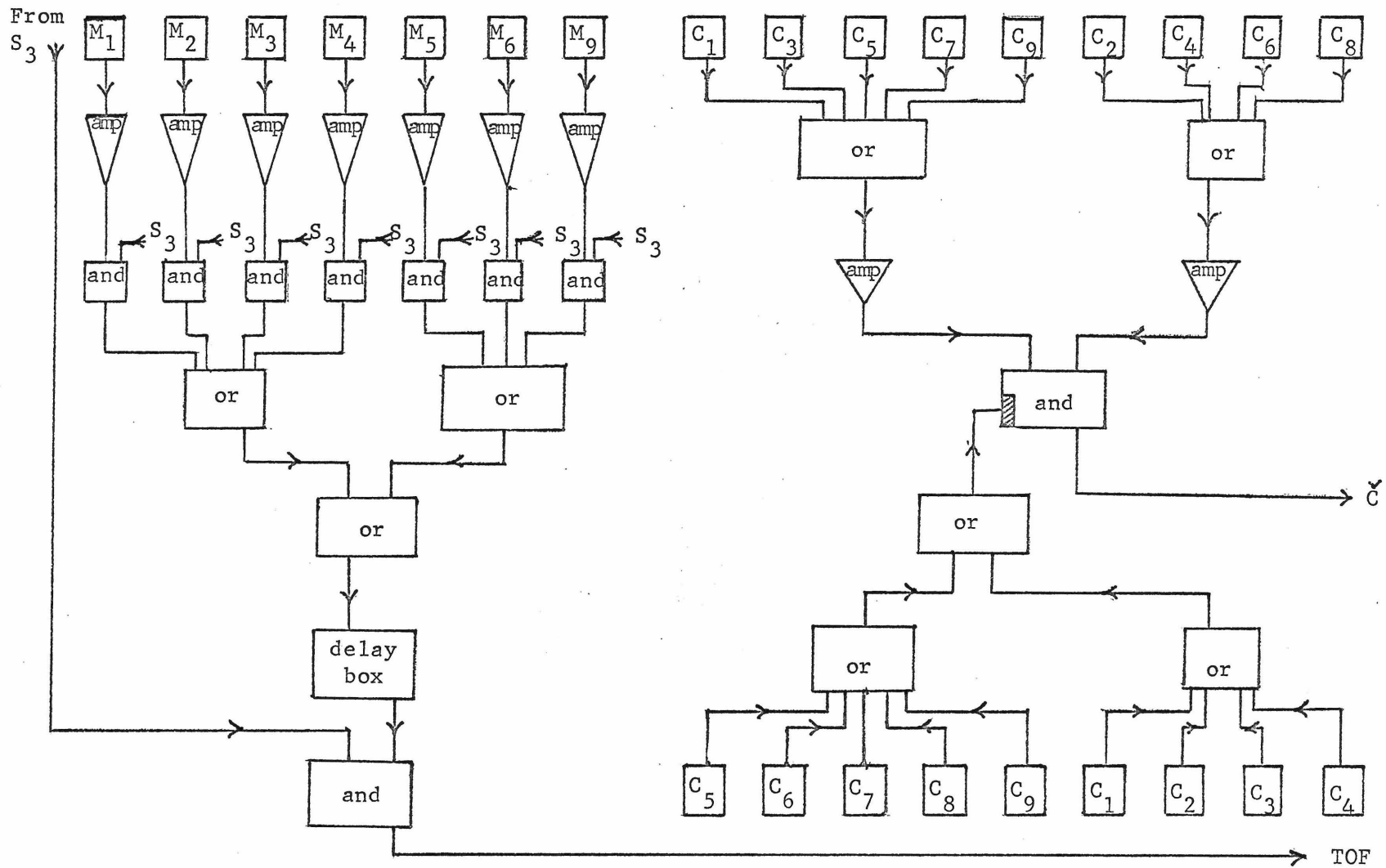


Figure 2.5: Diagram of Čerenkov counter and time-of-flight logic.

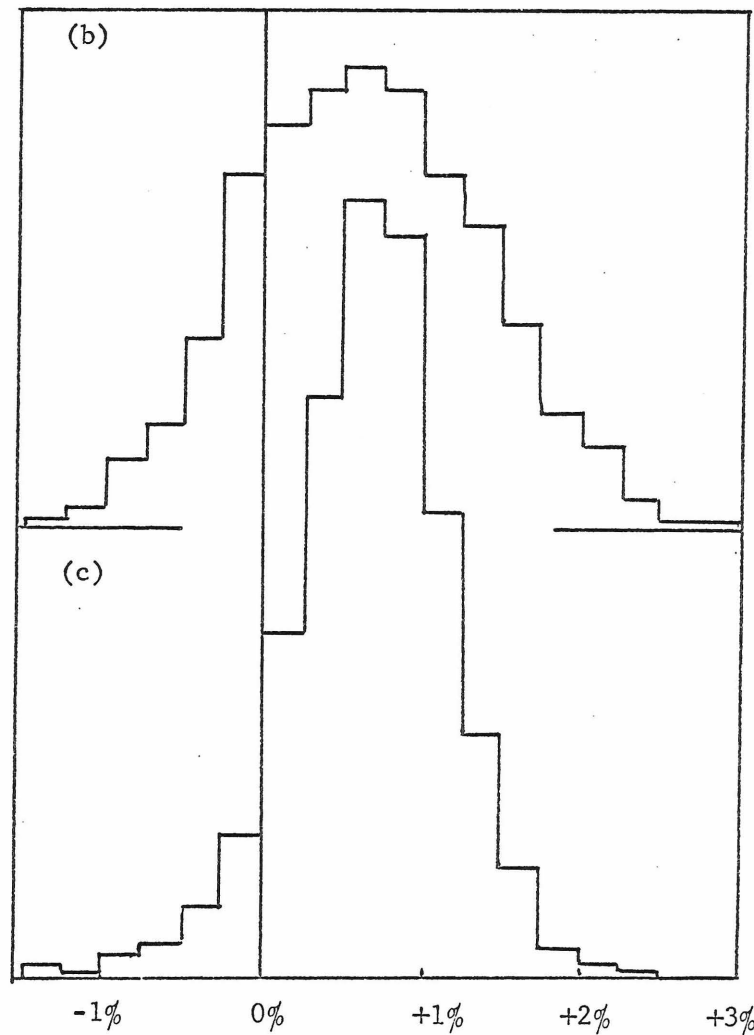
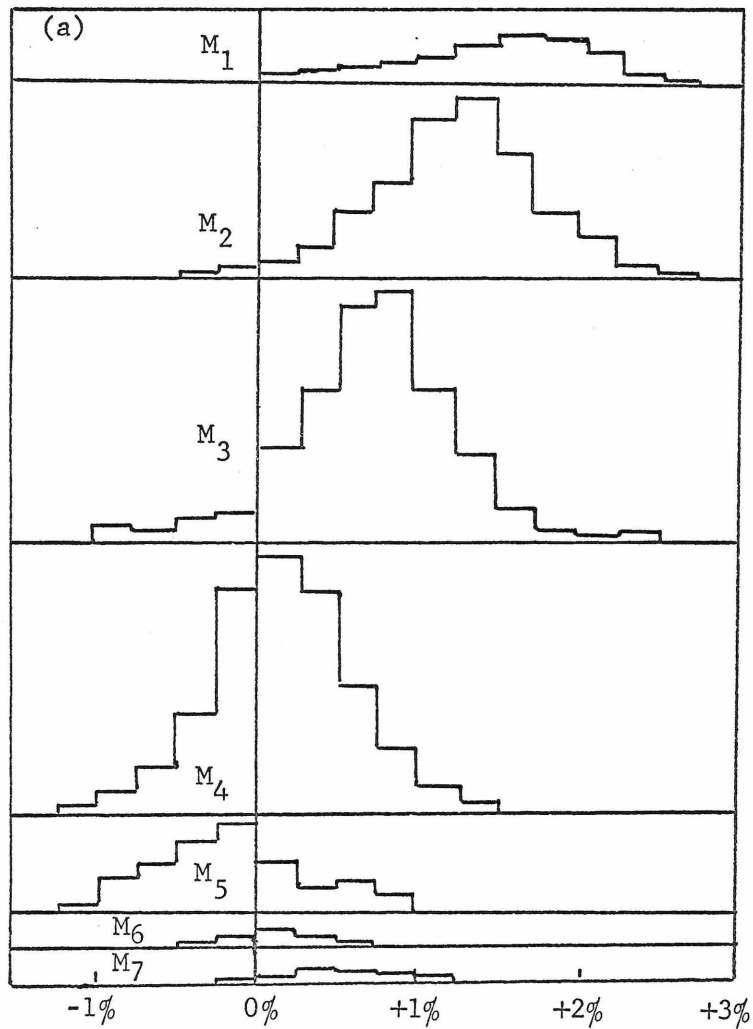


Figure 2.6: Momentum distributions of incident \bar{p} 's at 2.0 GeV/c nominal momentum for: (a) \bar{p} 's hitting particular mass slit counters. (b) all \bar{p} 's. (c) all \bar{p} 's corrected according to which mass slit counters are hit.

Figure 2.7: continued

Horizontal slope distribution (in units of 10 mr)

Vertical slope distribution (in units of 10 mr)

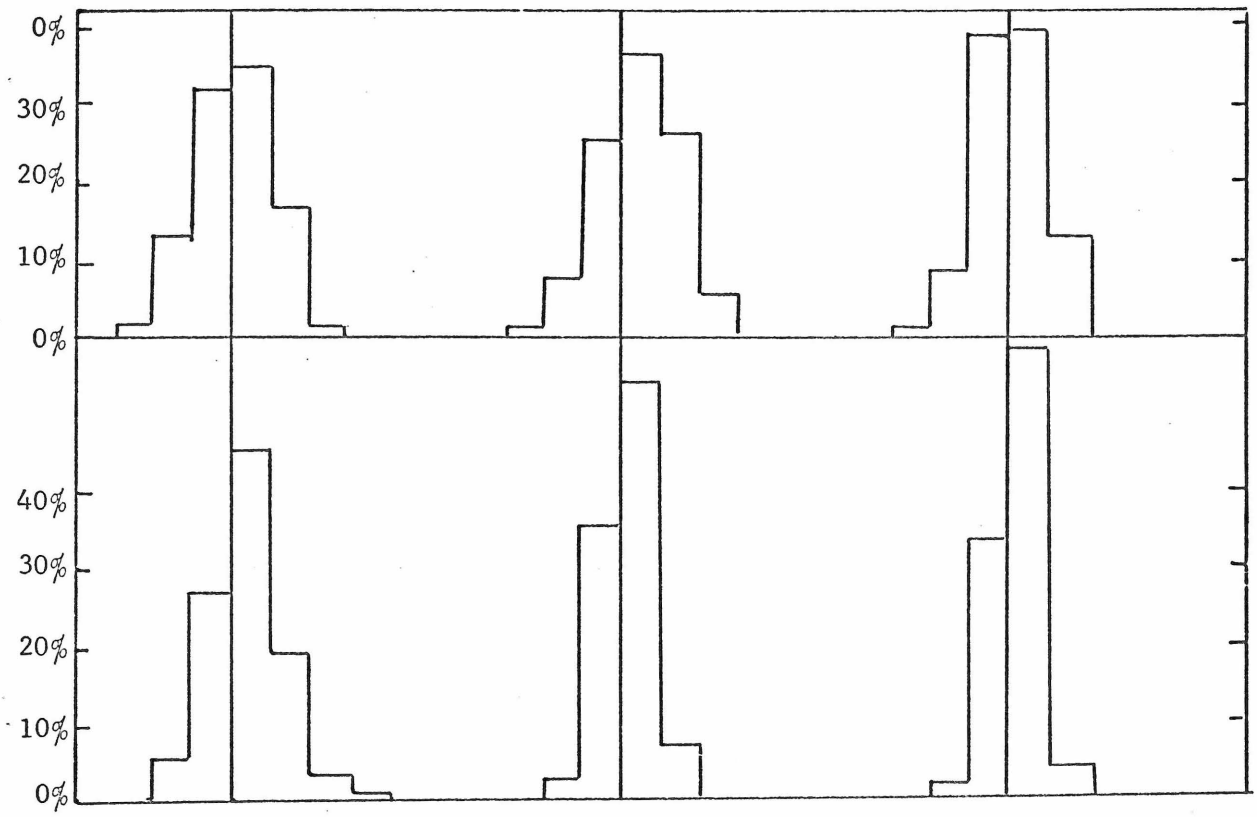


Table 2.2

Sizes and Positions of Beam Counters

<u>Counters</u>	<u>Dimensions</u>	<u>Beam Position</u>
Mass slit $M_1 - M_7$ (7 counters)	1-1/2" wide** 1/8" thick	Just upstream of mass slit $z \sim - 14'$
Beam defining		
S_1	3" diameter 1/4" thick	$z = - 75''$
S_2	2" diameter 1/4" thick	$z = - 39''$
S_3 ***	3-1/8" x 2-1/4" 1/8" thick	$z = - 11-7/8''$
Beam Halo		
A_u	22" high (2" diameter 12" wide hole in center) 1/4" thick	$z = - 39-7/8''$
Beam hodoscope		
Horizontal array	2" x 1/2"	$z = - 35-3/4''$
$H_{x_1} - H_{x_4}$	1/4" thick	
Vertical array		
$H_{y_1} - H_{y_4}$ (8 counters)		
Differential Čerenkov Counter		
Radiator cell	6" diameter 1/2" - 1" thick	$z \sim - 50''$

* $z = 0$ at center of target and increases in beam direction.

** Counters higher than mass slit aperture.

*** S_3 was set 45° to beam line to present a circular aperture of 2-1/4" diameter to the beam.

2. The Target

In order to increase the probability of a beam particle-proton interaction, the liquid H₂ target should be made as long as possible. The largest target which could be made compatible with the already existing experiment equipment was 14-5/8" (37.2 cm) long and 3" (7.6 cm) in diameter and was housed in a vacuum box 15-3/4" wide set 45° to the beam line. The liquid hydrogen was contained in a single jacket of 14 mil mylar surrounded by 40 layers of .3 mil aluminized mylar acting as superinsulation and was maintained at atmospheric pressure near the boiling point at a density of .0708 gm/cm³. Such a target resulted in the interaction of ~ 10% of the incident beam antiprotons.

3. The Bending Magnet

When the two reaction particles in a two particle initial state, two particle final state interaction form appreciable angles with the incident particle beam direction ($\sim 15^\circ$ for backward particle $\sim 5^\circ$ for forward particle); knowledge of the beam particle momentum and the laboratory angles of the reaction products is sufficient to accurately determine the masses of the reaction products and $\bar{p}p \rightarrow \pi^\pm \pi^\mp$ events can be separated from $\bar{p}p \rightarrow k^\pm k^\mp$ events. However, when the two reaction particles are produced in the nearly forward and nearly backward directions, the momentum of one of the reaction particles, in this case the forward going particle, must be measured to accurately determine the masses of the reaction products.

In order to momentum analyze charged forward going particles it is necessary to have a bending magnet with an accurately known magnetic field. The magnet used in this experiment (D_4) was a heavily magnetically shielded 48 D48 dipole magnet with an 18" vertical aperture.

The two iron-wood sandwich shieldings bolted to the magnet sides and consisting of iron layers 3/4", 1" and 6" thick reduced the upstream and downstream apertures to 14" x 28" and 16-1/4" x 46-1/4", respectively, but were sufficiently large so that any particle traversing all the wire spark chambers would not strike the shielding wall. Such extensive shielding was necessary to reduce the high fields inside the magnet (5-15 kgauss) to the levels just outside the magnet which were required for the satis-

factory performance of shielded photomultiplier tubes on scintillation counters and magnetostrictive readout wires on wire spark chambers close to the magnet (< 100 gauss). Even with the shielding the vertical magnetostrictive wires on wire spark chambers downstream of the magnet had to be remagnetized in the direction of the magnetic field of D_4 every time its polarity was changed to prevent loss of magnetization from stray longitudinal fields.

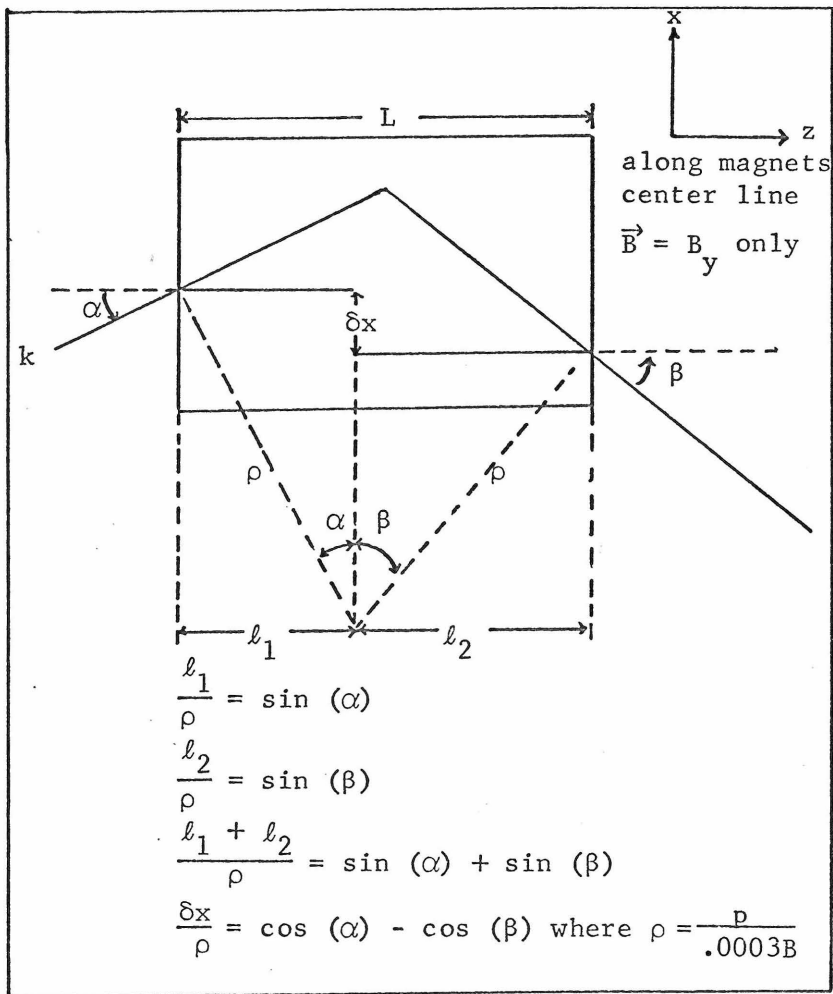
The field (B) at the center of the magnet was measured by means of a nuclear magnetic resonance probe. The equation for the effective length (L) over which a constant magnetic field of this magnitude acts for the magnet used in this experiment is

$$L = 155.60 \text{ cm} / (1 + (B/255.51 \text{ kg})^{0.999991}) \quad (1)$$

and the momentum (p) of a particle traversing the magnet is given by

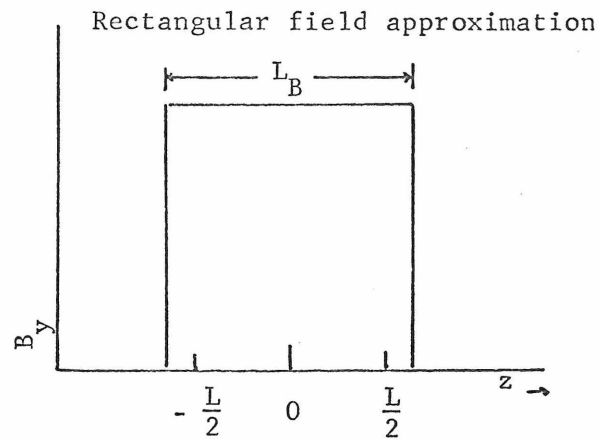
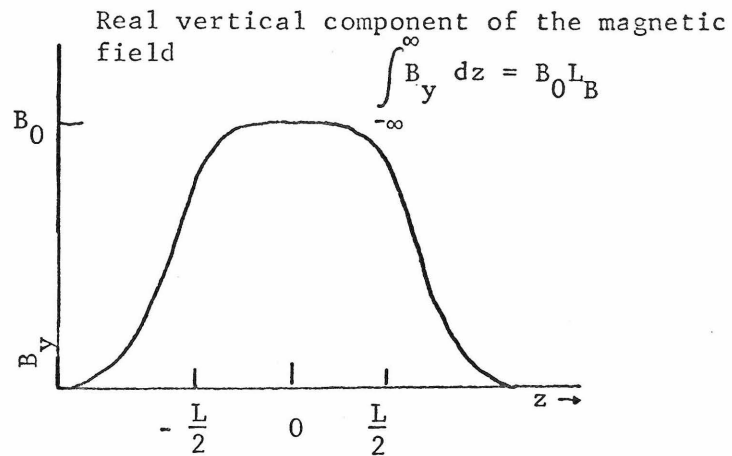
$$p(\text{GeV}/c) = \frac{2.9978 \text{ B(kgauss)} \text{ L(cm)} (1 + x'^2 + y'^2)^{1/2}}{100(\sin \alpha + \sin \beta) (1 + x'^2)^{1/2}} \quad (2)$$

where x' and y' are the incident horizontal and vertical slope and α and β are the horizontal incident and outgoing angle, respectively (Figure 2.8). The momentum calculated from Eq. (2) was shown by studies to be accurate to within 0.3%.²¹⁾



Relation between the horizontal deflection of a track and its momentum

(a)



(b)

Figure 2.8: Rectangular field model for a dipole magnet.

4. Trigger Logic

To reduce the number of recorded background events to be analyzed, the wire spark chambers were only triggered for annihilation events satisfying either of two trigger conditions. One partial set of acceptable trigger conditions occurred when a backward going particle was detected by an array of scintillation counters upstream of the target (B counters) in time coincidence with a forward going particle detected by an array of scintillation counters downstream of the target and upstream of the magnet D_4 (P counters), and an array of scintillation counters downstream of the magnet (R counters). The second partial set of acceptable trigger conditions occurred when a backward going particle traversing a wide angle B counter ($B_3 - B_6$) was in time coincidence with a forward going particle traversing a wide angle P counter ($P_6 - P_{10}$) with no requirement on the R counters. The sign of the change of a forward going particle could be determined by the direction of bend in its trajectory as it traversed the D_4 magnet; this information was not available on most of the wide angle triggers since they did not require that the forward particle traverse the magnet.

In addition to the requirements on the B, P, and R counter arrays, two other conditions had to be met to produce a trigger. To reduce recorded background from multiparticle final state annihilations, scintillation counters (A_L^i counters, $i = L, R, B, A$) located in regions of space where neither particle of a two particle annihilation reaction satisfying the B, P, and R trigger conditions could be found were set in anticoincidence with the B,

P, and R counter trigger conditions. In addition the beam particle was required to vanish.

When the trigger was set for positively charged forward going particles, the negatively charged beam passed through the Q counters and high numbered R counters ($R_4 - R_6$). A time coincidence between these counters was set in time anticoincidence with an otherwise acceptable trigger to prevent events without disappearing beam particles from being recorded.

When the trigger was set for negatively charged forward going particles, the beam passed through the counters A_{D_M} and A_{D_L} which were also set in time coincidence with each other and in anticoincidence with the trigger. The fact that the forward going meson in the annihilations $\bar{p}p \rightarrow \bar{\pi}\pi$ or $\bar{p}p \rightarrow \bar{k}k$ has a momentum greater than the incident antiproton prevented the particles produced in the annihilation events of interest from bending as much as the beam particles and activating those veto counters.

A flow chart of the trigger logic is given in Figure 2.9.²²⁾ Trigger counter dimensions and positions are given in Table 2.3 and are shown schematically and approximately to scale in Figure 2.1.

Scalars continuously monitored the number of \bar{p} beam particles passing through A_D or A_D' , the number of annihilation triggers requiring a particle to traverse the magnet, a number of wide angle annihilation triggers and the total number of particles traversing all the B counters, all the P counters, all the R counters, and all the A_T counters. Consistent readings of these quantities for a

series of data runs insured proper operation of the individual components of the over-all trigger logic circuit and the time consistency of the beam characteristics.

The complete annihilation trigger is given below

Positive particle forward

$$T_+ = \left[\left(\sum_{i=1}^3 S_i \right) \cdot \check{C} \cdot \overline{\left(\sum_{i=1}^4 A_T^i \right)} \cdot \left\{ \left(\sum_{i=1}^6 B_i \right) \cdot \left(\sum_{i=1}^6 P_i \right) \cdot \left(\sum_{i=1}^6 R_i + \sum_{i=4}^5 Q_i \right) \right. \right. \\ \left. \left. + \left(\sum_{i=3}^6 B_i \right) \cdot \left(\sum_{i=6}^{10} P_i \right) \right\} \cdot \overline{\left(\sum_{i=4}^5 (R_i + Q_i) + \sum_{i=5}^6 R_i \right)} \right]$$

Negative particle forward

$$T_- = \left[\left(\sum_{i=1}^3 S_i \right) \cdot \check{C} \cdot \overline{\left(\sum_{i=1}^4 A_T^i \right)} \cdot \left\{ \left(\sum_{i=1}^6 B_i \right) \cdot \left(\sum_{i=1}^6 P_i \right) \cdot \left(\sum_{i=1}^6 R_i + \sum_{i=4}^5 Q_i \right) \right. \right. \\ \left. \left. + \left(\sum_{i=3}^6 B_i \right) \cdot \left(\sum_{i=6}^{10} P_i \right) \right\} \cdot \overline{\left(A_D^M + A_D^L \right)} \right].$$

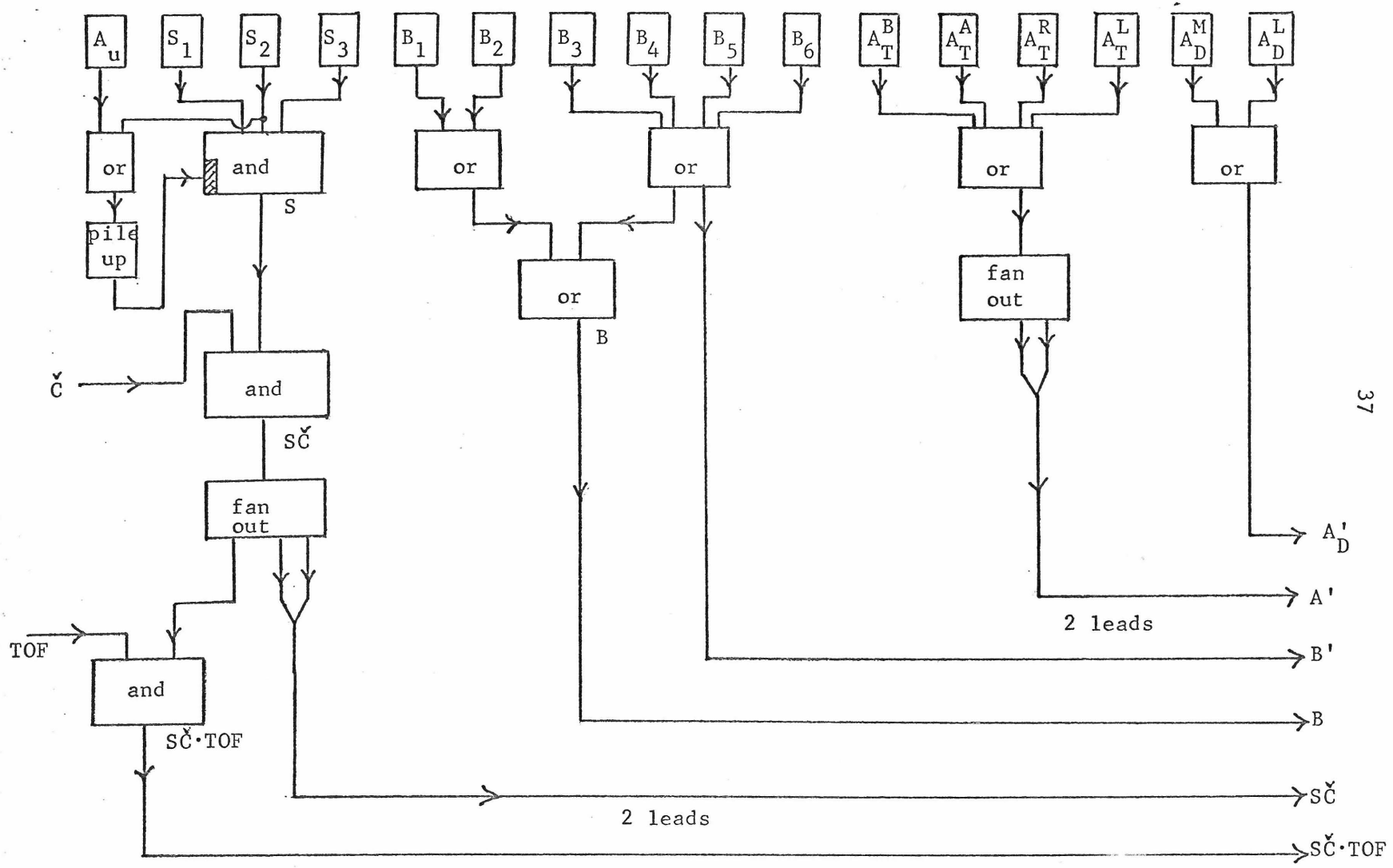


Figure 2.9: Flow diagram of trigger logic

Figure 2.9 continued

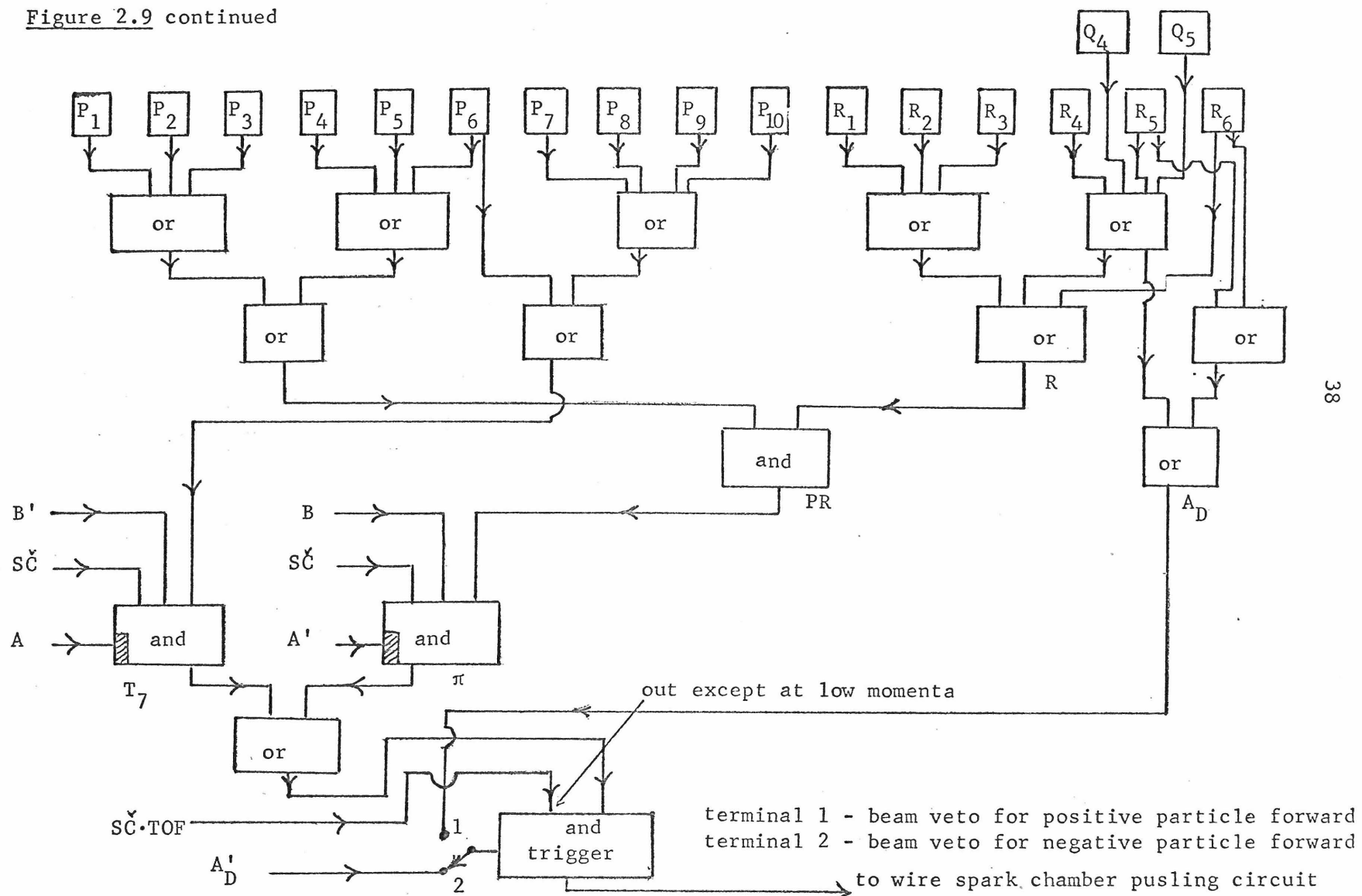


Table 2.3

Sizes and Position of Trigger Counters

Counter	Size			Position		
	<u>X</u>	<u>Y</u>	<u>Z</u>	<u>X</u>	<u>Y</u>	<u>Z</u>
P ₁	3"	7"	1/8"	- 4" to - 1"	- 3-1/2" to 3-1/2"	38-1/4"
P ₂	3"	7"	1/8"	- 1-1/2" to 1-1/2"	- 3-1/2" to 3-1/2"	38-1/4"
P ₃	3"	7"	1/8"	1" to 4"	- 3-1/2" to 3-1/2"	38-1/4"
P ₄	3"	7"	1/8"	3-1/2" to 6-1/2"	- 3-1/2" to 3-1/2"	38-1/4"
P ₅	3"	7"	1/8"	6" to 9"	- 3-1/2" to 3-1/2"	38-1/4"
P ₆	3"	7"	1/8"	8-1/2" to 11-1/2"	- 3-1/2" to 3-1/2"	38-1/4"
P ₇	7"	11"	1/4"	10-3/8" to 17-3/8"	- 5-3/4" to 5-1/4"	34-3/4"
P ₈	3"	12"	1/4"	16-3/4" to 19-3/4"	- 5-3/4" to 6-1/4"	35-1/4"
P ₉	5"	11"	1/4"	19-1/4" to 24"	- 5-1/4" to 5-3/4"	36-1/4" to 38"
P ₁₀	7-1/2"	13"	1/4"	11" to 18-1/2"	- 6-1/2" to 6-1/2"	21-1/2"
A _{DL}	12"	24"	1/4"	-37" to -24-1/2"	-12-1/4" to 11-3/4"	175-3/8"
R ₀	14"	24"	1/2"	-30" to -16"	-12-1/4" to 11-3/4"	175-3/8"
R ₁	14"	24"	1/2"	-24-1/2" to -10-1/2"	-12-1/4" to 11-3/4"	175-3/8"
R ₂	14"	24"	1/2"	-14" to 0	-12-1/4" to 11-3/4"	175-3/8"
R ₃	14"	24"	1/2"	- 4" to 10"	-12-1/4" to 11-3/4"	175-3/8"
R ₄	14"	24"	1/2"	7" to 21"	-12-1/4" to 11-3/4"	175-3/8"
R ₅	14"	24"	1/2"	16-1/2" to 30-1/2"	-12-1/4" to 11-3/4"	175-3/8"
R ₆	14"	24"	1/2"	26-1/2" to 40-1/4"	-12-1/4" to 11-3/4"	175-3/8"

Table 2.3 (continued)

Counter	Size			Position		
	<u>X</u>	<u>Y</u>	<u>Z</u>	<u>X</u>	<u>Y</u>	<u>Z</u>
Q ₄	12"	22"	1/4"	9" to 21"	-11" to 11"	139-1/4"
Q ₅	12"	22"	1/4"	19-1/2" to 31-1/2"	-11" to 11"	139-1/4"
A _D _S	4"	3"	1/4"	-28" to -24"	- 1-1/2" to 1-1/2"	186-5/8"
B ₁	9"	25"	1/2"	11" to 10-1/2"	-10-1/2" to 14-1/2"	-21" to -23"
B ₂	9"	25"	1/2"	3" to 12"	-10" to 15"	-22"
B ₃	9"	25"	1/2"	- 5-1/4" to 3-3/4"	- 9-3/4" to 15-1/4"	-22"
B ₄	9"	25"	1/2"	-13" to - 4"	- 9-3/4" to 15-1/4"	-22"
B ₅	9"	25"	1/2"	-12" to -21"	- 9-3/4" to 15-1/4"	-22"
B ₆	7-1/2"	13-1/2"	1/4"	-26" to -20-1/2"	- 7-1/2" to 6"	-17-3/4" to -22-3/4"
A _D _M	9"	9"	1/2"	-12" to -21"	- 4" to 5"	126"
A _T ^L	24"	11"	1/4"	9-3/4" to 27-1/4"	- 5-1/2" to 5-1/2"	-10" to 6"
A _T ^R	25"	12"	1/4"	-29-1/2" to - 5-1/4"	- 5-3/4" to 6-1/4"	16-1/4" to 23-1/4"
A _T ^{B,A}	3 irregular shaped counters			x of both counters through target center		
	max. width 14"			- 9-1/4" to 10-1/2"		
below target	max. length 26"			y lower - 5-1/4"		
	thickness 1/4"					
above target	2 counters total width 12"			y upper 4-3/4"		
	length 26"			z of both counters along beam line		
	thickness 1/4"			-10" to 9-1/2"		

40

* x,y, and z positions of the B counters are with respect to a coordinate system rotated 45° counterclockwise about the negative y axis (see Figure 2.1).

5. The Wire Spark Chambers

In order to accurately record the trajectories in space of the particles in the triggered events, three sets of four wire spark chambers were used, one upstream of the target (chambers 1-4), one downstream of the target and upstream of the D_4 magnet (chambers 5-8), and one downstream of the magnet (chambers 9-12). Chamber numbers increased sequentially with increasing z position along the beam line. Chambers 1-4 were arranged so that a line drawn normal to the plane of their sensitive areas formed a 45° angle with the beam center line (Figure 2.1).

When the backward scattered meson in the reaction $\bar{p}p \rightarrow \pi^\pm \pi^\mp$ or the reaction $\bar{p}p \rightarrow k^\pm k^\mp$ forms a laboratory angle with respect to the antiproton beam line of $\sim 15^\circ$ the calculated laboratory angle of the forward pion in a two pion annihilation differs from the calculated laboratory angle of the forward kaon in a two kaon annihilation by $\sim .7^\circ$ for incident antiproton momenta between .7 and 2.4 GeV/c. Consequently, in order to separate the reactions $\bar{p}p \rightarrow \pi^\pm \pi^\mp$ and $\bar{p}p \rightarrow k^\pm k^\mp$ when the momentum of the forward going particle was not measured by using the measured laboratory angle of the forward going particle for a given beam momentum, it was necessary to measure the angles of the forward and backward going mesons to the order of 5 mrad. Since the minimum distance between the liquid hydrogen target and wire spark chambers 1 and 8 were ~ 260 mm and ~ 620 mm, respectively, the resolution of the wire spark chambers was required to be ~ 1 mm to achieve the desired separation.

Figure 2.10 shows the distribution of sparks in chambers 1

through 8 for straight beam tracks for an incident antiproton momentum of .99 GeV/c. It can be seen from the widths of the peaks in the figure that the experimental resolution of the wire spark chambers is ~ 1 mm.

Each wire spark chamber consisted of two planes of parallel coplanar wires 20/inch and 25 mils wide etched onto fiberglass epoxy sheets 3-4 mils thick, spaced 1/4" apart and oriented so that the wires in each plane were at right angles to each other.²³⁾ The wires on each wire plane were connected together electrically by means of a bus bar laid across the wire ends. A 90-10% neon helium gas mixture just above atmospheric pressure with $\sim 1\%$ mixture of isopropanol alcohol acting as spark quenching agent flowed slowly between an inlet and exit hole in the chamber frame through the 1/4" gap between the wire planes and was retained in the chamber by two mylar windows glued to the fiberglass chamber frame.

To pulse the chambers a trigger pulse from the fast logic activated a pulse driven circuit which produced a .8 kv, 80 nsec pulse which in turn activated 12 thyatron-discharge storage-capacitor circuits, one for each chamber. These applied a 2.9 - 3.3, 20 nsec pulse across the wire planes of a chamber by suddenly (~ 60 nsec) connecting a capacitor charged to 4.8 - 5.6 kv to one wire plane while the other wire plane was connected to ground. Ionization at points where charged particles had traversed the chamber gap up to 1 μ sec before pulsing created low resistance current paths in the chamber and avalanche breakdown sparking occurred at those points ~ 30 nsec after pulsing. If no sparking occurred in the chamber,

the voltage was bled off through a resistor with a time constant ~ 200 nsec.

When sparking occurred, the magnetic field from the large currents in the wires carrying charges to and from regions of breakdown sparking created electro-mechanical pulses in iron-cobalt magnetostrictive readout wires, one on each wire plane, which were laid across the wires near and parallel to the bus bars at the edges of the wire planes. These pulses, which re-oriented the magnetic domains in the magnetized wire, propagated along the magnetostrictive wire at $5.2 \text{ mm}/\mu\text{sec}$ and were electrically detected and amplified at the end of the wire (Figure 2.11).

Each time the chambers were pulsed large currents were made to flow in two edge wires on each wire plane called start and stop fiducials. These fiducials were measured in space to great accuracy and used as position references in the analysis.

The horizontal coordinate wire plane of chamber 1 was read out as follows (Figure 2.12). The amplified magnetostrictive pulse generated by the fiducial wire nearest the readout receiver-amplifier (the start fiducial) was used to start 4 scalars counting at 10 megacycles/sec. The pulses generated by the wires that had supplied the current to sparks in the chamber then sequentially turned off the scalars one at a time after being detected and amplified at the receiver. No more than 4 sparks per plane could be time digitized this way; any spark produced magnetostrictive pulse and the stop fiducial pulse arriving at the receiver after the

fourth detected pulse were lost. Assuming the pulse propagation rate along the wire was linear and knowing the time delay and the distance between start and stop fiducial pulses, the spark positions along this coordinate direction were determined to an accuracy of .52 mm per scalar digit.

The vertical coordinate of chamber 1 and the horizontal and vertical coordinates of chambers 2 to 12 were then read in by means of the serial readout system. Each magnetostrictive wire except the vertical coordinate wire of chamber 12 which had only a receiver-amplifier was equipped with a magnetostrictive pulse transmitter at one end and a pulse receiver-amplifier at the other. Spark and fiducial pulses of a given coordinate of a given chamber, after having been received and amplified initially by that chamber coordinate's receiver-amplifier, were retransmitted and rereceived along the entire chain of magnetostrictive readout wires until reaching the readout receiver of the horizontal coordinate of chamber 1. Digitizing then occurred in a manner identical to the digitizing procedure described above.

Electromagnetic disturbances generated at the instant of wire spark chamber sparking produced noise signals in the transmitters and receiving amplifiers. To prevent these signals from being treated as fiducial or spark generated pulses by the scalar digitizing system, masking pulses of adjustable length were produced by the interface.

The initial mask pulse was issued by the interface prior to

pulsing the chambers and was terminated about 3 μ sec prior to the arrival of the first start fiducial pulse at the readout receiver. A short scalar reset pulse was also issued by the interface at the termination of the initial mask pulse. About 5 μ sec after the pulse from the first stop fiducial reached the readout receiver (whether it was digitized or not) the interface issued a pulse stopping all scalars and a second mask pulse. This was terminated about 3 μ sec prior to the arrival of the start fiducial pulse of the first transmitted set of pulses when another reset scalar pulse was issued. This sequence was continued until both coordinate direction of all 12 wire chambers had been read in. Since the scalars were gated off for the duration of the mask pulse, noise due to chamber sparking was not digitized and recorded as data.

The principal advantage of this type of serial readout system over a parallel readout system is that it requires only one digitizing set of scalars and a relatively small amount of electronics. Since a 20 msec dead-time was imposed on all trigger electronics after each triggered event to allow the wire chambers to recover, the over-all serial readout time of 3 msec did not produce any extra loss of available beam. However, difficulties with the transmitter or receiver-amplifier by any one chamber coordinate affected the data readout from all higher numbered chamber coordinates as well. Difficulties with the mask generator or with transmitters or receivers on low numbered chambers rendered data from the entire system unreliable. The operation of the chamber electronics was

therefore carefully monitored during the running of the experiment.

The sizes and positions of the sensitive areas of the twelve wire spark chambers used in this experiment are given in Table 2.4. Characteristics of wire spark chambers such as memory and recovery time and need for clearing fields, spark formation and track resolution and multiple track resolution are discussed in detail in Appendix B.

Table 2.4: Sizes and Positions of the Sensitive Areas of the Wire Spark Chambers

Wire Chamber (sensitive area)	z position	x position	y position
Chambers upstream of target (1-4)**			
1 36" (x) by 18" (y)	- 18-3/4"*	-14-1/2" to 21-1/2"*	-9" to 9"
2 36" (x) by 18" (y)	- 15-3/4"*	-17-1/2" to 18-1/2"	-9" to 9"
3 36" (x) by 18" (y)	- 12"*	-21-1/2" to 14-1/2"	-9" to 9"
4 36" (x) by 18" (y)	- 9-1/4"*	-24-1/2" to 11-1/2"	-9" to 9"
Chambers downstream of target, upstream of D ₄ magnet (5-8)			
5 18" (x) by 9" (y)	12-3/4"	-2" to 16"	-4-1/2" to 4-1/2"
6 18" (x) by 9" (y)	19-1/4"	-2" to 16"	-4-1/2" to 4-1/2"
7 18" (x) by 9" (y)	25-1/2"	-2" to 16"	-4-1/2" to 4-1/2"
8 18" (x) by 9" (y)	31-3/4"	-2" to 16"	-4-1/2" to 4-1/2"
Chambers downstream of D ₄ magnet (9-12)			
9 36" (x) by 18" (y)	144-1/2"	-19-1/4" to 16-3/4"	-9" to 9"
10 36" (x) by 18" (y)	153-1/2"	-21-3/4" to 14-1/4"	-9" to 9"
11 36" (x) by 18" (y)	162-1/2"	-23-3/4" to 12-1/4"	-9" to 9"
12 36" (x) by 18" (y)	171-1/4"	-26-1/4" to 9-3/4"	-9" to 9"

* x,y, and z positions of the chambers upstream of the target are with respect to a coordinate system rotated 45° counterclockwise about the negative y axis (see Figure 2.1).

** Chamber numbers sequentially increase with increasing z position.

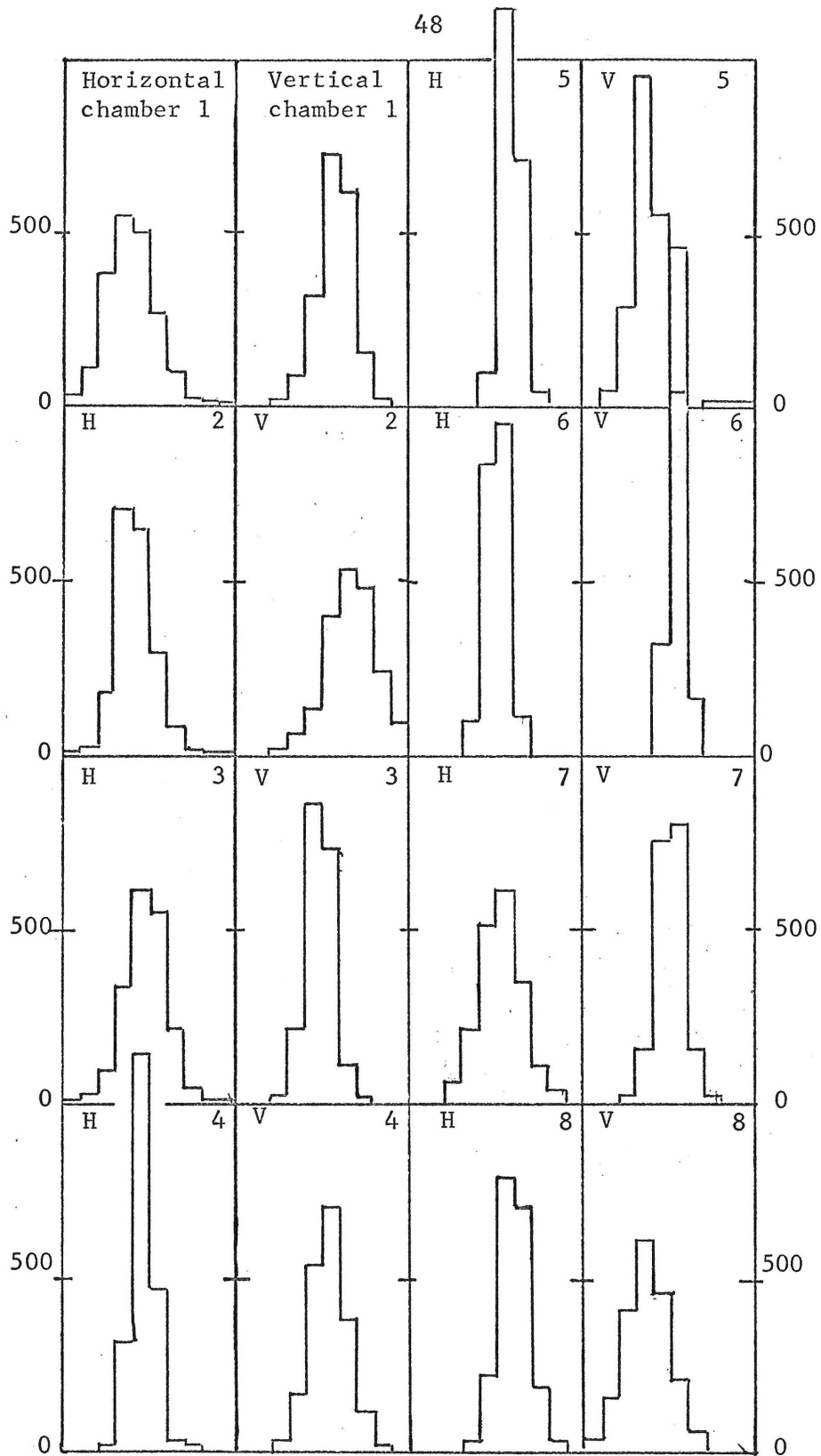


Figure 2.10: Horizontal and vertical distribution of sparks in wire spark chambers 1-8 for straight tracks. The bin size is .5 mm.

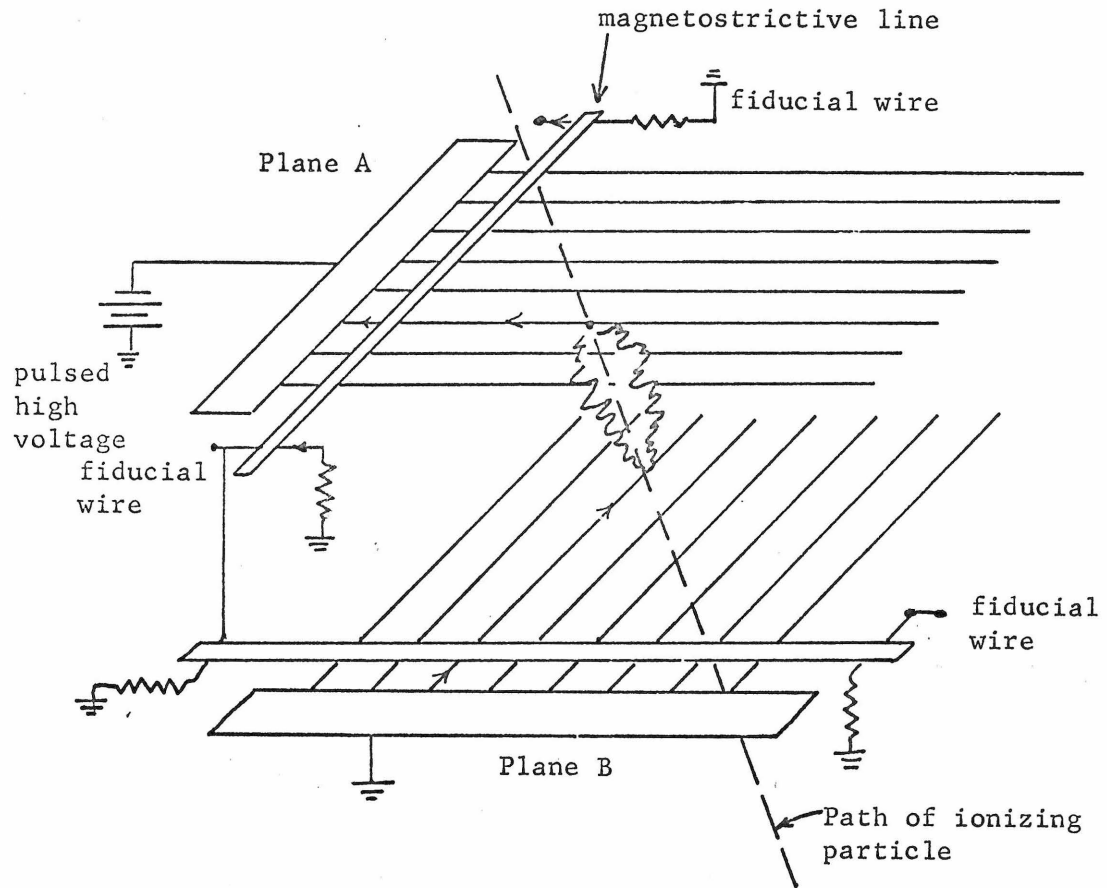


Figure 2.11

Schematic of the operation and components of the wire spark chambers. A spark formed along the path of the ionizing particle. Current flowed through the wires (denoted by arrows) coupled by the spark. Marker pulses were placed on the magnetostriuctive lines by the fiducial wires.

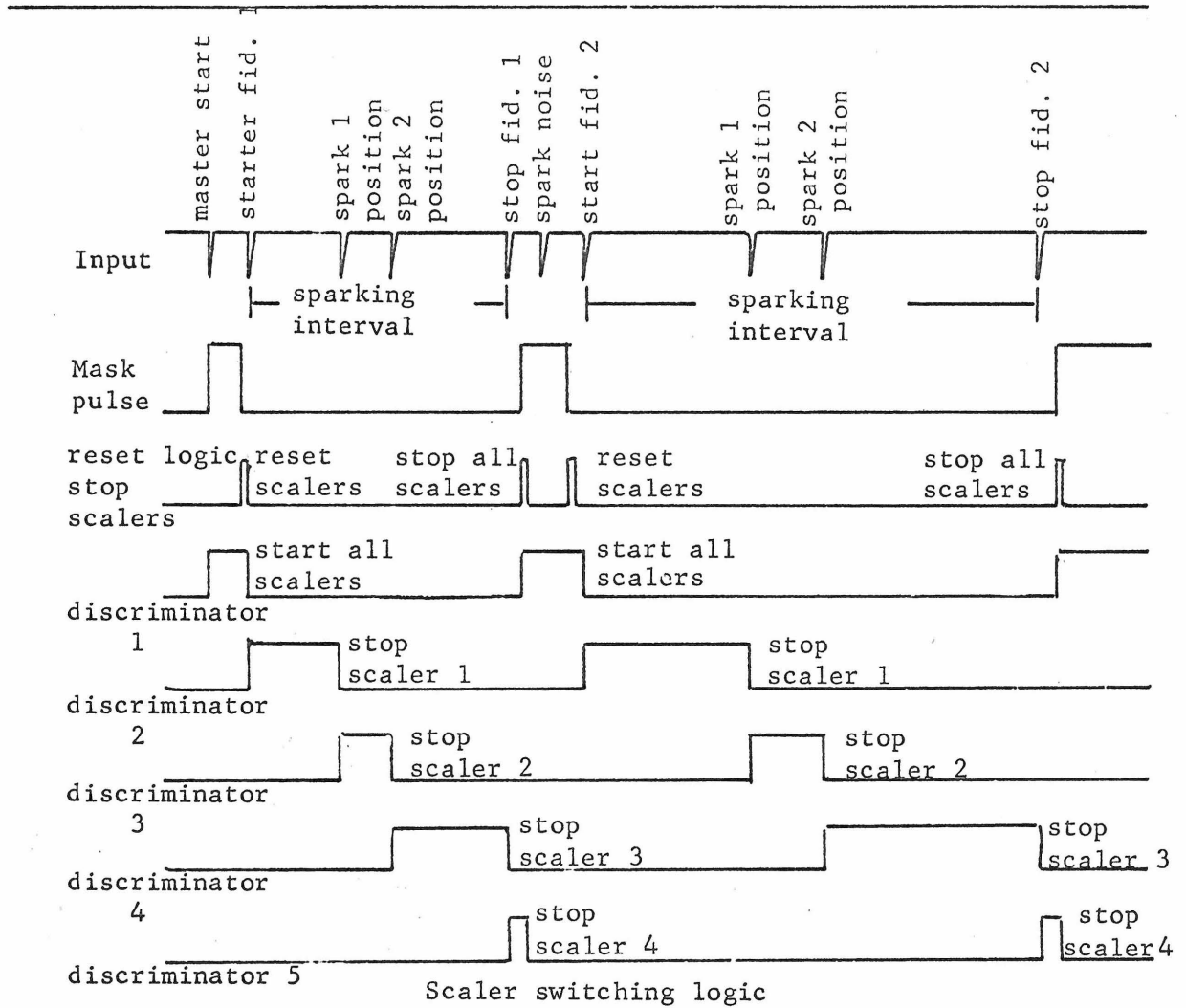
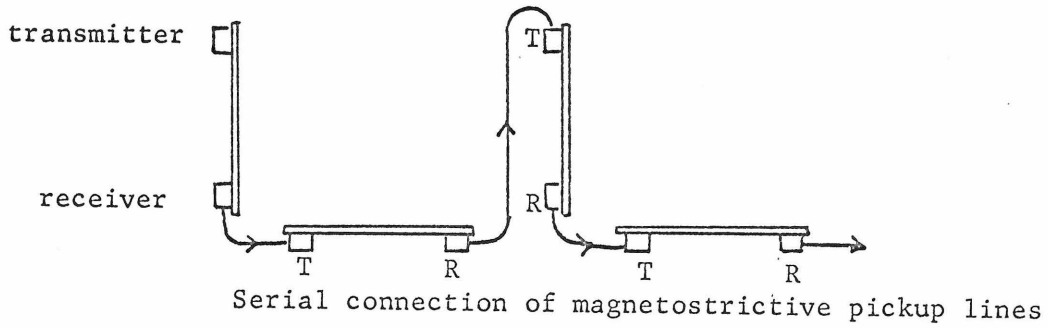


Figure 2.12

The wire spark chamber signals and the digitizer operation

6. Over-all Timing, the Interface, and the PDP-8 Computer

In order to coordinate the information from the trigger logic and the wire chambers, a master gate controlling the fast logic,²⁴⁾ an interface, and a PDP-8 computer were used. The over-all timing diagram for the data recording process is given in Figure 2.13.

The beam spill lasted roughly 400 msec of each 2.4 sec between machine pulses. During the approximately 2 seconds of beam-off time, the fast logic electronics were gated off by the master gate. At the beginning of the beam spill, a beam start pulse was sent from an AGS beam monitor system which closed the master gate and activated the electronics. Approximately 180 nsec after a trigger producing event occurred, the master gate received an event signal from the fast logic electronics system and gated it off. This fast event signal lasted only 30 μ sec but was supplemented by a busy signal sent from the interface which arrived at the master gate ~ 2 μ sec after the event had occurred and kept the fast logic gated off for a total of 20 msec. After this time, the master gate activated the fast logic electronics and the system was ready to detect another event. At the end of the beam spill, a beam stop pulse sent to the master gate from the beam monitor system gated the fast logic electronics off.

The purpose of the interface was to control the wire spark chamber digitizing system and to read the digitized spark positions along with additional counter bit information into the PDP-8 computer. In addition, at the beginning and end of each run, the

interface read run labelling and run symmetry information from digit switches and scalars into the computer.

Approximately 180 nsec after the trigger producing event occurred, the interface received a start pulse. For the next 50 nsec, delayed signals from selected counters, which fired when the events occurred, set bits in the interface which were then clamped before sparking occurred in the wire spark chambers (about 300 nsec after the event). After the wire spark chambers had sparked, the counter bits were read into the computer and reset, and a busy signal was sent to the master gate. The mask and the scalar reset and stop pulses were then sent to the digitizer in the order described in Section 5.

During a 20 μ sec duration of the mask pulses, data from the 4 scalars used in the digitizing system were read into the computer. These 4 data breaks took a total time of about 8 μ sec to complete.

About 3 msec after the event occurred, all the counter bits and digitized wire spark chamber information had been read into the computer. However, the interface remained on and the trigger logic electronics off for a total time of about 20 msec to allow the wire spark chambers to completely recover (Appendix B).

The principal purpose of the PDP-8 computer used in this experiment was to write the data received from the interface on magnetic storage tape. In addition, at the end of each run, it calculated and printed out on a teletype the wire spark chamber efficiencies and individual counter bit totals for all events

recorded during the run.²⁵⁾

The data were recorded on magnetic tape in the following format:

- a) 24 60-bit words each containing 4 12-bit numbers corresponding to the 4 digitizer scalar readings and a 12-bit blank. The 24 words corresponded to the 24 coordinates on the 12 wire chambers.
- b) 1 60-bit word containing 48 bits of counter information.
- c) 5 blank bit words.

At the beginning and end of each run, 30 60-bit words numbering and describing each run and containing scalar readings of \bar{p} fluxes and the number of triggered events were also written on the tape.

A maximum number of 15 events/beam pulse could be accepted, the limitation being due to the size of the buffer between the PDP-8 computer and the magnetic tape drive. However, since a trigger rate of 15 events/beam pulse was achieved only at 2.4 GeV/c and a maximum of 20 events each with a dead time of 20 msec could be recorded in a 400 msec beam pulse, this limitation was not severe.

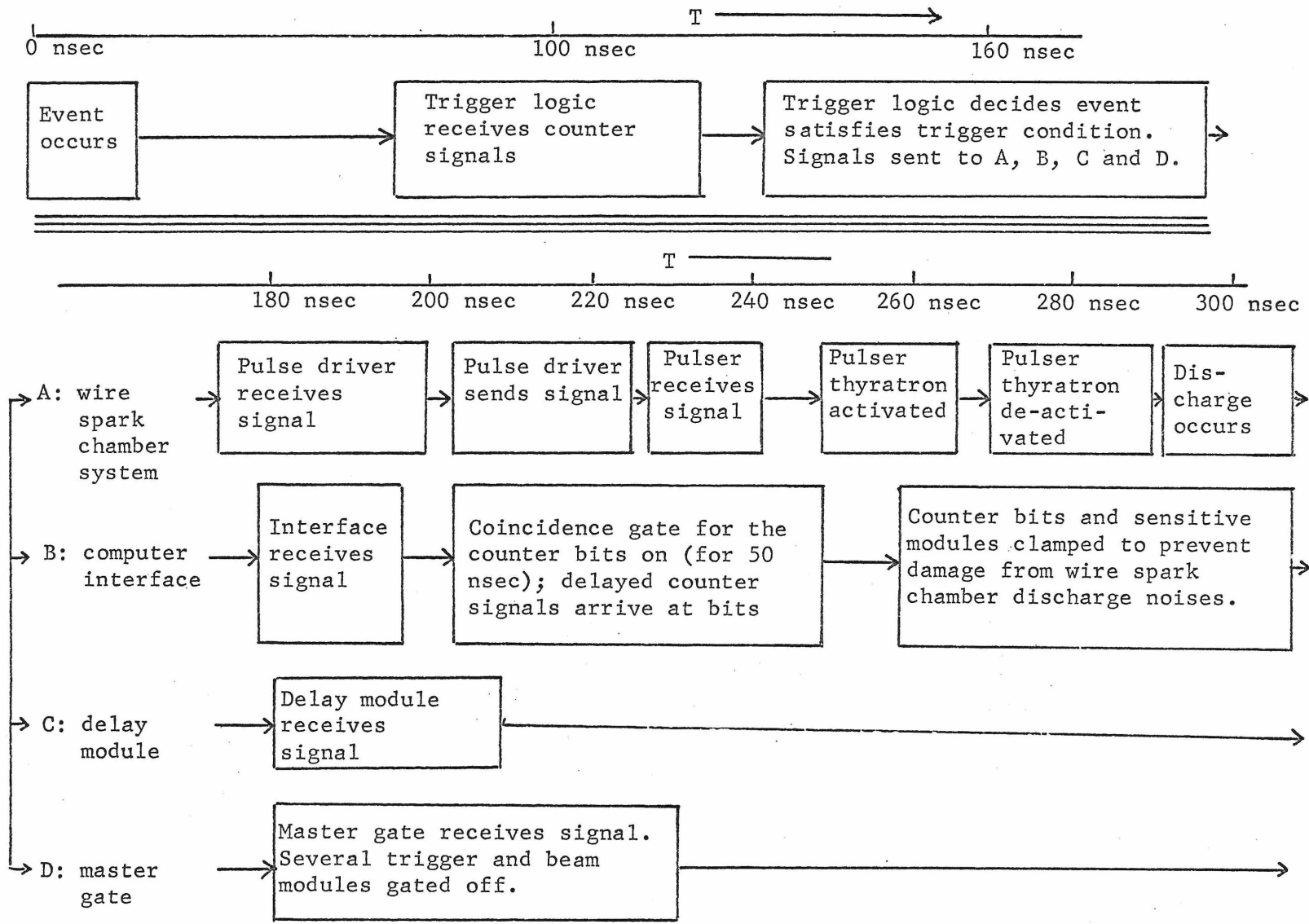
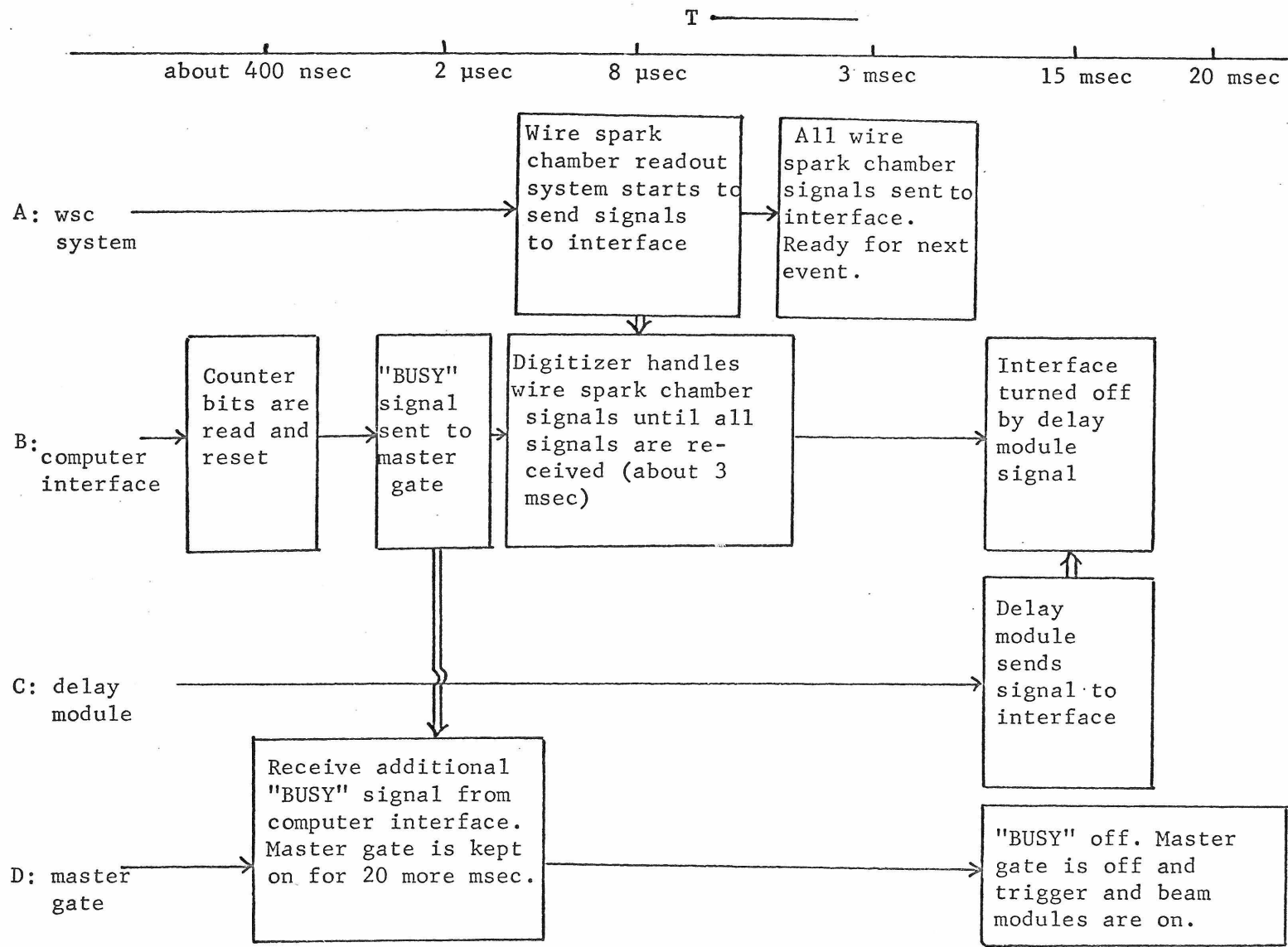


Figure 2.13: Trigger and event recording timing diagram (continued on the next page). All timings are approximate.



7. Monitoring the Experiment

In any complicated particle accelerator experiment it is imperative to carefully monitor the beam, the experimental equipment, and the data being recorded as close to the time of actual data taking as possible to insure the proper operation of all parts of the experiment. This section describes the methods used to monitor the experimental equipment and the data in this experiment (the beam and the operation of trigger scintillation counters were monitored by the scalars described in Sections 1 and 4).

Periodic measurement (~ 2 hrs) of the resistance of two 300Ω 1/4 watt carbon resistors (whose resistance is temperature dependent) located at the top and bottom of the hydrogen target insured that the target was kept filled with liquid hydrogen. A scalar which continuously displayed the nuclear magnetic resonance frequency of a deuterium oxide probe (high momenta) and a water probe (low momenta) monitored the magnetic field of the bending magnet D_4 .

Signals from the receiver amplifiers of each of the 24 wire spark chamber coordinates could be separately viewed on the screen of an oscilloscope. Another oscilloscope was used to display the mask signal produced by the interface.

During a run the data taking could be interrupted and the last event read into the computer printed out by the teletype. This

print-out provided a spot check that all the wire spark chambers, the digitizing system and the interface were working properly.

At the end of each run, the computer printed out crude wire spark chamber efficiencies (Appendix C) and individual counter bit totals for the run. Also, at the end of the run, all the scalar readings for the quantities scaled during the run were typed out. Beam scalar ratios and trigger rates were then plotted for each run to check for instabilities in the beam and the experimental apparatus.

Within two hours after the completion of data recording on a given magnetic tape (2 - 8 runs), accurate wire spark chamber efficiencies and crude numbers of annihilation events per run were available from a printout of the first stage analysis program run on Brookhaven's CDC-6600 computer.²⁶⁾ Consistently high values for the over-all event detection efficiency (> 90%) insured reliable wire spark chamber data.

The operation of the high voltage and magnet current supplies and the efficiencies of the scintillation counters were expected to remain approximately constant in time. However, counter voltages, beam magnet currents, and wire spark chamber high voltages, and gas flows were checked and recorded every eight hours. B and R scintillation counter efficiencies were measured using B and R efficiency counters several times during the running of the experiment and were typically >99%. The relative efficiencies of P counters $P_1 - P_6$ were determined from particles traversing two

counters in the 1/2" region of overlap and were typically $> 99\%$. Wide angle counters such as B_6 and $P_7 - P_{10}$, whose efficiency could not be easily determined from efficiency counters because of low event rates, were initially plateaued with a source and the output pulse height from the phototube of each of these counters was frequently checked using the source throughout the experiment. It is assumed that their efficiencies were $> 98\%$.

Table 2.5 gives wire chamber event efficiencies at each momentum run in this experiment for both the regular and wide angle triggers. The columns titled magnet track events are for those events in the regular trigger whose forward particles produced a track in the wire spark chambers downstream of the D_4 magnet. The estimated efficiencies of the B, P, and R counter arrays for the three types of events listed above are given in Table 2.6.

Table 2.5

Wire Spark Chamber Event Efficiencies

<u>Incident \bar{p} momentum</u>	Positive Particle Forward			Negative Particle Forward		
	<u>Magnet Track Events</u>	<u>Regular Events</u>	<u>Wide Angle Events</u>	<u>Magnet Track Events</u>	<u>Regular Events</u>	<u>Wide Angle Events</u>
.700	.994	.987	.938*	1.000	.989	.942*
.810	.993	.993	.950*	-	-	-
.870	.981	.988	.988	.988	.992	.993
.990	.984	.986	.951*	.984	.976	.954
1.120	.984	.984	.985	.960	.973	.973
1.340	.953	.919	.921*	.940	.904	.915*
1.450	.975	.963	.916*	.969	.972	.934
1.590A	.825	.815	.786	.872	.846	.851
1.590 B	.985	.981	.985	.967	.958	.955
1.590C	.945	.944	.920*	-	-	-
1.710	.942	.937	.915*	.961	.955	.918*
1.815	.981	.981	.983	.987	.982	.979
2.000	.957	.952	.917*	.945	.942	.906*
2.160	.947	.966	.960	.988	.977	.976
2.260	-	-	-	.924	.927	.883*
2.400	.974	.955	.956	.970	.968	.972

* Beam track probability times multiplied efficiencies of chambers 2-7.

Table 2.6

Scintillation Counter Efficiencies

<u>Event Type</u>	<u>Counter Array Efficiency (%)</u>			<u>Over-all Counter Efficiency (%)</u>
	<u>B</u>	<u>P</u>	<u>R + Q</u>	
Magnet track	98 ± 1.0	99 ± 0.5	99 ± 0.5	96 ± 1.2
Regular	98 ± 1.0	99 ± 0.5	99 ± 0.5	96 ± 1.2
Wide angle	98 ± 1.0	98 ± 1.0		96 ± 1.4

CHAPTER III

ANALYSIS OF THE DATA

Introduction

In order to convert the spark coordinate and counter bit information written on magnetic tape for each event into proton-antiproton annihilation cross sections, each event was reconstructed by means of a reconstruction computer program which was run on the Brookhaven CDC-6600 computer. Coplanarity, copunctuality, target vertex, kinematics and, where applicable, momentum cuts were applied to the data to yield the numbers of two charged pion and kaon final state annihilation events in bins of $\Delta \cos \theta_{\text{cm}} = .02$. These were combined with differential solid angle acceptances calculated by the Monte Carlo method to yield differential cross sections at each momentum.

This chapter describes this analysis procedure in detail. The reconstruction procedure is described in Section 1. The cuts and background subtractions applied to the reconstructed data are described in Section 2. Section 3 describes the Monte Carlo calculation. Over-all normalization and angular corrections applied to the final data are described in Section 4. Finally, the cross section calculation is described in Section 5.

1. The Reconstruction Procedure

The first stage of the off-line data analysis consisted of reconstructing particle tracks from the wire spark coordinate data. Those events which had roughly the correct topology and whose track angles satisfied the kinematics constraints on two final state meson annihilations were written on magnetic tape for subsequent analysis.

In order to describe the track finding procedure it is convenient to divide the coordinates of the wire spark chambers into six regions. Regions 1, 3, and 5 were defined as the horizontal view and regions 2, 4, and 6 the vertical view of each set of 4 wire spark chambers (1-4), (5-8), and (9-12), respectively. Trackfinding was done separately in each region.

Consider a particular region and a particular event. For trackfinding purposes the lowest numbered chamber of a set was defined as chamber 1 (chamber furthest upstream) and the highest numbered chamber as chamber 4. Let the minimum number of measured sparks for that event in chambers 3-4 be M . Then all possible two spark tracks formed using spark coordinates from chambers 1 and M and chambers 2 and M were found and extrapolated to the other chambers in the region. When sparks could be found in these chambers within a region of ~ 7.5 mm from the extrapolation, a line was fit to the 4 sparks using a least squares procedure. If $\chi^2 > 6.6$ for this fit or if any spark used in the fit had been used to form another 4 spark track with a lower χ^2 the track was rejected; otherwise it was considered a good 4 spark track. After all 4 spark tracks had been obtained in the region, the spark coordinates used to form them were

removed from consideration and a search was made for all three spark tracks in that region.

Once all the tracks had been found in each of the six regions they were identified in the following manner. In region 1 (the horizontal view of the upstream chambers (1-4) the track with a slope of less than 50 mrad was classified as a beam track. In region 2, if there was more than one track, the track with the correct hodoscope bit or the one satisfying coplanarity requirements was chosen as the beam track. Other tracks in regions 1 and 2 were classified as backward scattered tracks. The requirement that a track be present in the small beam region eliminated the need for rotating the wire chambers to remove two track ambiguities in regions 1 and 2. Any tracks found in regions 3 and 4 were classified as forward tracks and any tracks in regions 5 and 6 were classified as magnet tracks.

Frequently ($\sim 20\%$ of the time) extra tracks (more than 1 in regions 3-6 and more than 2 in regions 1-2) were found in the various regions for a particular event. These were removed using the procedure described below which was terminated when no extra tracks remained in any region.

The horizontal views were considered first. Extra beam tracks which did not pass through the correct element of the beam hodoscope (Chapter II, Section 1) were removed. Then tracks in regions 1 and 3 having differences in slope of less than 10 mrad and differences in x vertex at $z = 0$ of less than 3 mm were removed unless in so doing less than 2 tracks remained in region 1 or no tracks

remained in region 3. In these cases only the track in the multiple track region was removed.

All track vertices were required to be within the target volume. Tracks which formed vertices with other tracks outside this volume were removed. The vertices of pairs of tracks in region 1 which were more than 8 mm from tracks in region 3 were also removed.

If there were still extra tracks in region 1 or region 3 or both, then the pair of tracks in region 1 and the track in region 3 forming the best vertex was chosen as the correct set of event tracks. Although the beam track could be lost in events in which more than one backward scattering track emanated from the same vertex, these events involved at least three final state particles and were not events of interest in this experiment.

This procedure was then repeated in the vertical view. Since the beam and backward scattered tracks could often be colinear in the vertical view, only one track was required in region 2 and was considered the vertical projection of the best pair of tracks in region 1.

Following the tracksorting procedure described above, a candidate for a two meson final state proton-antiproton annihilation event was required to have a beam track, a backward scattered track and a forward scattered track. In addition, the following requirements had to be satisfied by these tracks:

- a) The three tracks were required to intersect at a vertex with a copunctuality limit of 1 cm.²⁷⁾
- b) The track vertex had to be formed in the target volume.

- c) The three tracks were required to be coplanar with ± 50 mrad²⁸⁾
and
- d) The angles the forward and backward scattered tracks formed with the beam track were required to satisfy two meson final state kinematical constraints.²⁹⁾

Events with the correct number of tracks and whose tracks satisfied requirements a-d were considered acceptable events for further study and written on magnetic tape for subsequent analysis.

2. Event Determination

Events having approximately the correct topology and kinematics after reconstruction were then studied further by imposing tighter kinematical and topological cuts and calculating the final state particle masses assuming equal mass two particle final states. Those events with squares of final state particle masses between $-.14$ and $.16 \text{ GeV}^2$ were classified as two pion annihilations, those with squares of final state particle masses between $.16$ and $.35 \text{ GeV}^2$ were classified as two kaon annihilations. In reactions in which the reaction products travelled in directions nearly colinear with the beam line, the forward going particle traversed the bending magnet D_4 and the wire spark chambers 9-12 downstream of the magnet and its momentum could be determined. For these reactions the squared mass of the final state particles was obtained from knowledge of the beam particle momentum, the angle the backward particle formed with respect to the incident beam particle line, and the momentum of the forward particle.

In reactions in which the forward going particle formed a larger laboratory angle ($\sim 7^\circ$) with respect to the incident anti-proton beam line, the forward particle could still traverse the bending magnet but did not traverse the wire spark chambers 9-12. For these reactions the sign of the forward particle's charge could be determined from scintillation counter information downstream of the magnet (the R counters) and the squared mass of the final state particles could be calculated from knowledge of the beam particle

momentum and the laboratory angles formed by the final state reaction particle tracks with respect to the beam line.

Forward going particles in those reactions in which the laboratory angle between the incident antiproton beam line and the forward going particle was greater than $\sim 20^\circ$ were not able to traverse the D_4 bending magnet and hence the sign of their charge could not be determined. However, the final state particles in these reactions triggered the wide angle P and B counters (Section II-4) and the squared mass of the final state particles could be determined as above from knowledge of the beam momentum and the laboratory angles of the reaction products with respect to the beam line.

The coplanarity distribution and the distribution of vertices along the beam line are shown for the trigger set for a negative forward going particle at .99 GeV/c in Figures 3.1 and 3.2, respectively. Reactions whose final state particles were coplanar with the beam line to within ± 15 mrad were considered event candidates, reactions whose final state particles were coplanar with the beam line to between -30 and -15 mrad and 15 and 30 mrad were considered background events for multiparticle final state reactions (> 2 reactions particles) and used in the background subtraction described below. Z vertex cuts were made at ± 18.73 cm. The peak in the number of events at ~ -30.0 cm in Figure 3.2 are reactions occurring in the third beam defining counter S_3 . The accurate vertex definition $\lesssim .5$ cm eliminated the need for empty target subtractions.

Figures 3.3 and 3.4 show numbers of final state particle masses squared in mass squared bins of $.01 \text{ GeV}^2$ for all reactions whose final state particles were coplanar with the beam line to within ± 15 mrad, and between -30 and -15 mrad or 15 and 30 mrad, respectively. Those events giving calculated final state particle squared masses in the pion or kaon event regions but whose calculated coplanarities were between -30 and -15 mrad or 15 and 30 mrad were subtracted bin by bin in $\cos \theta_{\text{cm}}$ from events with squared masses in the pion or kaon event regions with calculated coplanarities between ± 15 mrad. The net number of events after this subtraction in $\cos \theta_{\text{cm}}$ bins of $.02$ was used in the calculations of two pion and two kaon annihilation cross sections. Figure 3.5 shows the summed data with the background subtracted out.

By changing the coplanarity limits for background events from $15 \leq |\text{coplanarity}| \leq 30$ to $15 \leq |\text{coplanarity}| \leq 45$ the effect of the slope in the coplanarity background was studied and was shown to have negligible effect in the background subtraction used in the cross section calculation. Plots of the distribution of coplanarity for calculated final state particle masses outside the acceptable limits for two pion or two kaon annihilation reactions show slight peaking for near zero coplanarity indicating the presence of $< 1\%$ π^- contamination in the beam. This contamination is treated as an over-all normalization uncertainty and included in the error due to uncertainties in the analysis discussed in Section III-5.

Events giving final state particle masses at the extremes of

the acceptable two pion and two kaon limits have been studied and found to be events whose final state particles formed small angles with respect to the beam line. Small measurement errors in such events cause large errors in the final state particle masses obtained from a calculation using the beam momentum and laboratory angles to determine these masses. These events, however, had a high probability to have their final state forward going particle traverse the wire spark chambers downstream of the magnet and the final state particle masses could then be accurately calculated from the measured momentum of the forward going particle. Changing the pion and kaon annihilation mass squared limits by $\pm .02 \text{ GeV}^2$ produced negligible changes in the values of the cross sections.

The tight kinematical and topological cuts are listed below:

- a) Event copunctuality was required to be less than .5 cm.
- b) Events vertices were required to lie within a 4 cm diameter from the beam line through the target center, and
- c) Event tracks were required to lie within wire chamber fiducial volumes in wire spark chambers 1, 8, and 12 slightly smaller than the sensitive areas of the chambers.

The wire chamber fiducial cuts were made to insure that a backward going final state particle resulting from an annihilation in the target traversed a trigger counter and that a forward going final state particle resulting from an annihilation in the target had negligible probability of hitting a magnet pole face. The wire chamber fiducial cuts made to the data for the various triggers and the

target radius cuts were consistent with those used in the Monte Carlo calculation of the experimental detection efficiency of the apparatus discussed in Section III-3. Event losses due to the cut on copunctuality have been studied and found to be negligible ($\lesssim 1\%$).

Figure 3.1. .99 GeV/c Incident \bar{p} momentum
Negative particle forward

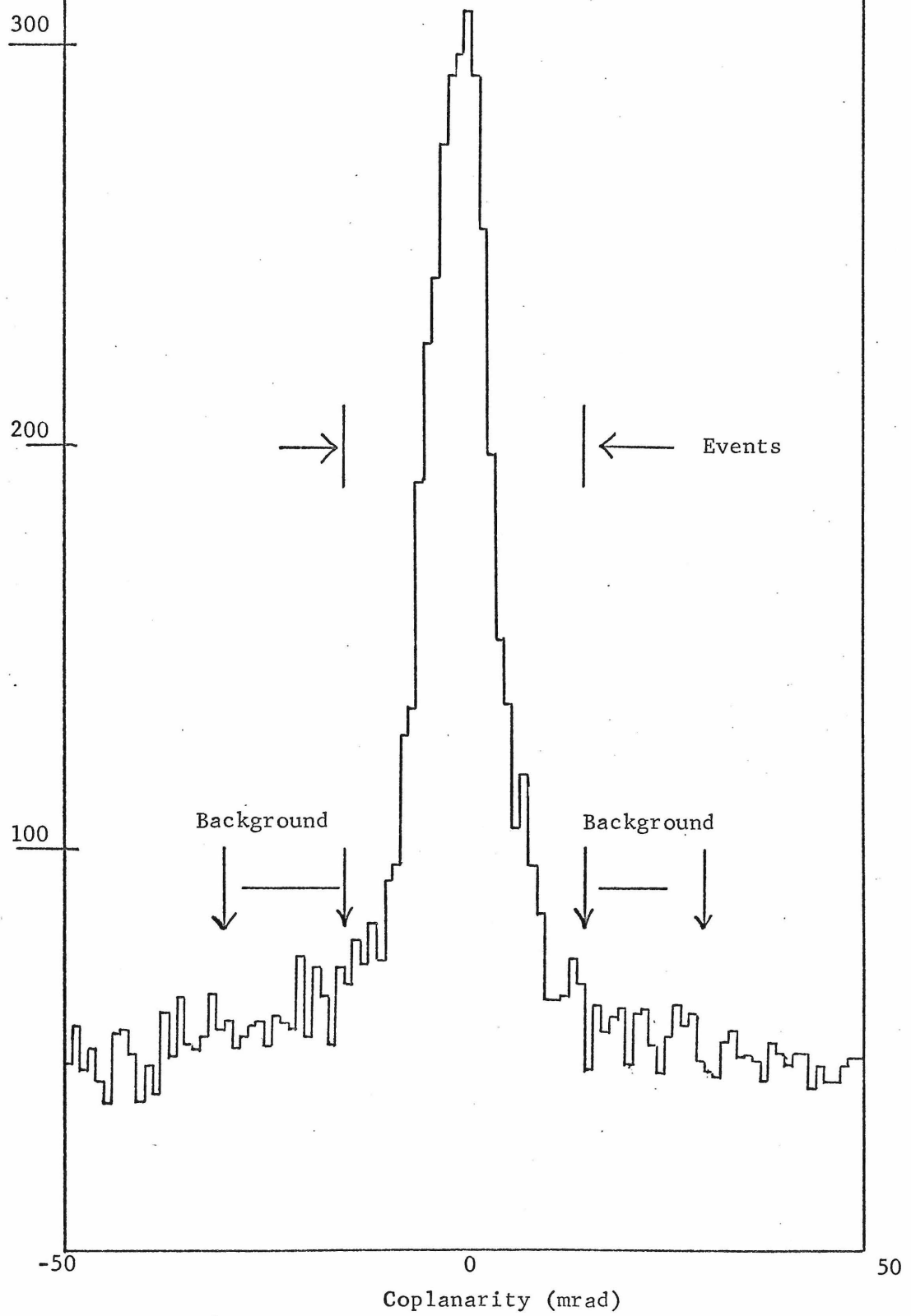


Figure 3.2

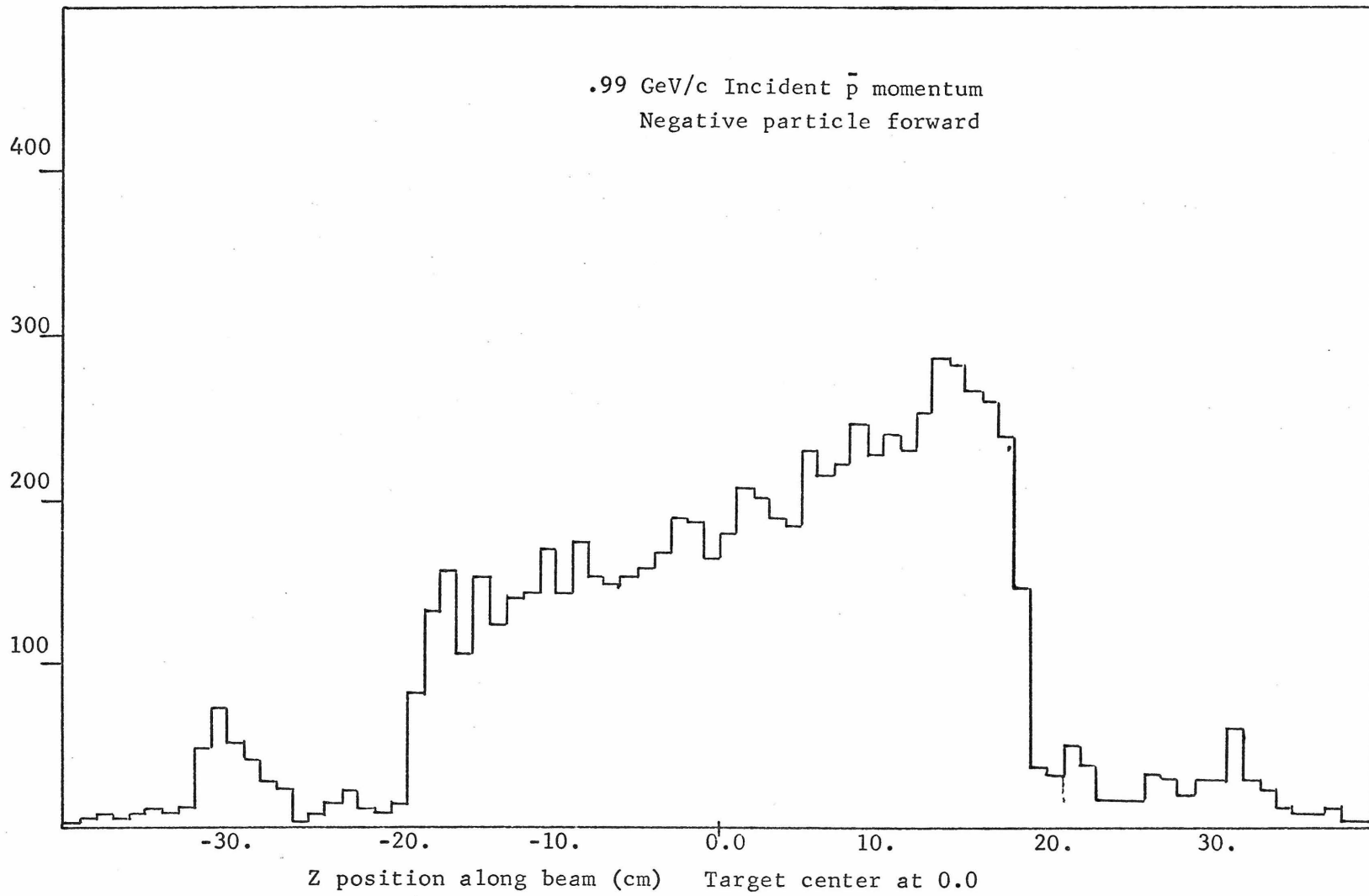


Figure 3.3

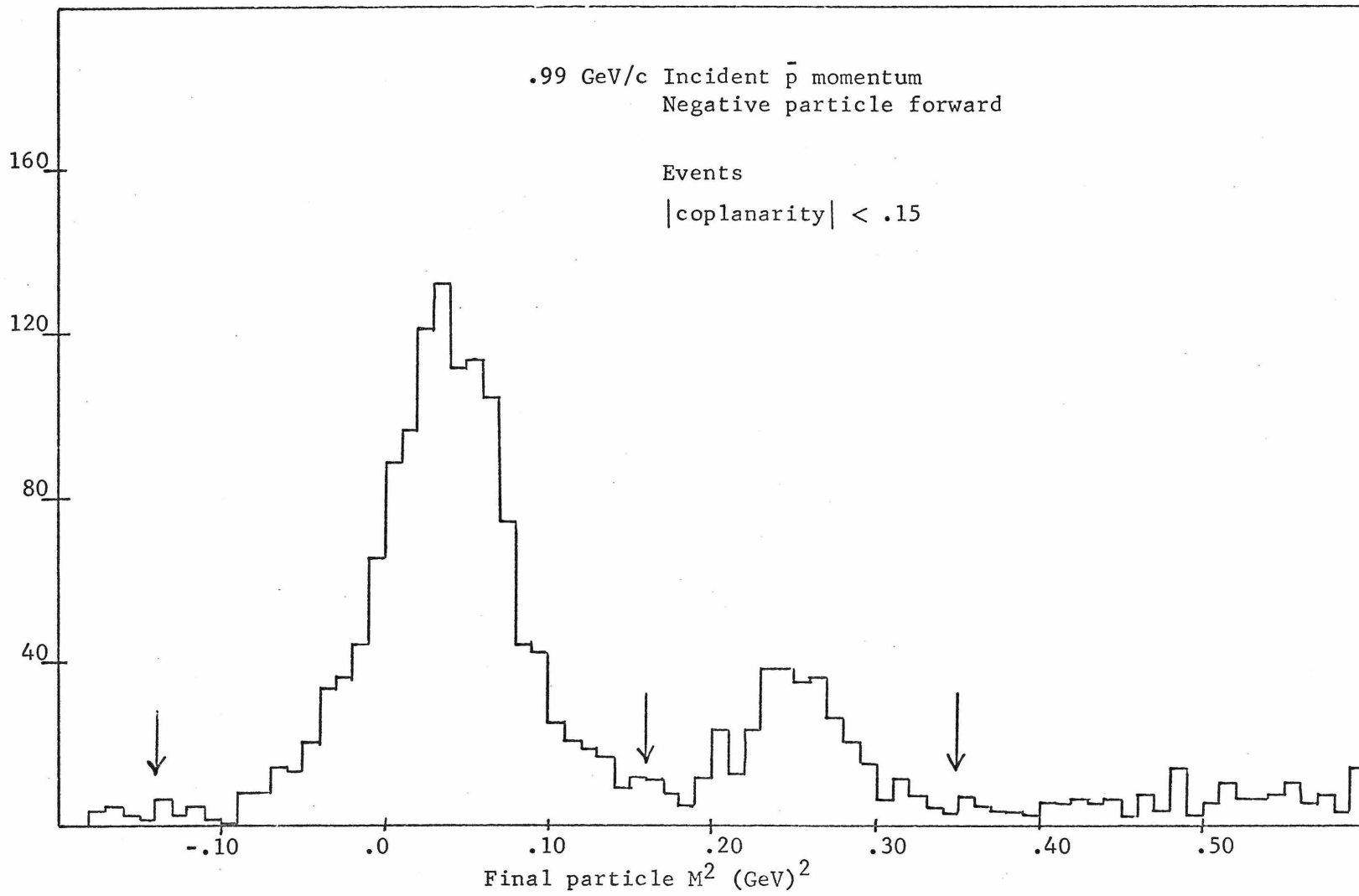


Figure 3.4

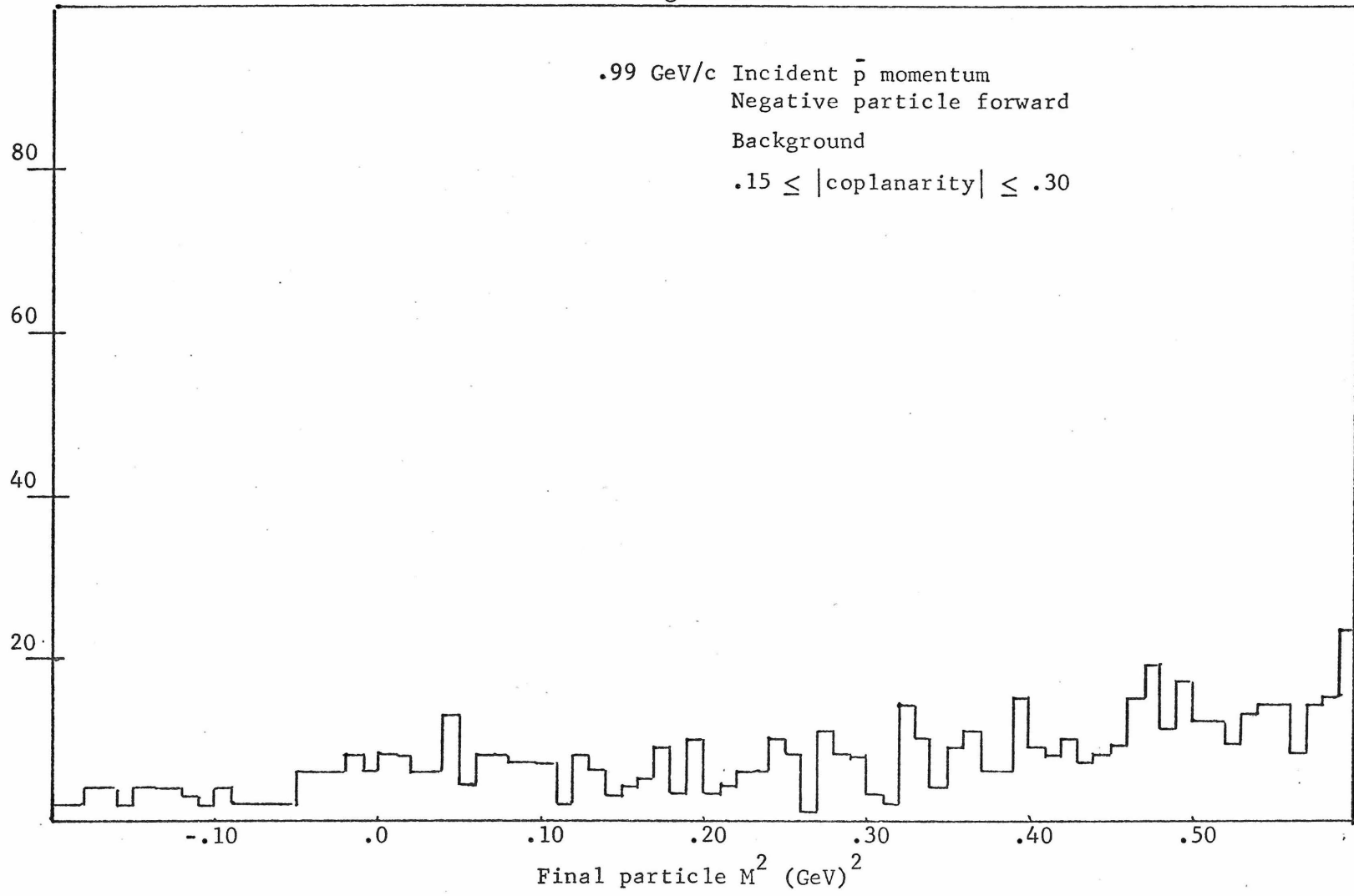
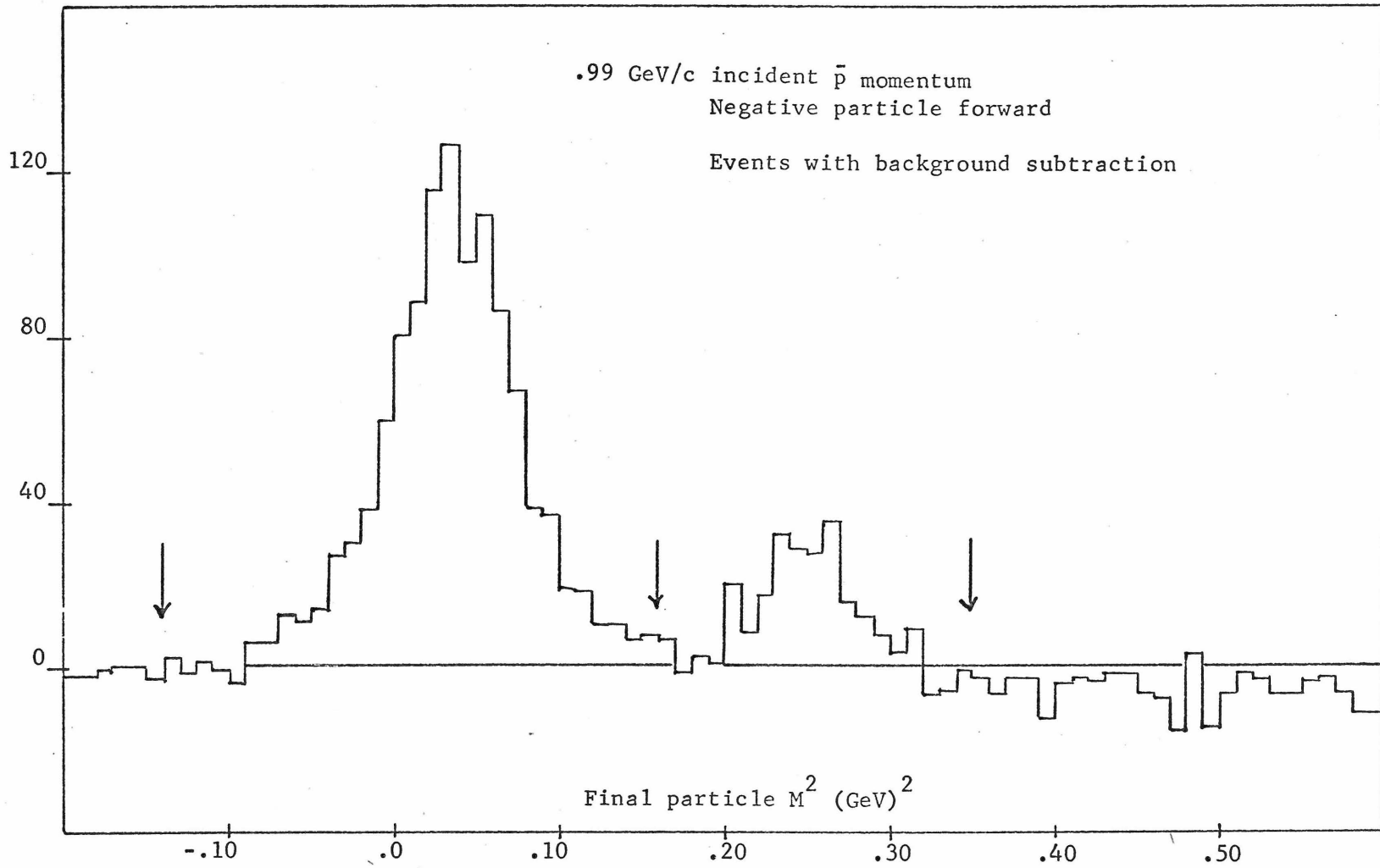


Figure 3.5



3. The Detection Efficiency of the Apparatus

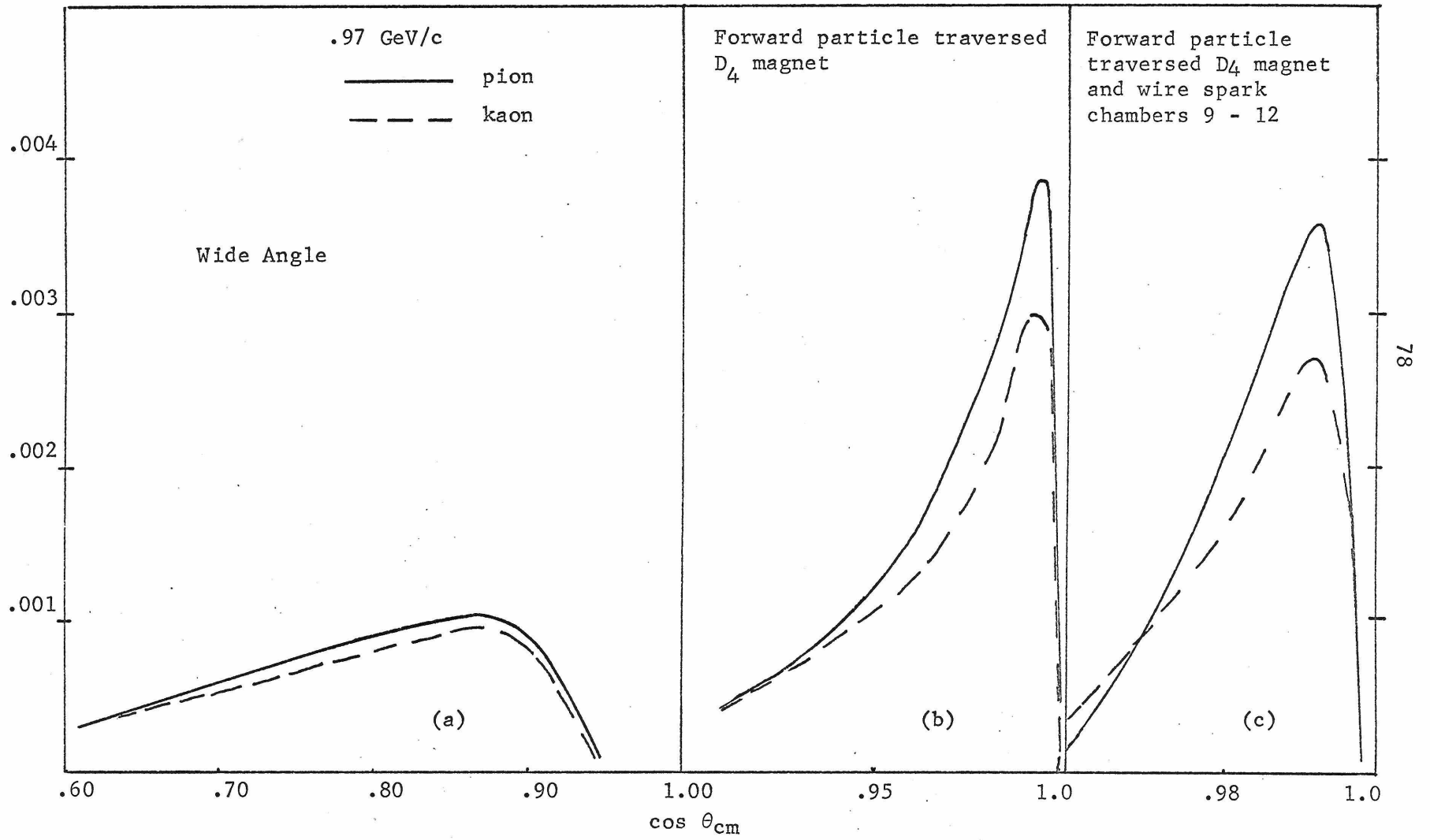
In order to determine annihilation cross sections, it is necessary to know the experimental event detection efficiency as a function of the center-of-mass angle between the incident antiproton and proton and the outgoing two mesons. This was calculated using the Monte Carlo method by generating two-body final states at random in $\cos \theta_{\text{cm}}$ bins and ϕ angular regions in which there was a non-vanishing experimental particle detection efficiency in the laboratory, and using two pion or two kaon annihilation kinematics to find corresponding laboratory angles.³⁰⁾ Those pion or kaon events which satisfied trigger conditions and which could be reconstructed into acceptable pion or kaon annihilation events using the same reconstruction process which was used for the data divided by the number of trials in each $\cos \theta_{\text{cm}}$ bin produced the efficiency of the experimental apparatus for that bin. Final state pion or kaon decay and multiple scatterings were included in the simulated events. Ten thousand trials for each trigger at each momentum gave statistical uncertainties in the efficiency of $\sim 10\%$ for each bin.

The detection efficiency of the apparatus was separately calculated for those reactions in which the forward going particle was required to traverse the magnet and the wire spark chambers downstream of the magnet (9-12), those reactions in which the forward going particle was required to traverse the magnet but not the wire spark chambers downstream of the magnet, and those reactions in which the forward going particle was only required to traverse chambers 5 and 6 and the backward particle was only required to

traverse chambers 2, 3, and 4 (the wide angle events). Except for the wide angle events, backward going particles were always required to traverse the four upstream wire spark chambers 1-4 and the forward going particles were required to traverse either all downstream wire chambers 5-12 or chambers 5-8 if momentum information from the D_4 bending magnet was not required.

Figure 3.6 gives the two pion and two kaon experimental and solid angle acceptances at .99 GeV/c incident \bar{p} momentum as a function of $\cos \theta_{cm}$ for events whose forward particles were required to traverse wire spark chambers 9-12 (3.5c), events whose forward particles were required to traverse the magnet (3.5b) and wide angle events (3.5a). Final state particle decay is primarily responsible for the lower experimental efficiency for two kaon annihilations.

Figure 3.6



4. Systematic Corrections

In order to correct for experimental and event reconstruction inefficiencies, studies were made to determine the magnitudes of the systematic errors associated with this experiment. Corrections to the normalization were made to account for scintillation counter inefficiencies ($4 \pm 1.2\%$, Table 2.6) wire chamber inefficiencies (Table 2.5), event reconstruction inefficiencies ($7.0 \pm 1.1\%$), events lost to accidentals in the trigger veto counters ($1.3 \pm .3\%$) a flux correction for the absorption of beam in the hydrogen target ($\sim 10 \pm 1.5\%$, Table 3.1), and event losses due to final state particle nuclear interactions in the experimental apparatus ($\sim 4 \pm 2\%$, Table 3.2). Angular corrections other than those included in the beam absorption and nuclear interaction of final state particles include angular inefficiencies in the reconstruction procedure for events whose forward final state particle traversed the magnet ($3.5 \pm 3.5\%$) and for wide angle events ($1 \pm 1\%$ for $.7 \leq |\cos \theta_{\text{cm}}| < .8$ and $2.5 \pm 2.5\%$ for $.6 \leq |\cos \theta_{\text{cm}}| < .7$).

The wire chamber efficiency calculation was made from missing spark pattern information recorded with each event during the reconstruction procedure described in Section III-1. This calculation is described in detail in Appendix D.³¹⁾ The resulting event efficiencies tabulated in Table 2.5 were used to correct the data for wire spark chamber inefficiencies.

Event reconstruction inefficiencies were determined from scanning computer drawn pictures of each event and searching for

lost events. Roughly 2000 pictures of annihilation and πp scattering triggers were scanned. One of the major sources of inefficiency occurred in the reconstruction in wire spark chambers 1-4 due to spurious tracks found from spurious sparks in these chambers which removed one or more sparks from the correct beam track and prevented it from being found. In the beam region spurious sparks were sufficiently close to real beam track sparks so this could happen $\sim 3\%$ of the time.

Another major source of difficulty occurred when more than two tracks were present in the upstream chambers 1-4 or more than one track was present in chambers 5-8. (The number of times extra tracks were present in chamber 9-12 was negligible.) An extra track in the beam region resulting from a beam particle which did not interact in the target and gave a track in chambers 5-8 could often fool the tracksorting procedure into throwing away the forward scattered particle track from an event with the correct topology and consequently losing the event. This was particularly true for the forward particles from wide angle event triggers which had additional non-interacting beam tracks present and resulted in the angular corrections applied to those events. The over-all inefficiency of the extra track removal procedure was estimated at $\sim 15\%$ and since it was used on 15-20% of all the data, the resulting over-all correction is estimated to be 2-3%.

Other sources of inefficiencies included a small under-estimation of wire spark chamber inefficiency $\sim 1\%$ and miscellaneous

reconstruction mistakes estimated at $\sim 1\%$.

In order to estimate the reconstruction inefficiency for small angle final state particle events, ~ 7500 triggers at $.99$ GeV/c were analyzed by calculating the mass of the backward scattered particles from knowledge of the momentum of the incident beam particle and the momentum and scattering angle of the forward scattered particle. The extra events found this way which could not be accounted for by inefficiencies in chamber 1-4 when a backward scattered track was required were used to estimate the reconstruction inefficiency when a backward track was required (normal analysis procedure) and resulted in a calculated inefficiency of $\sim 3.5\%$.

Target veto counters which surrounded the liquid hydrogen target and were used to veto $\bar{p}p$ annihilations into more than three particle final state events gave spurious noises pulses which rendered the trigger circuit dead for $\sim 1.3\%$ of the time data were being taken. The percentage of events lost are estimated to be equal to the percentage of trigger logic dead time.

Losses due to nuclear interaction of final state particles given in Table 3.2 are primarily due to interactions in the hydrogen target after annihilation and interactions in the P scintillation counters upstream of the magnet for events whose forward going particles traversed the magnet. Total cross sections for $\pi^{\pm}p$ with incident pion momenta between 1.4 and 3.0 GeV/c average to about 32 mb for π^+p and 34 mb for π^-p with the average kaon total cross sections $\sim 2/3\sigma_{\pi p}$ ³²⁾. At these momenta $3/4$ of the total cross section

is due to inelastic scattering. Making the assumption that any event having a final state particle involved in an inelastic nuclear interaction was lost and any event having a final state particle involved in an elastic nuclear interaction was lost except for small angle events whose forward going particle scattered elastically in the hydrogen target, the corrections given in Table 3.2 are obtained. A small angle scatter of the forward going particle in the hydrogen target in such a small angle event would still be likely to give a calculated final state particle mass squared within the acceptable limits.

The beam absorption correction was made by folding the number of beam antiprotons lost as a function of z position along the beam line into the event detection efficiency of the apparatus as a function of z . Total $\bar{p}p$ cross sections between .7 and 2.4 GeV/c incident antiproton momentum average ~ 100 mb.³³⁾

The over-all normalization multiplicative factor applied to the uncorrected data ranged from ~ 1.37 at .70 GeV/c to ~ 1.29 at 2.40 GeV/c incident antiproton laboratory momentum. The angular correction multiplicative factor applied to the uncorrected data was 1.00 in the center of the measured angular region and averaged ~ 1.03 at the extremes.

A radiative correction which has not been applied to the data has been calculated using the method described by Fong¹⁾. This correction was found to be $\sim 6\%$.

Table 3.1

Beam Absorption Corrections

<u>Incident \bar{p} momentum</u>	Positive Pion Forward			Negative Pion Forward		
	<u>Magnet Track Events</u>	<u>Regular Events</u>	<u>Wide Angle Events</u>	<u>Magnet Track Events</u>	<u>Regular Events</u>	<u>Wide Angle Events</u>
.700	12.4%	12.8%	16.1%	13.0%	17.8%	16.2%
.810	12.6	15.0	14.1			
.870	10.7	10.9	11.3	10.5	11.3	11.5
.990	10.4	11.0	11.7	11.7	11.9	12.1
1.120	8.5	10.5	10.8	9.0	10.0	9.9
1.340	8.5	9.8	7.2	9.1	9.7	7.4
1.450	8.1	8.5	7.9	9.0	9.7	8.2
1.590	8.4	10.3	7.1	8.7	10.7	7.6
1.710	7.8	9.2	7.0	9.0	9.7	6.7
1.815	6.3	7.8	6.2	8.7	8.7	7.0
2.000	6.8	8.6	4.9	8.2	8.4	6.3
2.160	6.2	6.8	4.0	7.1	8.1	4.5
2.260				6.8	8.2	5.4
2.400	6.3	6.5	3.5	7.1	7.3	4.4

Table 3.1 (continued)

<u>Incident \bar{p} momentum</u>	Positive Kaon Forward			Negative Kaon Forward		
	<u>Magnet Track Events</u>	<u>Regular Events</u>	<u>Wide Angle Events</u>	<u>Magnet Track Events</u>	<u>Regular Events</u>	<u>Wide Angle Events</u>
.700	18.1%	13.9%	11.7%	12.9%	11.0%	18.1%
.810	11.8	11.8	11.5			
.870	9.7	10.6	12.2	11.3	11.1	12.4
.990	9.9	11.1	10.8	8.7	10.8	11.6
1.120	9.8	9.6	10.9	8.5	10.3	10.7
1.340	10.3	10.9	8.1	10.1	9.7	6.3
1.450	9.3	8.6	7.7	7.2	9.4	7.6
1.590	11.6	11.3	4.8	5.2	8.0	3.6
1.710	9.4	8.8	7.2	6.9	7.5	7.5
1.815	10.3	6.8	6.6	8.5	7.9	5.8
2.000	7.5	6.0	5.9	7.9	8.2	5.6
2.160	10.2	8.1	4.1	7.4	8.0	4.1
2.260				6.3	7.8	5.6
2.400	2.2	7.4	4.2	8.2	7.8	4.6

Table 3.2

Nuclear Interaction Corrections

<u>Type Events</u>	<u>Pion Correction</u>	<u>Kaon Correction</u>
Magnet Track Events	$6.5 \pm 3.3\%$	$4.4 \pm 2.2\%$
Regular Events	3.0 ± 1.5	2.0 ± 1.0
Wide Angle Events	2.0 ± 1.0	$1.7 \pm .9$

5. Cross Section Calculation

In antiproton-proton annihilations producing two charged pion or two charged kaon final states, the number of pions (kaons) obtained in a given center-of-mass angular bin with mean angle θ

($\Delta N_{\pi, k}(\theta)$) is given by

$$\Delta N_{\pi, k}(\theta) = N_0 \exp(-n\sigma_{pp} z + 18.73)) n \frac{\Delta\sigma_{\pi, k}(\theta)}{\Delta\Omega} \Delta\Omega \Delta z \quad (3.1)$$

where N_0 is the number of antiprotons incident on the target, n is the number of scattering centers (protons) per unit volume in the target, $\Delta\sigma_{\pi, k}/\Delta\Omega$ is the probability per unit area for having an antiproton-proton pair annihilate into a pion (kaon) pair with each pion (kaon) forming a center-of-mass angle θ with respect to the center of mass incident antiproton or proton direction, $\Delta\Omega$ is the acceptance solid angle of the experimental apparatus for $\cos \theta$ in bins of .02, and z is the interaction position in the target (measured in centimeters along the beam line). θ was defined to be 0 when a negative pion (kaon) was colinear with the beam line and travelled in the same direction (+z).

The equation for the annihilation differential cross section obtained from equation 3.1 without the beam absorption correction discussed in Section III-4 is

$$\frac{\Delta\sigma}{\Delta\Omega}(\theta) = \frac{\Delta N(\theta)}{\Delta\Omega} \left(\frac{1}{N_0 n z} \right) = \frac{.63857}{N_0 \text{ (millions)}} \frac{\Delta N}{\Delta\Omega} (\cos \theta \text{ in bins of } .02) \quad (3.2)$$

Since data events with $|\text{coplanarity}| < 15 \text{ mrad}$ (N_T) con-

sisted of two pion and two kaon annihilations plus background and events with $15 \leq |\text{coplanarity}| \leq 30$ mrad (N_B) consisted of background events only $\Delta N(\theta)$ equalled $N_T - N_B$. The statistical error ϵ_s was calculated from the equation

$$\epsilon_s = \frac{\Delta\sigma}{\Delta\Omega}(\theta) \cdot \left(\frac{\sqrt{N_T + N_B}}{N_T - N_B} \right) \quad (3.3)$$

The cross sections calculated from the raw data were then averaged and smoothed. The final cross sections were calculated from these averaged cross sections from the equation

$$\left. \frac{d\sigma}{d\Omega}(\theta) \right|_{\text{final}} = \left. \frac{d\sigma}{d\Omega}(\theta) \right|_{\text{raw data}} (1 + N(\theta))$$

where $N(\theta)$ was the product of the normalization corrections discussed in Section III-4.

The errors quoted with the cross sections given in Chapter IV are statistical. The uncertainties in the over-all normalization estimated from the square root of the sum of squares of the normalization correction errors given in Section III-4, along with a 2% error in the density of liquid hydrogen in the target and a 4% error from uncertainties in the analysis and variations on normalization as a function of momentum, are listed in Table 3.3.

Figure 3.7 gives a flow chart of the analysis procedure used for calculating the differential cross sections with the number of triggered events surviving each stage of the analysis for .99 GeV/c with the trigger set for negative forward going particles.

Table 3.3

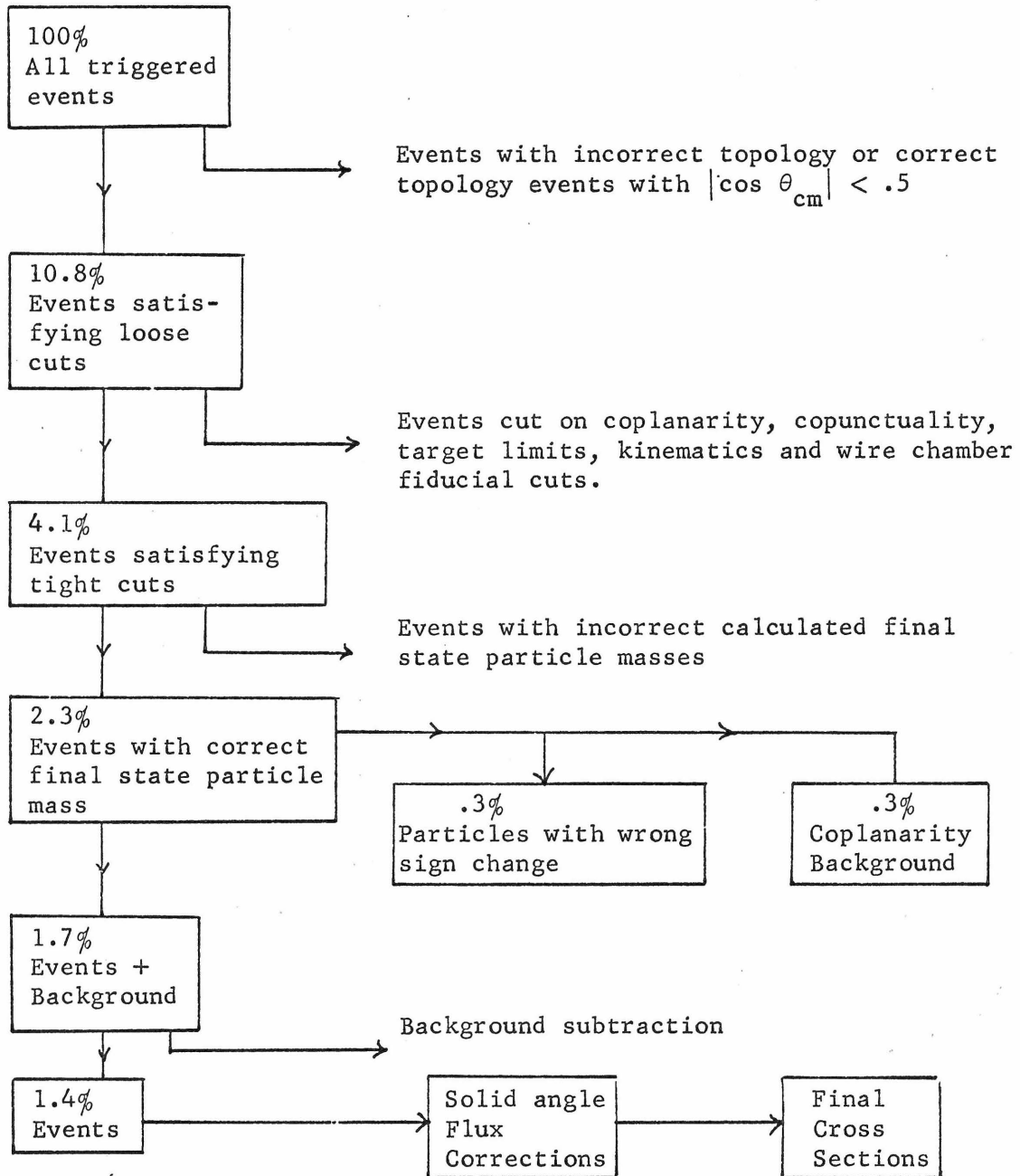
Uncertainty in Normalization

<u>$\cos \theta_{cm}$</u>	<u>Normalization Uncertainty</u>
Magnet Track Events *	6.40%
Regular Events *	5.40%
.80 - .70	5.50%
.70 - .60	5.95%
<u>Average Uncertainty</u>	<u>5.69%</u>

* Range of $\cos \theta_{cm}$ varies with momentum

Figure 3.7

Flow Chart of Analysis Procedure*



* Numbers are for .99 GeV/c with trigger set for negative forward particle.

CHAPTER IV

Results

This chapter gives the results of the experiment in tabular and graphical form. The tables and graphs are organized in the following way.

1. Table 4.1 gives the two pion annihilation data.
2. Table 4.2 gives the two kaon annihilation data.
3. Figures 4.1 and 4.2 which combine data from this experiment and the one of Fong et al.³⁴⁾ present the folded distributions at twelve momenta for $\bar{p}p \rightarrow \pi\pi$ and $\bar{p}p \rightarrow kk$, respectively. The dashed curves are Legendre polynomial fits to the data.
4. Tables 4.3 and 4.4 give the fitted values for the Legendre coefficients for $\bar{p}p \rightarrow \pi\pi$ and $\bar{p}p \rightarrow kk$, respectively. The coefficient of P_0 is multiplied by 2π to give the total annihilation cross sections for each reaction.
5. Figure 4.3 presents the total cross section for $\bar{p}p \rightarrow \pi\pi$ and $\bar{p}p \rightarrow kk$ as a function of incident antiproton momentum.
6. Figure 4.4 presents the momentum dependence of the remaining Legendre coefficients for the fits given in Tables 4.3 and 4.4.
7. Tables 4.5 and 4.6 give the differential cross section $d\sigma/d\Omega$ and $d\sigma/du$ at $\cos \theta_{cm} = .99$ (π^- , k^- goes forward) and at $\cos \theta_{cm} = -.99$ (π^+ , k^+ goes forward) for the reactions $\bar{p}p \rightarrow \pi\pi$ and $\bar{p}p \rightarrow kk$ respectively.
8. Figures 4.5 and 4.6 present the differential cross sections

$d\sigma/d\Omega$ at $\cos \theta_{\text{cm}} = \pm .99$ for the $\pi\pi$ annihilations and kk annihilation, respectively. Figures 4.7 and 4.8 present the differential cross sections $d\sigma/du$ at $\cos \theta_{\text{cm}} = \pm .99$ for the $\pi\pi$ annihilations and kk annihilations, respectively.

Figures 4.1 and 4.2 presenting the folded differential cross sections for the two pion and two kaon annihilations show a more striking energy dependence for the two pion annihilation. At the lowest momenta of this reaction there is a fairly simple distribution with peaks at $|\cos \theta_{\text{cm}}| = 0.$ and $1.0.$ At 1.45 GeV/c a second dip begins to appear at $|\cos \theta_{\text{cm}}| \approx .85$ and then up to 2.0 GeV/c there are two very pronounced dips which change with energy. This double-dipped distribution is also seen in the energy averaged data of Chapman et al.³⁵⁾ Finally, at the highest momenta, the peak at $|\cos \theta_{\text{cm}}| = 0.$ rapidly falls away.

The two kaon annihilations also show prominent energy dependent changes, particularly in the vicinity of 1.0 GeV/c. However, the two kaon channel does not develop the double dipped angular distribution observed in the two pion channel.

The dashed curves through the data in Figures 4.1 and 4.2 are Legendre polynomial fits of the form

$$\frac{d\sigma}{d\Omega}(\theta) + \frac{d\sigma}{d\Omega}(\pi - \theta) = \sum_{\ell=0}^L a_{\ell} P_{\ell}(\cos \theta) \quad \ell \text{ even} \quad (4.1)$$

since odd terms cannot contribute to the folded distributions. χ^2 probabilities of all the fits are greater than .002.

Multiplying both sides of Equation (4.1) by 2π and integrating with respect to $d(\cos \theta_{\text{cm}})$ over the interval 0 to 1 produces the equation for the total cross section

$$\sigma = 2\pi a_0. \quad (4.2)$$

This is plotted for both the two pion and two kaon annihilation channels in Figure 4.3. The most striking feature of the energy dependence of these total cross sections is the broad shoulder at 1.0 GeV/c ($s = 4.33$) in the two pion annihilation channel. The over-all energy dependence of the total cross sections are $\sim s^{-6.3}$ and $s^{-4.6}$ for the two pion and the two kaon annihilations, respectively. Other previous measurements appear in Table 4.7.

The most prominent features of the energy dependence of the remaining Legendre coefficients are the behaviors of the a_6 and a_8 coefficients in the regions between 0.8 and 1.8 GeV/c. The peaking of the a_8 coefficient at 1.6 GeV/c combined with the fact that all other coefficients are relatively small at this momentum suggests that a P_4 Legendre polynomial or a combination of P_L^m associated Legendre polynomials simulating a P_4 Legendre polynomial dominates the amplitude at that momentum. Except for the fall and slight fluctuations a_2 , a_4 and a_6 coefficients with increasing momentum at low momenta (.7 - 1.0 GeV/c), the Legendre coefficients of the two kaon annihilation show no interesting structure.

Finally, it can be seen from Figures 4.5 - 4.8 that between .7 and 1.34 GeV/c in both two pion and two kaon annihilations that

the positively charged particle has a higher probability for going forward, contrary to what one might expect from simple charge following considerations. Although there is considerable structure in the cross sections for a charged pion going forward in a two pion annihilation, the cross sections for a charged kaon going forward fall approximately exponentially, the cross section for the k^+ forward having the greater negative slope. The cross section $d\sigma/du$ has an s dependence given by s^{-10} for a positive kaon going forward and by $s^{-5.2}$ for a negative kaon going forward.

Table 4.1 $\bar{p}p$ into $\pi\pi$

Momentum .700 $s = 3.957$

Negative Forward Going Pion

<u>cos θ_{cm}</u>	<u>$d\sigma/d\Omega$</u>	<u>error</u>	<u>-t</u>	<u>-u</u>	<u>$d\sigma/du$</u>	<u>error</u>
.99	156.3	52.1	.43	1.72	1510	504
.96	75.4	29.5	.45	1.70	729	285

Positive Forward Going Pion

<u>cos θ_{cm}</u>	<u>$d\sigma/d\Omega$</u>	<u>error</u>	<u>-t</u>	<u>-u</u>	<u>$d\sigma/du$</u>	<u>error</u>
-.99	123.6	31.9	1.72	.43	1194	308
-.96	153.6	28.4	1.70	.45	1484	274

76

Folded Data

<u>cos θ_{cm}</u>	<u>$d\sigma/d\Omega$</u>	<u>error</u>	<u>-t</u>	<u>-u</u>	<u>$d\sigma/du$</u>	<u>error</u>
.99	279.9	61.1	.43	1.72	2704	590
.96	229.0	40.9	.45	1.70	2212	345
.91	126.5	26.6	.49	1.67	1222	257
.85	134.9	24.4	.53	1.63	1304	236
.77	107.3	17.7	.58	1.58	1037	171
.67	74.0	20.1	.64	1.51	1052	287

Table 4.1 (continued)

Momentum .810 s = 4.086

Negative Forward Going Pion

<u>cos θ</u> _{cm}	<u>dσ/dΩ</u>	<u>error</u>	<u>-t</u>	<u>-u</u>	<u>dσ/du</u>	<u>error</u>
--	--	--------------	-----------	-----------	--------------------------------	--------------

Positive Forward Going Pion

<u>cos θ</u> _{cm}	<u>dσ/dΩ</u>	<u>error</u>	<u>-t</u>	<u>-u</u>	<u>dσ/du</u>	<u>error</u>
-.99	81.8	27.3	1.89	.40	683	228
-.96	101.9	27.1	1.87	.42	851	226

Folded Data*

<u>cos θ</u> _{cm}	<u>dσ/dΩ</u>	<u>error</u>	<u>-t</u>	<u>-u</u>	<u>dσ/du</u>	<u>error</u>
.99	163.6	38.6	.40	1.89	1366	322
.96	203.9	38.3	.42	1.87	1702	320
.91	157.7	27.4	.46	1.83	1316	229
.85	144.3	23.5	.50	1.78	1204	196
.79	68.6	15.8	.55	1.74	573	132
.73	135.1	25.9	.59	1.69	1128	217
.67	73.3	26.3	.64	1.65	612	220

* The first two bins of the folded data are the positive forward going pion data multiplied by 2.

Table 4.1 (continued)

Momentum .870 s = 4.161

Negative Forward Going Pion

<u>cos θ</u> _{cm}	<u>dσ/dΩ</u>	<u>error</u>	<u>-t</u>	<u>-u</u>	<u>dσ/du</u>	<u>error</u>
.99	70.7	12.6	.38	1.98	550	98
.97	100.7	16.1	.40	1.97	783	125
.93	64.5	11.0	.43	1.93	501	86

Positive Forward Going Pion

<u>cos θ</u> _{cm}	<u>dσ/dΩ</u>	<u>error</u>	<u>-t</u>	<u>-u</u>	<u>dσ/du</u>	<u>error</u>
-.99	96.9	15.9	1.98	.38	753	124
-.97	120.3	20.8	1.97	.40	935	162
-.93	86.6	14.4	1.93	.43	673	112

Folded Data

<u>cos θ</u> _{cm}	<u>dσ/dΩ</u>	<u>error</u>	<u>-t</u>	<u>-u</u>	<u>dσ/du</u>	<u>error</u>
.99	167.6	20.3	.38	1.98	1303	158
.97	221.0	26.3	.40	1.97	1718	205
.93	151.0	18.1	.43	1.93	1174	141
.82	117.5	8.1	.52	1.84	913	63
.75	56.0	10.4	.57	1.79	435	81

Table 4.1 (continued)

Momentum .990 s = 4.320

Negative Forward Going Pion

$\cos \theta_{\text{cm}}$	$d\sigma/d\Omega$	error	-t	-u	$d\sigma/du$	error
.99	54.1	6.7	.35	2.17	370	46
.96	70.5	6.6	.38	2.14	481	45
.92	86.5	11.3	.41	2.11	591	77

Positive Forward Going Pion

$\cos \theta_{\text{cm}}$	$d\sigma/d\Omega$	error	-t	-u	$d\sigma/du$	error
-.99	97.9	9.9	2.17	.35	668	67
-.96	94.6	8.3	2.14	.38	646	56
-.92	94.4	12.7	2.11	.41	644	86

Folded Data

$\cos \theta_{\text{cm}}$	$d\sigma/d\Omega$	error	-t	-u	$d\sigma/du$	error
.99	152.0	11.9	.35	2.17	1038	81
.96	165.0	10.6	.38	2.14	1126	72
.92	180.9	16.9	.41	2.11	1235	116
.91	132.7	8.0	.42	2.10	906	55
.85	122.2	6.7	.48	2.04	835	46
.79	97.1	6.3	.53	1.99	663	43
.72	75.8	5.7	.60	1.92	518	39
.65	53.1	7.3	.66	1.86	363	50

Table 4.1 (continued)

Momentum 1.120 s = 4.502

Negative Forward Going Pion

$\cos \theta_{cm}$	$d\sigma/d\Omega$	error	-t	-u	$d\sigma/du$	error
.99	31.5	5.1	.32	2.38	190	31
.96	40.5	3.4	.35	2.35	244	20
.92	34.1	4.4	.39	2.31	206	26

Positive Forward Going Pion

$\cos \theta_{cm}$	$d\sigma/d\Omega$	error	-t	-u	$d\sigma/du$	error
-.99	87.4	15.2	2.38	.32	527	92
-.96	75.2	12.8	2.35	.35	454	78
-.92	59.3	15.0	2.31	.39	358	91

Folded Data

$\cos \theta_{cm}$	$d\sigma/d\Omega$	error	-t	-u	$d\sigma/du$	error
.99	118.9	16.0	.32	2.38	717	97
.96	115.7	13.3	.35	2.35	698	80
.92	93.4	15.6	.39	2.31	564	94
.87	68.5	3.3	.45	2.26	413	20
.80	56.9	2.4	.52	2.18	343	14
.72	42.1	3.2	.60	2.10	254	20
.64	48.1	5.5	.68	2.02	290	33

Table 4.1 (continued)

Momentum 1.340 s = 4.830

Negative Forward Going Pion

$\cos \theta_{cm}$	$d\sigma/d\Omega$	error	-t	-u	$d\sigma/du$	error
.99	31.6	5.5	.28	2.75	159	28
.96	34.7	6.7	.32	2.71	175	34
.92	35.7	6.4	.37	2.66	180	32
.88	45.6	12.2	.42	2.61	220	61

Positive Forward Going Pion

$\cos \theta_{cm}$	$d\sigma/d\Omega$	error	-t	-u	$d\sigma/du$	error
-.99	27.8	3.9	2.75	.28	140	20
-.96	23.2	4.0	2.71	.32	117	20
-.92	20.7	4.1	2.66	.37	104	21
-.88	16.5	5.0	2.61	.42	83	25

Folded Data

$\cos \theta_{cm}$	$d\sigma/d\Omega$	error	-t	-u	$d\sigma/du$	error
.99	59.4	6.7	.28	2.75	299	34
.96	57.9	7.8	.32	2.71	292	39
.92	56.4	7.6	.37	2.66	284	38
.88	62.1	13.2	.42	2.61	313	66
.83	32.0	2.9	.48	2.55	161	15
.77	28.4	3.1	.56	2.48	143	16
.71	33.6	5.3	.63	2.40	169	27

Table 4.1 (continued)

Momentum 1.450 s = 5.001

Negative Forward Going Pion

$\cos \theta_{\text{cm}}$	$d\sigma/d\Omega$	error	-t	-u	$d\sigma/du$	error
.99	34.3	5.1	.26	2.94	160	24
.96	19.8	4.7	.31	2.90	92	22
.92	8.8	3.4	.36	2.84	41	16
.88	7.5	6.6	.41	2.79	35	31

Positive Forward Going Pion

$\cos \theta_{\text{cm}}$	$d\sigma/d\Omega$	error	-t	-u	$d\sigma/du$	error
-.99	25.0	5.0	2.94	.26	116	23
-.96	23.6	5.6	2.90	.31	110	26
-.92	12.3	4.5	2.84	.36	57	21
-.88	26.1	8.0	2.79	.41	122	37

100

Folded Data

$\cos \theta_{\text{cm}}$	$d\sigma/d\Omega$	error	-t	-u	$d\sigma/du$	error
.99	59.3	7.1	.26	2.94	276	33
.96	43.4	7.3	.31	2.90	202	34
.92	21.1	5.6	.36	2.84	98	26
.89	34.5	3.9	.40	2.80	156	48
.88	33.6	10.4	.41	2.79	161	18
.83	29.8	3.1	.48	2.72	139	15
.76	31.0	3.4	.58	2.63	145	16
.68	33.9	4.1	.68	2.52	158	19
.62	20.6	5.5	.76	2.44	96	26

Table 4.1 (continued)

Momentum 1.590 s = 5.225

Negative Forward Going Pion

$\cos \theta_{\text{cm}}$	$d\sigma/d\Omega$	error	-t	-u	$d\sigma/du$	error
.99	19.1	3.8	.25	3.18	81	16
.96	21.3	3.5	.29	3.13	91	15
.92	7.8	2.5	.35	3.08	34	11

Positive Forward Going Pion

$\cos \theta_{\text{cm}}$	$d\sigma/d\Omega$	error	-t	-u	$d\sigma/du$	error
-.99	15.7	3.0	3.18	.25	66	12
-.96	8.2	2.0	3.13	.29	35	9
-.92	4.0	1.6	3.08	.35	17	7

101

Folded Data

$\cos \theta_{\text{cm}}$	$d\sigma/d\Omega$	error	-t	-u	$d\sigma/du$	error
.99	34.8	4.8	.25	3.18	148	20
.96	29.5	4.0	.29	3.13	126	17
.92	11.8	3.0	.35	3.08	50	13
.87	7.3	2.4	.42	3.00	30	11
.81	12.4	2.1	.51	2.91	52	9
.75	21.8	2.9	.60	2.82	92	12
.69	27.7	3.7	.69	2.73	117	15
.63	21.6	4.7	.78	2.65	91	20

Table 4.1 (continued)

Momentum 1.710 s = 5.420

Negative Forward Going Pion

$\cos \theta_{\text{cm}}$	$d\sigma/d\Omega$	<u>error</u>	<u>-t</u>	<u>-u</u>	$d\sigma/du$	<u>error</u>
.99	18.2	4.2	.23	3.39	72	17
.96	15.0	4.7	.28	3.34	59	19
.92	4.2	6.0	.35	3.28	17	24
.88	5.7	4.1	.41	3.21	23	16

Positive Forward Going Pion

$\cos \theta_{\text{cm}}$	$d\sigma/d\Omega$	<u>error</u>	<u>-t</u>	<u>-u</u>	$d\sigma/du$	<u>error</u>
-.99	16.7	3.4	3.39	.23	66	13
-.96	4.2	3.0	3.34	.28	17	12
-.92	9.6	3.8	3.28	.35	38	15
-.88	4.9	2.8	3.21	.41	19	11

Folded Data

$\cos \theta_{\text{cm}}$	$d\sigma/d\Omega$	<u>error</u>	<u>-t</u>	<u>-u</u>	$d\sigma/du$	<u>error</u>
.99	34.9	5.4	.23	3.39	138	21
.96	19.2	5.6	.28	3.34	76	22
.92	13.8	7.1	.35	3.38	54	28
.89	7.2	2.9	.39	3.23	28	11
.88	10.6	4.9	.41	3.21	42	20
.83	8.5	2.9	.49	3.13	34	11
.77	12.9	2.8	.58	3.04	51	11
.71	18.2	3.7	.68	2.94	72	15
.65	18.3	4.3	.78	2.85	72	17

Table 4.1 (continued)

Momentum 1.815 s = 5.594

Negative Forward Going Pion

$\cos \theta_{\text{cm}}$	$d\sigma/d\Omega$	error	-t	-u	$d\sigma/du$	error
.99	17.4	2.5	.23	3.57	65	9
.96	12.3	1.4	.27	3.52	46	5
.92	7.0	1.3	.34	3.45	26	5
.88	4.4	1.9	.41	3.39	16	7
.84	3.1	3.9	.48	3.32	12	14

Positive Forward Going Pion

$\cos \theta_{\text{cm}}$	$d\sigma/d\Omega$	error	-t	-u	$d\sigma/du$	error
-.99	9.1	1.9	3.57	.22	34	7
-.96	6.6	1.0	3.52	.27	25	4
-.92	2.7	1.4	3.45	.34	10	5
-.88	0.0	-	3.39	.41	0	-
-.84	3.5	2.0	3.32	.48	13	7

Folded Data

$\cos \theta_{\text{cm}}$	$d\sigma/d\Omega$	error	-t	-u	$d\sigma/du$	error
.99	26.5	3.1	.22	3.57	98	12
.96	18.9	1.7	.27	3.52	70	6
.92	9.6	1.9	.34	3.45	36	7
.88	4.4	1.9	.41	3.39	16	7
.85	6.5	1.1	.46	3.33	24	4
.84	6.6	4.3	.48	3.32	25	16
.79	11.0	.9	.56	3.23	41	3
.73	14.6	1.2	.66	3.13	54	4
.67	15.3	1.9	.76	3.03	57	7
.62	19.0	3.5	.85	2.95	71	13

Table 4.1 (continued)

Momentum 2.000 s = 5.906

Negative Forward Going Pion

$\cos \theta_{\text{cm}}$	$d\sigma/d\Omega$	error	-t	-u	$d\sigma/du$	error
.99	19.2	3.5	.21	3.90	65	12
.96	10.8	2.6	.26	3.84	36	9
.92	10.0	5.8	.34	3.77	34	20
.88	0.0	-	.41	3.69	0	-
.84	0.0	-	.49	3.62	0	-

Positive Forward Going Pion

$\cos \theta_{\text{cm}}$	$d\sigma/d\Omega$	error	-t	-u	$d\sigma/du$	error
-.99	3.9	1.6	3.90	.21	13	5
-.96	5.4	1.7	3.84	.26	18	6
-.92	3.1	2.7	3.77	.34	11	9
-.88	3.4	2.6	3.69	.41	12	9
-.84	3.1	3.1	3.62	.49	11	11

Folded Data

$\cos \theta_{\text{cm}}$	$d\sigma/d\Omega$	error	-t	-u	$d\sigma/du$	error
.99	23.1	3.8	.21	3.90	78	13
.96	16.2	3.1	.26	3.84	55	10
.92	13.2	6.4	.34	3.77	45	22
.88	3.4	2.6	.41	3.69	12	9
.84	3.1	3.1	.49	3.62	11	11
.83	5.9	2.4	.51	3.60	20	8
.77	8.0	2.1	.62	3.49	27	7
.71	12.0	2.8	.73	3.38	41	9
.65	14.2	3.3	.84	3.26	48	11

Table 4.1 (continued)

Momentum 2.160 s = 6.179

Negative Forward Going Pion

$\cos \theta_{\text{cm}}$	$d\sigma/d\Omega$	error	-t	-u	$d\sigma/du$	error
.99	17.6	2.4	.20	4.18	55	7
.96	15.8	1.5	.26	4.12	49	5
.92	13.9	3.4	.34	4.04	43	11
.88	4.1	1.6	.42	3.96	13	5
.84	0.0	-	.50	3.88	0	-

Positive Forward Going Pion

$\cos \theta_{\text{cm}}$	$d\sigma/d\Omega$	error	-t	-u	$d\sigma/du$	error
-.99	5.4	1.6	4.18	.20	17	5
-.96	6.8	1.8	4.12	.26	21	6
-.92	1.7	1.7	4.04	.34	5	5
-.88	0.0	-	3.96	.42	0	-
-.84	3.4	3.4	3.88	.50	11	11

Folded Data

$\cos \theta_{\text{cm}}$	$d\sigma/d\Omega$	error	-t	-u	$d\sigma/du$	error
.99	23.1	2.8	.20	4.18	72	9
.96	22.6	2.3	.26	4.12	71	7
.92	15.6	3.8	.34	4.04	49	12
.88	4.1	1.6	.42	3.96	13	5
.84	3.4	3.4	.50	3.88	11	11
.80	5.6	.8	.58	3.80	18	3
.72	5.8	1.0	.74	3.64	18	3
.65	5.5	4.8	.88	3.50	17	15

Table 4.1 (continued)

Momentum 2.260 s = 6.352

Negative Forward Going Pion

<u>cos θ_{cm}</u>	<u>dσ/dΩ</u>	<u>error</u>	<u>-t</u>	<u>-u</u>	<u>dσ/du</u>	<u>error</u>
.99	13.3	3.2	.19	4.36	40	10
.96	9.2	2.9	.25	4.30	28	9
.92	16.7	5.9	.34	4.22	50	18

Positive Forward Going Pion

<u>cos θ_{cm}</u>	<u>dσ/dΩ</u>	<u>error</u>	<u>-t</u>	<u>-u</u>	<u>dσ/du</u>	<u>error</u>
-------------------------------------	--	--------------	-----------	-----------	--------------------------------	--------------

106

Folded Data *

<u>cos θ_{cm}</u>	<u>dσ/dΩ</u>	<u>error</u>	<u>-t</u>	<u>-u</u>	<u>dσ/du</u>	<u>error</u>
.99	26.5	4.5	.19	4.36	79	14
.96	18.5	4.1	.25	4.30	55	12
.92	33.4	8.4	.34	4.22	100	25
.89	6.8	3.7	.40	4.15	20	11
.83	9.5	3.6	.53	4.03	28	11
.77	4.3	2.9	.65	3.90	13	9
.71	7.8	2.9	.78	3.77	23	9
.64	11.2	6.0	.93	3.62	33	18

* The first three bins of the folded data are the negative forward going pion data multiplied by 2.

Table 4.1 (continued)

Momentum 2.400, $s = 6.596$

Negative Forward Going Pion

$\cos \theta_{\text{cm}}$	$d\sigma/d\Omega$	error	-t	-u	$d\sigma/du$	error
.99	9.9	2.3	.18	4.61	28	7
.96	3.9	1.5	.25	4.55	11	4
.92	5.0	3.8	.34	4.46	14	11
.88	2.2	2.9	.43	4.37	6	8

Positive Forward Going Pion

$\cos \theta_{\text{cm}}$	$d\sigma/d\Omega$	error	-t	-u	$d\sigma/du$	error
-.99	2.8	1.2	4.61	.18	8	3
-.96	3.4	1.4	4.55	.25	10	4
-.92	6.2	2.6	4.46	.34	18	7
-.88	3.5	3.9	4.37	.43	10	11

Folded Data

$\cos \theta_{\text{cm}}$	$d\sigma/d\Omega$	error	-t	-u	$d\sigma/du$	error
.99	12.6	2.6	.18	4.61	36	7
.96	7.3	2.1	.25	4.55	21	6
.92	11.3	4.6	.34	4.46	32	13
.88	5.8	4.8	.43	4.37	16	14
.83	4.8	2.2	.54	4.26	13	6
.77	5.6	3.2	.67	4.12	16	9
.71	10.7	4.5	.81	3.99	30	13

Table 4.2 $\bar{p}p$ into kk

Momentum .700 s = 3.957

Negative Forward Going Kaon

$\cos \theta_{cm}$	$d\sigma/d\Omega$	error	-t	-u	$d\sigma/du$	error
.99	10.9	10.9	.29	1.42	120	120
.97	32.3	27.6	.30	1.41	356	304

Positive Forward Going Kaon

$\cos \theta_{cm}$	$d\sigma/d\Omega$	error	-t	-u	$d\sigma/du$	error
-.99	63.0	23.1	1.42	.29	695	254
-.97	50.2	27.6	1.41	.30	554	304

Folded Data

$\cos \theta_{cm}$	$d\sigma/d\Omega$	error	-t	-u	$d\sigma/du$	error
.99	73.9	25.5	.29	1.42	815	282
.97	82.5	39.0	.30	1.41	908	431
.90	121.9	28.6	.34	1.37	1343	315
.85	68.3	16.6	.37	1.34	752	182
.79	58.3	15.7	.40	1.31	644	174
.72	20.5	8.8	.44	1.27	226	97
.64	44.4	25.8	.49	1.22	489	284

Table 4.2 (continued)

Momentum .810 s = 4.086

Negative Forward Going Kaon

$\cos \theta_{\text{cm}}$	$d\sigma/d\Omega$	<u>error</u>	<u>-t</u>	<u>-u</u>	$d\sigma/du$	<u>error</u>
---------------------------	-------------------	--------------	-----------	-----------	--------------	--------------

Positive Forward Going Kaon

$\cos \theta_{\text{cm}}$	$d\sigma/d\Omega$	<u>error</u>	<u>-t</u>	<u>-u</u>	$d\sigma/du$	<u>error</u>
-.99	30.1	22.5	1.58	.26	286	213
-.96	33.9	17.9	1.56	.28	321	170

109

Folded Data*

$\cos \theta_{\text{cm}}$	$d\sigma/d\Omega$	<u>error</u>	<u>-t</u>	<u>-u</u>	$d\sigma/du$	<u>error</u>
.99	60.3	31.8	.26	1.58	571	301
.96	67.8	25.3	.28	1.56	642	240
.91	45.3	14.9	.32	1.52	429	141
.85	79.8	28.2	.36	1.48	756	267
.79	51.4	21.0	.40	1.44	487	199
.73	71.6	22.9	.43	1.40	678	217
.67	42.7	17.5	.47	1.36	404	166

* The first two bins of the folded data are the positive forward going kaon data multiplied by 2.

Table 4.2 (continued)

Momentum .870 s = 4.161

Negative Forward Going Kaon

<u>cos θ_{cm}</u>	<u>dσ/dΩ</u>	<u>error</u>	<u>-t</u>	<u>-u</u>	<u>dσ/du</u>	<u>error</u>
.99	19.5	7.7	.25	1.66	172	68
.94	17.1	5.0	.29	1.63	151	44

Positive Forward Going Kaon

<u>cos θ_{cm}</u>	<u>dσ/dΩ</u>	<u>error</u>	<u>-t</u>	<u>-u</u>	<u>dσ/du</u>	<u>error</u>
-.99	16.3	10.8	1.66	.25	143	95
-.94	11.0	4.5	1.63	.29	97	39

110

Folded Data

<u>cos θ_{cm}</u>	<u>dσ/dΩ</u>	<u>error</u>	<u>-t</u>	<u>-u</u>	<u>dσ/du</u>	<u>error</u>
.99	35.8	13.3	.25	1.66	315	117
.94	28.2	6.7	.29	1.63	248	59
.91	18.5	6.1	.31	1.61	163	54
.85	32.1	5.1	.35	1.56	282	45
.79	29.5	7.4	.39	1.52	260	65
.73	22.3	8.6	.44	1.48	197	75

Table 4.2 (continued)

Momentum .990 s = 4.320

Negative Forward Going Kaon

$\cos \theta_{\text{cm}}$	$d\sigma/d\Omega$	error	-t	-u	$d\sigma/du$	error
.99	14.6	4.4	.23	1.84	112	34
.97	18.6	6.6	.24	1.83	143	51
.92	17.4	3.9	.28	1.79	134	30

Positive Forward Going Kaon

$\cos \theta_{\text{cm}}$	$d\sigma/d\Omega$	error	-t	-u	$d\sigma/du$	error
-.99	33.9	6.6	1.84	.23	261	51
-.97	26.4	7.7	1.83	.24	203	60
-.92	21.1	4.9	1.79	.28	162	38

111

Folded Data

$\cos \theta_{\text{cm}}$	$d\sigma/d\Omega$	error	-t	-u	$d\sigma/du$	error
.99	48.5	8.0	.23	1.84	373	61
.97	45.1	10.2	.24	1.83	347	78
.92	38.5	6.2	.28	1.79	296	48
.91	25.1	4.3	.29	1.78	193	33
.85	22.9	3.6	.34	1.73	176	28
.79	23.8	4.2	.39	1.68	183	32
.73	13.5	4.4	.44	1.53	104	34
.67	17.6	4.7	.49	1.58	135	36
.62	21.2	6.9	.53	1.54	163	53

Table 4.2 (continued)

Momentum 1.120 s = 4.502

Negative Forward Going Kaon

$\cos \theta_{\text{cm}}$	$d\sigma/d\Omega$	<u>error</u>	<u>-t</u>	<u>-u</u>	$d\sigma/du$	<u>error</u>
.99	12.0	3.7	.21	2.05	81	25
.96	16.6	3.3	.23	2.02	112	23
.92	13.5	3.6	.27	1.98	92	24

Positive Forward Going Kaon

$\cos \theta_{\text{cm}}$	$d\sigma/d\Omega$	<u>error</u>	<u>-t</u>	<u>-u</u>	$d\sigma/du$	<u>error</u>
-.99	23.6	11.0	2.05	.21	159	75
-.96	22.9	12.0	2.02	.23	155	81
-.92	20.9	12.0	1.98	.27	141	81

112

Folded Data

$\cos \theta_{\text{cm}}$	$d\sigma/d\Omega$	<u>error</u>	<u>-t</u>	<u>-u</u>	$d\sigma/du$	<u>error</u>
.99	35.6	11.6	.21	2.05	240	79
.96	39.5	12.4	.23	2.02	267	84
.92	34.4	12.6	.27	1.98	232	85
.91	16.5	2.8	.28	1.97	111	19
.85	10.1	1.4	.34	1.92	68	9
.79	11.1	1.9	.39	1.86	75	13
.73	9.3	2.2	.45	1.81	63	15

Table 4.2 (continued)

Momentum 1.340 s = 4.830

Negative Forward Going Kaon

$\cos \theta_{cm}$	$d\sigma/d\Omega$	error	-t	-u	$d\sigma/du$	error
.99	7.1	3.3	.18	2.40	40	19
.95	5.0	3.9	.32	2.36	28	22

Positive Forward Going Kaon

$\cos \theta_{cm}$	$d\sigma/d\Omega$	error	-t	-u	$d\sigma/du$	error
-.99	13.5	3.8	2.40	.18	76	21
-.95	6.3	2.1	2.36	.22	35	12

Folded Data

$\cos \theta_{cm}$	$d\sigma/d\Omega$	error	-t	-u	$d\sigma/du$	error
.99	20.6	5.1	.18	2.40	115	28
.95	11.4	4.5	.22	2.36	64	25
.87	7.9	2.5	.31	2.27	44	14
.81	4.7	1.7	.38	2.20	26	10
.75	8.2	3.0	.45	2.13	46	17
.69	9.8	3.8	.52	2.07	55	22

Table 4.2 (continued)

Momentum 1.450 s = 5.001

Negative Forward Going Kaon

$\cos \theta_{\text{cm}}$	$d\sigma/d\Omega$	<u>error</u>	<u>-t</u>	<u>-u</u>	$d\sigma/du$	<u>error</u>
.99	12.7	5.5	.17	2.58	66	21
.95	9.7	3.2	.22	2.54	50	17

Positive Forward Going Kaon

$\cos \theta_{\text{cm}}$	$d\sigma/d\Omega$	<u>error</u>	<u>-t</u>	<u>-u</u>	$d\sigma/du$	<u>error</u>
-.99	4.1	2.9	2.58	.17	21	15
-.95	5.5	2.4	2.54	.22	28	13

114

Folded Data

$\cos \theta_{\text{cm}}$	$d\sigma/d\Omega$	<u>error</u>	<u>-t</u>	<u>-u</u>	$d\sigma/du$	<u>error</u>
.99	16.8	6.2	.17	2.58	87	32
.95	15.2	4.0	.22	2.54	78	21
.89	16.0	3.1	.29	2.46	83	16
.83	7.7	2.8	.36	2.39	40	15
.77	9.9	3.1	.44	2.32	51	16
.71	12.0	3.6	.51	2.24	62	18
.65	9.1	3.5	.58	2.17	47	18

Table 4.2 (continued)

Momentum 1.590 s = 5.225

Negative Forward Going Kaon

$\cos \theta_{\text{cm}}$	$d\sigma/d\Omega$	<u>error</u>	<u>-t</u>	<u>-u</u>	$d\sigma/du$	<u>error</u>
.99	12.0	3.2	.16	2.82	56	15
.94	9.1	1.8	.22	2.75	43	9

Positive Forward Going Kaon

$\cos \theta_{\text{cm}}$	$d\sigma/d\Omega$	<u>error</u>	<u>-t</u>	<u>-u</u>	$d\sigma/du$	<u>error</u>
-.99	4.0	2.0	2.82	.16	19	9
-.94	2.4	1.2	2.75	.22	11	5

115

Folded Data

$\cos \theta_{\text{cm}}$	$d\sigma/d\Omega$	<u>error</u>	<u>-t</u>	<u>-u</u>	$d\sigma/du$	<u>error</u>
.99	15.6	3.7	.16	2.82	75	18
.94	11.5	2.2	.22	2.75	54	10
.88	13.3	3.4	.30	2.67	62	16
.80	7.3	1.7	.41	2.56	34	10
.73	7.4	2.1	.51	2.47	34	10
.65	11.9	3.0	.61	2.36	56	14

Table 4.2 (continued)

Momentum 1.710 s = 5.420

Negative Forward Going Kaon

$\cos \theta_{cm}$	$d\sigma/d\Omega$	<u>error</u>	<u>-t</u>	<u>-u</u>	$d\sigma/du$	<u>error</u>
.99	7.7	3.7	.15	3.02	33	16
.95	9.4	3.3	.21	2.97	41	14

Positive Forward Going Kaon

$\cos \theta_{cm}$	$d\sigma/d\Omega$	<u>error</u>	<u>-t</u>	<u>-u</u>	$d\sigma/du$	<u>error</u>
-.99	0.0	-	3.02	.15	0	-
-.95	1.5	3.3	2.97	.21	6	14

Folded Data

$\cos \theta_{cm}$	$d\sigma/d\Omega$	<u>error</u>	<u>-t</u>	<u>-u</u>	$d\sigma/du$	<u>error</u>
.99	7.7	3.7	.15	3.02	33	16
.95	10.9	4.7	.21	2.97	47	20
.89	14.7	4.0	.29	2.88	64	18
.83	11.6	2.8	.38	2.79	50	12
.77	7.8	3.1	.47	2.70	34	14
.71	10.6	3.8	.55	2.62	46	17
.65	10.5	3.3	.64	2.53	45	14

Table 4.2 (continued)

Momentum 1.815 s = 5.594

Negative Forward Going Kaon

<u>cos θ</u> _{cm}	<u>dσ/dΩ</u>	<u>error</u>	<u>-t</u>	<u>-u</u>	<u>dσ/du</u>	<u>error</u>
.99	8.8	2.0	.14	3.20	36	8
.96	9.9	1.4	.19	3.16	40	6
.94	8.1	.8	.22	3.13	33	3

Positive Forward Going Kaon

<u>cos θ</u> _{cm}	<u>dσ/dΩ</u>	<u>error</u>	<u>-t</u>	<u>-u</u>	<u>dσ/du</u>	<u>error</u>
-.99	1.2	.9	3.20	.14	5	4
-.96	1.0	.6	3.16	.19	4	3
-.94	1.8	.7	3.13	.22	7	3

117

Folded Data

<u>cos θ</u> _{cm}	<u>dσ/dΩ</u>	<u>error</u>	<u>-t</u>	<u>-u</u>	<u>dσ/du</u>	<u>error</u>
.99	10.0	2.2	.14	3.20	41	9
.96	10.9	1.5	.19	3.16	44	6
.94	9.9	1.0	.22	3.13	40	4
.87	10.1	.7	.33	3.02	41	3
.77	8.1	.6	.48	2.86	33	2
.67	7.5	.9	.64	2.71	30	4

Table 4.2 (continued)

Momentum 2.000 s = 5.906

Negative Forward Going Kaon

$\cos \theta_{\text{cm}}$	$d\sigma/d\Omega$	<u>error</u>	<u>-t</u>	<u>-u</u>	$d\sigma/du$	<u>error</u>
.99	10.2	2.9	.13	3.53	37	11
.96	2.6	1.7	.18	3.47	10	6
.92	6.5	5.6	.25	3.41	24	21
.88	6.7	8.1	.32	3.34	25	30

Positive Forward Going Kaon

$\cos \theta_{\text{cm}}$	$d\sigma/d\Omega$	<u>error</u>	<u>-t</u>	<u>-u</u>	$d\sigma/du$	<u>error</u>
-.99	.6	1.0	3.53	.13	2	4
-.96	2.0	1.0	3.47	.18	7	4
-.92	0.0	-	3.41	.25	0	-
-.88	0.0	-	3.34	.32	0	-

118

Folded Data

$\cos \theta_{\text{cm}}$	$d\sigma/d\Omega$	<u>error</u>	<u>-t</u>	<u>-u</u>	$d\sigma/du$	<u>error</u>
.99	10.8	3.1	.13	3.53	40	11
.96	4.6	2.0	.18	3.47	17	7
.92	6.5	5.6	.25	3.41	24	21
.88	6.7	8.1	.32	3.34	25	30
.85	4.9	2.2	.37	3.29	18	8
.75	9.0	2.0	.54	3.11	33	8
.66	7.1	2.6	.70	2.96	26	9

Table 4.2 (continued)

Momentum 2.160 s = 6.179

Negative Forward Going Kaon

$\cos \theta_{\text{cm}}$	$d\sigma/d\Omega$	error	-t	-u	$d\sigma/du$	error
.99	7.4	1.9	.12	3.81	25	6
.95	7.5	1.1	.20	3.73	25	4
.89	6.1	1.6	.31	3.62	21	6

Positive Forward Going Kaon

$\cos \theta_{\text{cm}}$	$d\sigma/d\Omega$	error	-t	-u	$d\sigma/du$	error
-.99	1.1	1.1	3.81	.12	4	4
-.95	0.0	-	3.73	.20	0	-
-.89	0.0	-	3.62	.31	0	-

119

Folded Data

$\cos \theta_{\text{cm}}$	$d\sigma/d\Omega$	error	-t	-u	$d\sigma/du$	error
.99	8.4	2.1	.12	3.81	29	7
.95	7.5	1.1	.20	3.73	25	4
.89	6.1	1.6	.31	3.62	21	6
.85	7.3	1.1	.38	3.55	25	4
.75	6.8	.8	.57	3.36	23	3

Table 4.2 (continued)

Momentum 2.260 s = 6.352

Negative Forward Going Kaon

<u>cos θ_{cm}</u>	<u>dσ/dΩ</u>	<u>error</u>	<u>-t</u>	<u>-u</u>	<u>dσ/du</u>	<u>error</u>
.99	4.9	2.6	.12	3.98	16	8
.96	5.5	2.0	.18	3.92	18	7
.92	2.4	2.4	.26	3.85	8	8

Positive Forward Going Kaon

<u>cos θ_{cm}</u>	<u>dσ/dΩ</u>	<u>error</u>	<u>-t</u>	<u>-u</u>	<u>dσ/du</u>	<u>error</u>
-------------------------------------	--	--------------	-----------	-----------	--------------------------------	--------------

120

Folded Data *

<u>cos θ_{cm}</u>	<u>dσ/dΩ</u>	<u>error</u>	<u>-t</u>	<u>-u</u>	<u>dσ/du</u>	<u>error</u>
.99	9.8	3.7	.12	3.98	32	12
.96	10.9	2.8	.18	3.92	35	9
.92	4.8	3.4	.26	3.85	16	11
.87	5.6	2.4	.35	3.75	18	8
.81	5.3	4.6	.47	3.63	17	15
.75	10.7	4.2	.59	3.52	35	14
.69	12.8	9.0	.71	3.40	41	29
.63	8.4	4.2	.82	3.28	27	14

* The first three bins of the folded data are the negative forward going kaon data multiplied by 2.

Table 4.2 (continued)

Momentum 2.400 s = 6.596

Negative Forward Going Kaon

<u>cos θ_{cm}</u>	<u>dσ/dΩ</u>	<u>error</u>	<u>-t</u>	<u>-u</u>	<u>dσ/du</u>	<u>error</u>
.99	6.5	2.1	.12	4.23	20	6
.96	4.2	1.5	.18	4.17	13	5
.92	3.2	3.9	.26	4.09	10	12
.89	10.3	10.3	.32	4.02	25	8

Positive Forward Going Kaon

<u>cos θ_{cm}</u>	<u>dσ/dΩ</u>	<u>error</u>	<u>-t</u>	<u>-u</u>	<u>dσ/du</u>	<u>error</u>
-.99	0.0	-	4.23	.12	0	-
-.96	.7	.7	4.17	.18	2	2
-.92	2.0	2.0	4.09	.26	6	6
-.89	2.1	1.6	4.02	.32	7	5

121

Folded Data

<u>cos θ_{cm}</u>	<u>dσ/dΩ</u>	<u>error</u>	<u>-t</u>	<u>-u</u>	<u>dσ/du</u>	<u>error</u>
.99	6.5	2.1	.12	4.23	20	6
.96	4.9	1.7	.18	4.17	15	5
.92	5.2	4.4	.26	4.09	16	13
.89	10.5	3.2	.32	4.02	32	10
.81	5.8	2.7	.49	3.86	18	8

Figure 4.1: Folded pion cross sections with Legendre fit (solid curve)

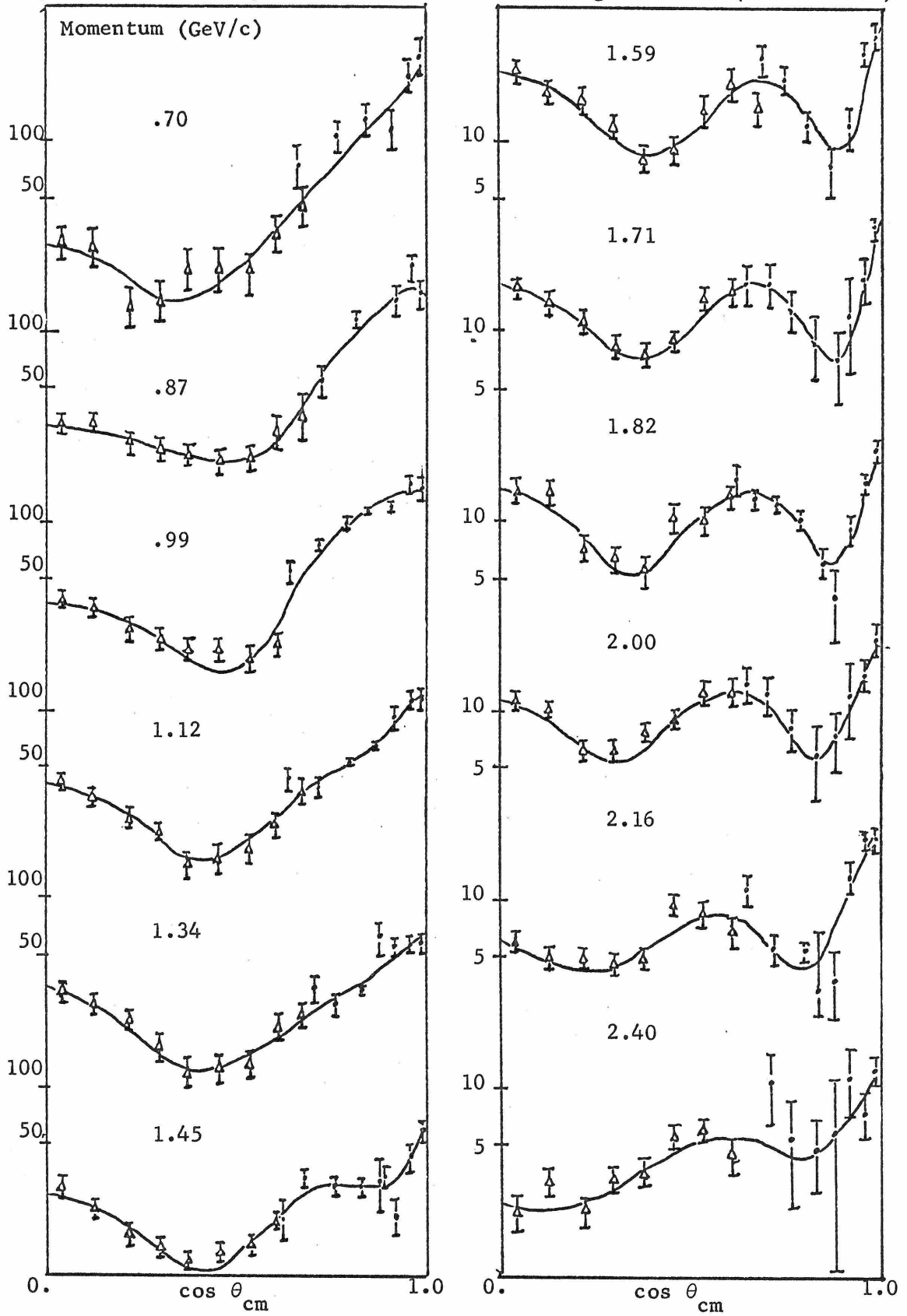


Figure 4.2: Folded kaon cross sections with Legendre fit (solid curve)

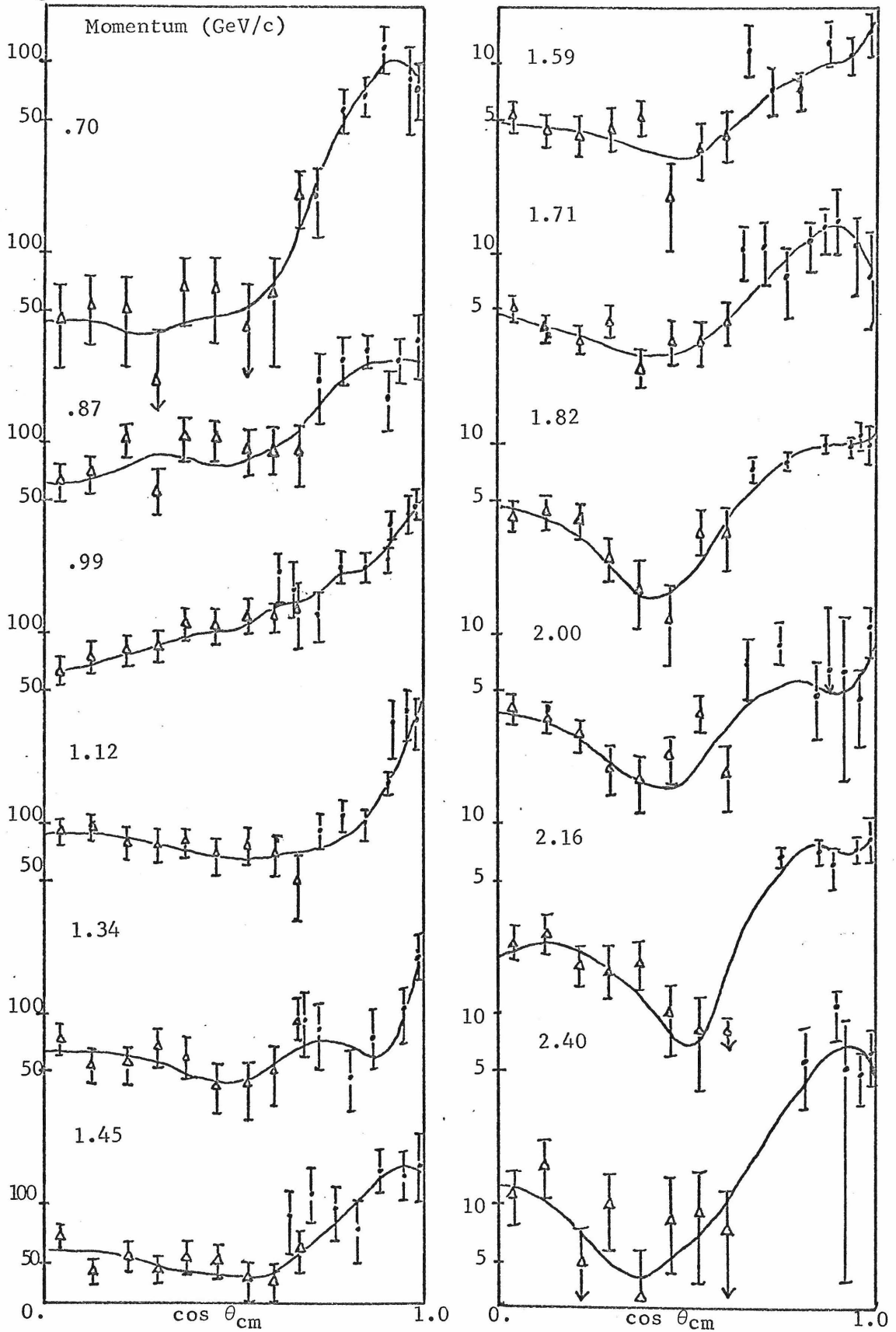


Table 4.3



Legendre Expansion Coefficients

Momentum	$\frac{\sigma_{\text{total}}}{2\pi a_0}$	a_2	a_4	a_6	a_8	a_{10}	χ^2	Prob.
.700	358.4 ±22.5	123.0 ±12.6	76.1 ±16.0				15.6	.08
.870	352.6 ±12.5	103.6 ± 6.6	65.8 ± 7.3	-24.6 ± 8.1	-26.8 ±10.6	-9.7 ± 8.9	8.6	.38
.990	342.1 ± 7.1	90.1 ± 3.3	50.4 ± 4.2	-35.8 ± 4.8	- 9.8 ± 5.6	5.4 ± 5.3	25.7	.002
1.120	243.6 ± 6.0	44.7 ± 3.4	41.7 ± 4.6	- 7.7 ± 4.6	17.3 ± 4.6	.4 ± 4.4	11.3	.33
1.340	163.6 ± 4.9	20.0 ± 2.3	23.6 ± 2.8	-10.4 ± 2.9	9.3 ± 3.9	- 5.5 ± 4.0	9.7	.46
1.450	145.0 ± 3.9	15.4 ± 1.8	13.1 ± 2.5	- 7.5 ± 2.7	17.4 ± 3.0	2.5 ± 3.0	20.4	.04
1.590	98.5 ± 3.3	2.4 ± 1.3	7.3 ± 1.8	.9 ± 2.0	22.3 ± 2.4	.8 ± 2.6	20.7	.04
1.710	82.8 ± 3.3	2.9 ± 1.5	4.3 ± 2.1	3.6 ± 2.2	19.8 ± 2.5	-1.7 ± 2.5	4.0	.95
1.815	66.7 ± 2.0	2.5 ± .7	2.4 ± 1.0	2.2 ± 1.1	15.7 ± 1.4	-3.6 ± 1.5	14.3	.22
2.000	59.7 ± 2.5	3.3 ± 1.1	2.1 ± 1.4	5.7 ± 1.6	9.1 ± 2.0	-5.4 ± 1.9	5.9	.82
2.160	43.1 ± 1.6	5.4 ± .7	4.7 ± .9	7.5 ± 1.0	4.5 ± 1.3	-3.2 ± 1.2	22.7	.01
2.400	28.0 ± 2.5	3.7 ± 1.1	.4 ± 1.2	3.1 ± 1.5	1.3 ± 1.9	-1.0 ± 1.7	10.4	.32

$$\frac{d\sigma}{d\Omega} = \sum_{\ell=0}^L a_{\ell} P_{\ell}(\cos \theta), \ell \text{ even}$$

There are ~ 15 data points/momentum

Table 4.4

 $\bar{p}p \rightarrow kk$

Legendre Expansion Coefficients

Momentum	$\frac{\sigma_{\text{total}}}{2\pi a_0}$	a_2	a_4	a_6	a_8	a_{10}	χ^2	Prob.
.700	158.2 ± 17.2	68.4 ± 9.4	32.4 ± 9.1	-24.0 ± 10.4	-34.1 ± 12.0	-15.1 ± 8.7	6.7	.75
.870	81.5 ± 5.9	16.6 ± 2.9	4.1 ± 4.0	-4.9 ± 5.0	-3.8 ± 4.9	2.9 ± 4.4	14.7	.10
.990	92.4 ± 4.3	20.1 ± 2.0	9.2 ± 2.7	5.7 ± 3.1	2.0 ± 3.3	1.9 ± 3.2	7.2	.84
1.120	63.0 ± 3.9	9.5 ± 2.2	13.0 ± 3.2	6.9 ± 3.3	4.6 ± 3.1	1.9 ± 2.8	7.4	.69
1.340	40.4 ± 3.1	3.5 ± 1.5	4.8 ± 1.9	2.6 ± 2.0	5.0 ± 2.5	3.5 ± 2.6	7.6	.58
1.450	44.4 ± 2.9	7.1 ± 1.5	5.6 ± 1.9	-1.7 ± 2.3	-2.1 ± 2.3	-1.1 ± 2.0	13.4	.20
1.590	37.3 ± 2.6	6.0 ± 1.1	3.9 ± 1.4	-1.4 ± 1.7	1.2 ± 2.1	1.6 ± 1.9	11.0	.20
1.710	38.2 ± 3.0	6.9 ± 1.4	1.3 ± 1.7	-5.8 ± 1.8	-2.0 ± 2.2	-.5 ± 2.1	8.3	.60
1.815	32.3 ± 1.3	5.9 $\pm .5$	2.0 $\pm .7$	-4.2 $\pm .8$	1.8 ± 1.0	.4 ± 1.0	8.1	.42
2.000	23.0 ± 2.3	2.7 ± 1.0	1.5 ± 1.1	-1.8 ± 1.5	2.6 ± 1.8	1.1 ± 1.5	13.2	.16
2.160	21.1 ± 1.2	4.8 $\pm .5$	2.1 $\pm .7$	-3.2 $\pm .9$	-.1 ± 1.0	2.3 $\pm .9$	10.4	.17
2.400	13.2 ± 2.5	4.2 ± 1.0	2.0 ± 1.0	-2.0 ± 1.5	-1.3 ± 1.4	-.8 ± 1.3	9.4	.23

$$\frac{d\sigma}{d\Omega} = \sum_{l=0}^L a_l P_l(\cos \theta), \quad l \text{ even}$$

There are ~ 15 data points/momentum

Figure 4.3: Pion and kaon total cross sections

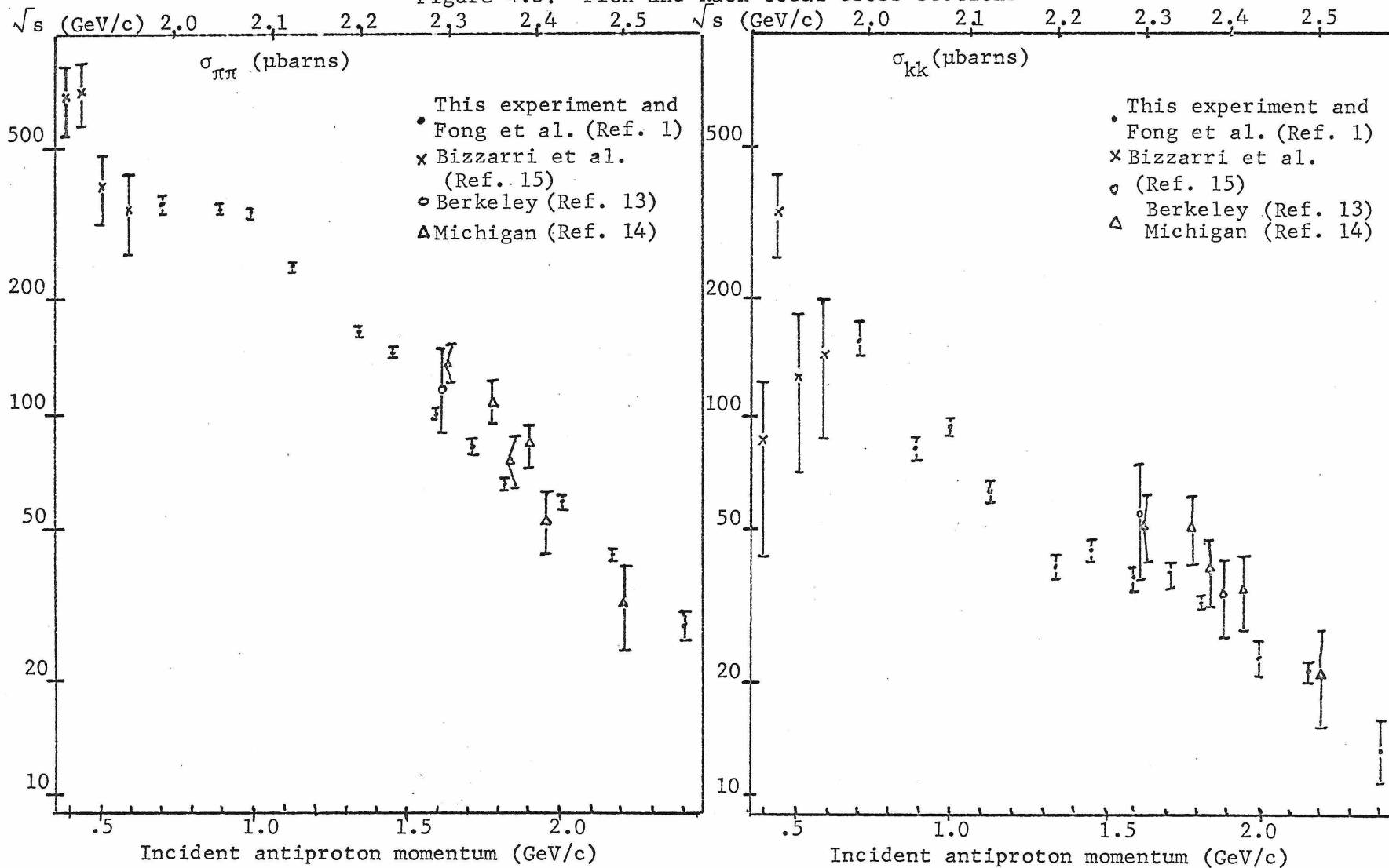


Figure 4.4: Pion and kaon Legendre expansion coefficients

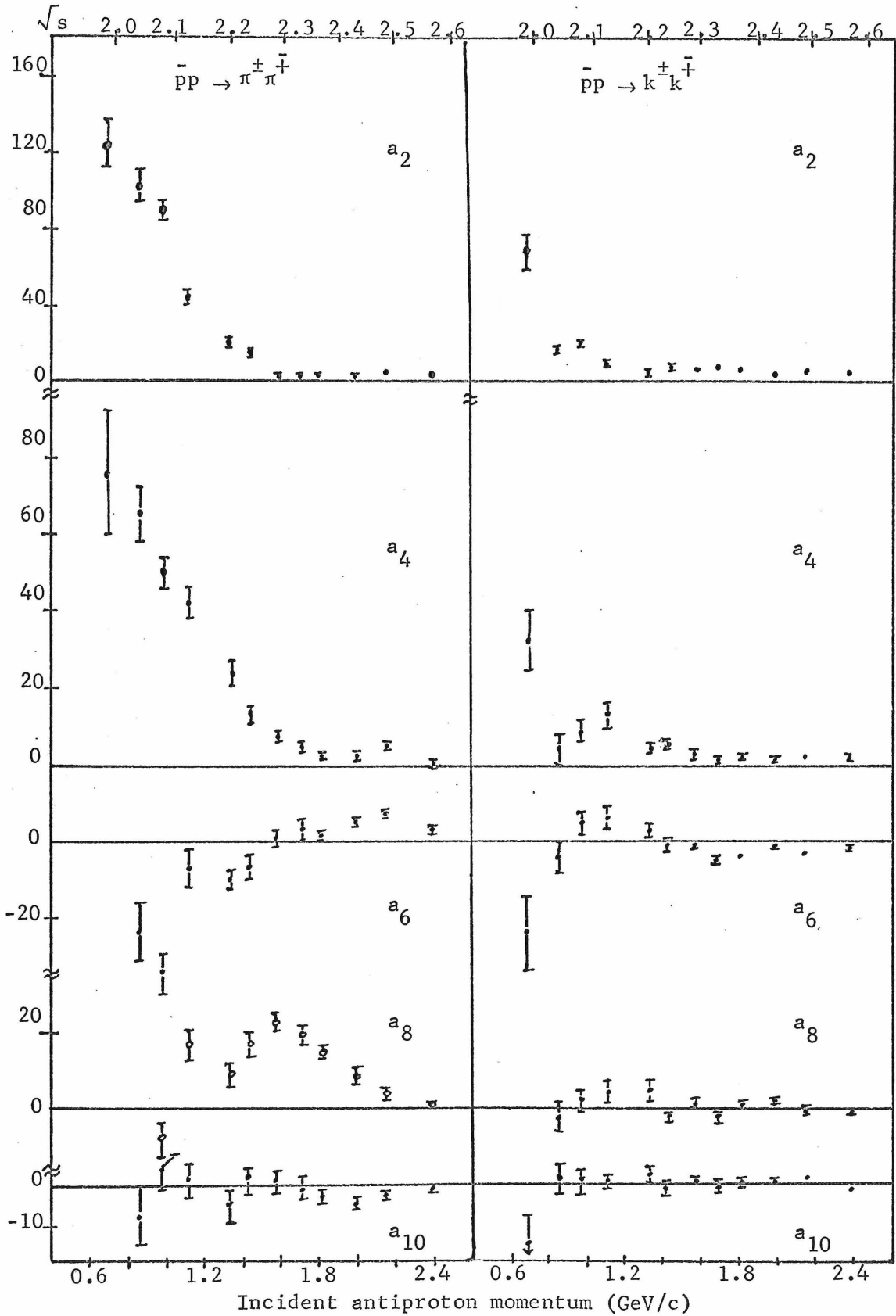


Table 4.5: Pion Extreme Angle Differential Cross Sections

2 π Annihilations

<u>Forward $\pi^- \cos \theta = .99$</u>					<u>Forward $\pi^+ \cos \theta = - .99$</u>				
<u>p</u>	<u>s</u>	<u>t</u>	<u>u</u>	<u>dσ/dΩ</u>	<u>dσ/du</u>	<u>t</u>	<u>u</u>	<u>dσ/dΩ</u>	<u>dσ/du</u>
.700	3.957	-.43	-1.72	156.3 \pm 52.1	1510 \pm 504	-1.72	-.43	123.6 \pm 31.9	1194 \pm 308
.870	4.161	-.38	-1.98	70.7 \pm 12.6	550 \pm 98	-1.98	-.38	96.9 \pm 15.9	753 \pm 124
.990	4.320	-.35	-2.17	54.1 \pm 6.7	370 \pm 46	-2.17	-.35	97.9 \pm 9.9	668 \pm 67
1.120	4.502	-.32	-2.38	31.5 \pm 5.1	190 \pm 31	-2.38	-.32	87.4 \pm 15.2	527 \pm 92
1.340	4.830	-.28	-2.75	31.6 \pm 5.5	159 \pm 28	-2.75	-.28	27.8 \pm 3.9	140 \pm 20
1.450	5.001	-.26	-2.94	34.3 \pm 5.1	160 \pm 24	-2.94	-.26	25.0 \pm 5.0	116 \pm 23
1.590	5.225	-.25	-3.18	19.1 \pm 3.8	81 \pm 16	-3.18	-.25	15.7 \pm 3.0	66 \pm 12
1.710	5.420	-.23	-3.39	18.2 \pm 4.2	72 \pm 17	-3.39	-.23	16.7 \pm 3.4	66 \pm 13
1.815	5.594	-.22	-3.57	17.4 \pm 2.5	65 \pm 9	-3.57	-.22	9.1 \pm 1.9	34 \pm 7
2.000	5.906	-.21	-3.90	19.2 \pm 3.5	65 \pm 12	-3.90	-.21	3.9 \pm 1.6	13 \pm 5
2.160	6.179	-.20	-4.18	17.6 \pm 2.4	55 \pm 7	-4.18	-.20	5.4 \pm 1.6	17 \pm 5
2.400	6.596	-.18	-4.61	9.9 \pm 2.3	28 \pm 7	-4.61	-.18	2.8 \pm 1.2	8 \pm 3

Table 4.6: Kaon Extreme Angle Differential Cross Sections

2k Annihilations

<u>Forward $k^- \cos \theta = .99$</u>						<u>Forward $k^+ \cos \theta = - .99$</u>			
<u>p</u>	<u>s</u>	<u>t</u>	<u>u</u>	<u>$d\sigma/d\Omega$</u>	<u>$d\sigma/du$</u>	<u>t</u>	<u>u</u>	<u>$d\sigma/d\Omega$</u>	<u>$d\sigma/du$</u>
.700	3.957	-.29	-.42	10.9 ± 10.9	120 ± 120	-1.42	-.29	63.0 ± 23.1	695 ± 254
.870	4.161	-.25	-1.66	19.5 ± 7.7	172 ± 68	-1.66	-.25	16.3 ± 10.8	143 ± 95
.990	4.320	-.23	-1.84	14.6 ± 4.4	112 ± 34	-1.84	-.23	33.9 ± 6.6	261 ± 51
1.120	4.502	-.21	-2.05	12.0 ± 3.7	81 ± 25	-2.05	-.21	23.6 ± 11.0	159 ± 75
1.340	4.830	-.18	-2.40	7.1 ± 3.3	40 ± 19	-2.40	-.18	13.5 ± 3.8	76 ± 21
1.450	5.001	-.17	-2.58	12.7 ± 5.5	66 ± 28	-2.58	-.17	4.1 ± 2.9	21 ± 15
1.590	5.225	-.16	-2.82	12.0 ± 3.2	56 ± 15	-2.82	-.16	4.0 ± 2.0	19 ± 9
1.710	5.420	-.15	-3.02	7.7 ± 3.7	33 ± 16	-3.02	-.15	0.0	0 -
1.815	5.594	-.14	-3.20	8.8 ± 2.0	36 ± 8	-3.20	-.14	$1.2 \pm .9$	5 ± 4
2.000	5.906	-.13	-3.53	10.2 ± 2.9	37 ± 11	-3.53	-.13	$.6 \pm 1.0$	2 ± 4
2.160	6.179	-.12	-3.81	7.4 ± 1.9	25 ± 6	-3.81	-.12	1.1 ± 1.1	4 ± 4
2.400	6.596	-.12	-4.23	6.5 ± 2.1	20 ± 6	-4.23	-.12	0.0	0 -

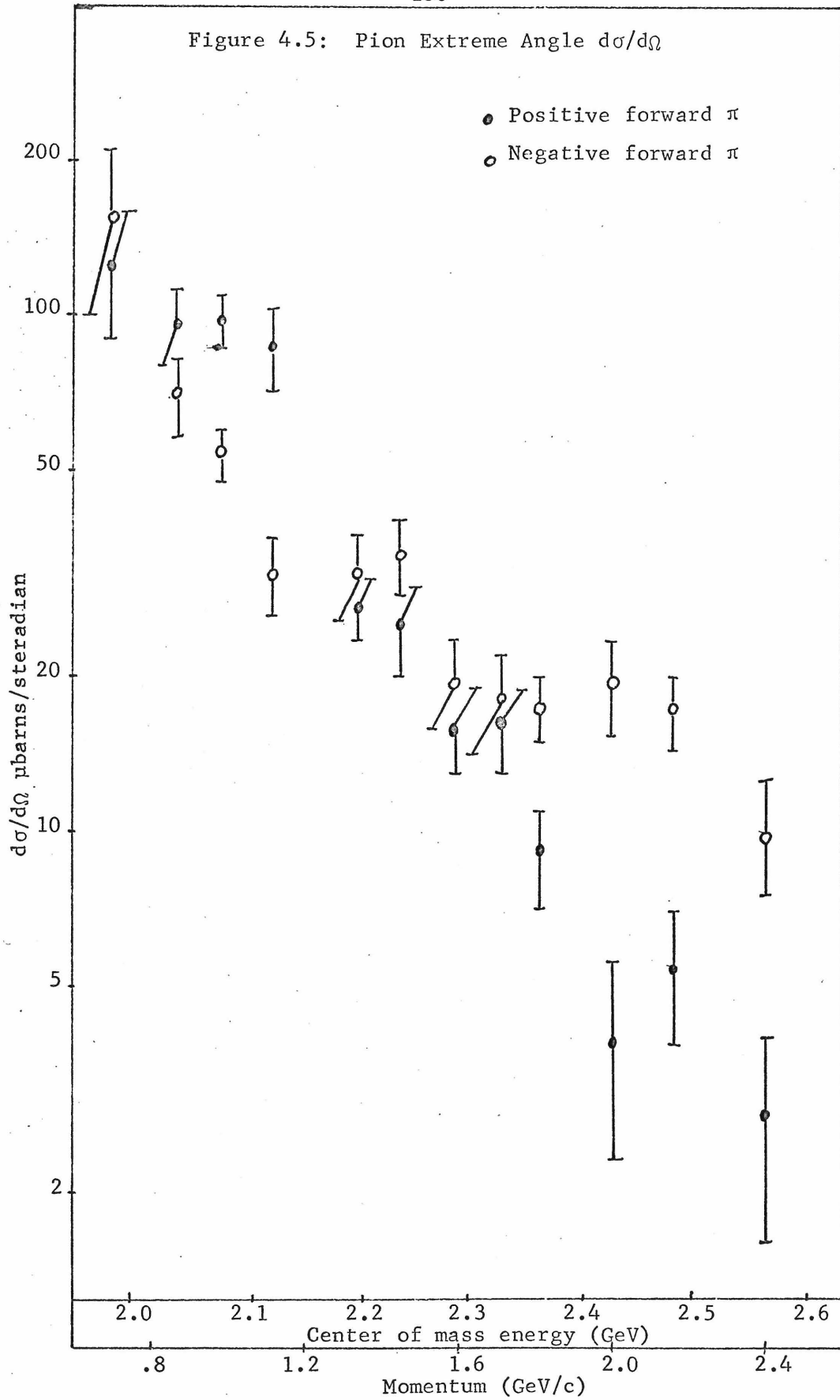
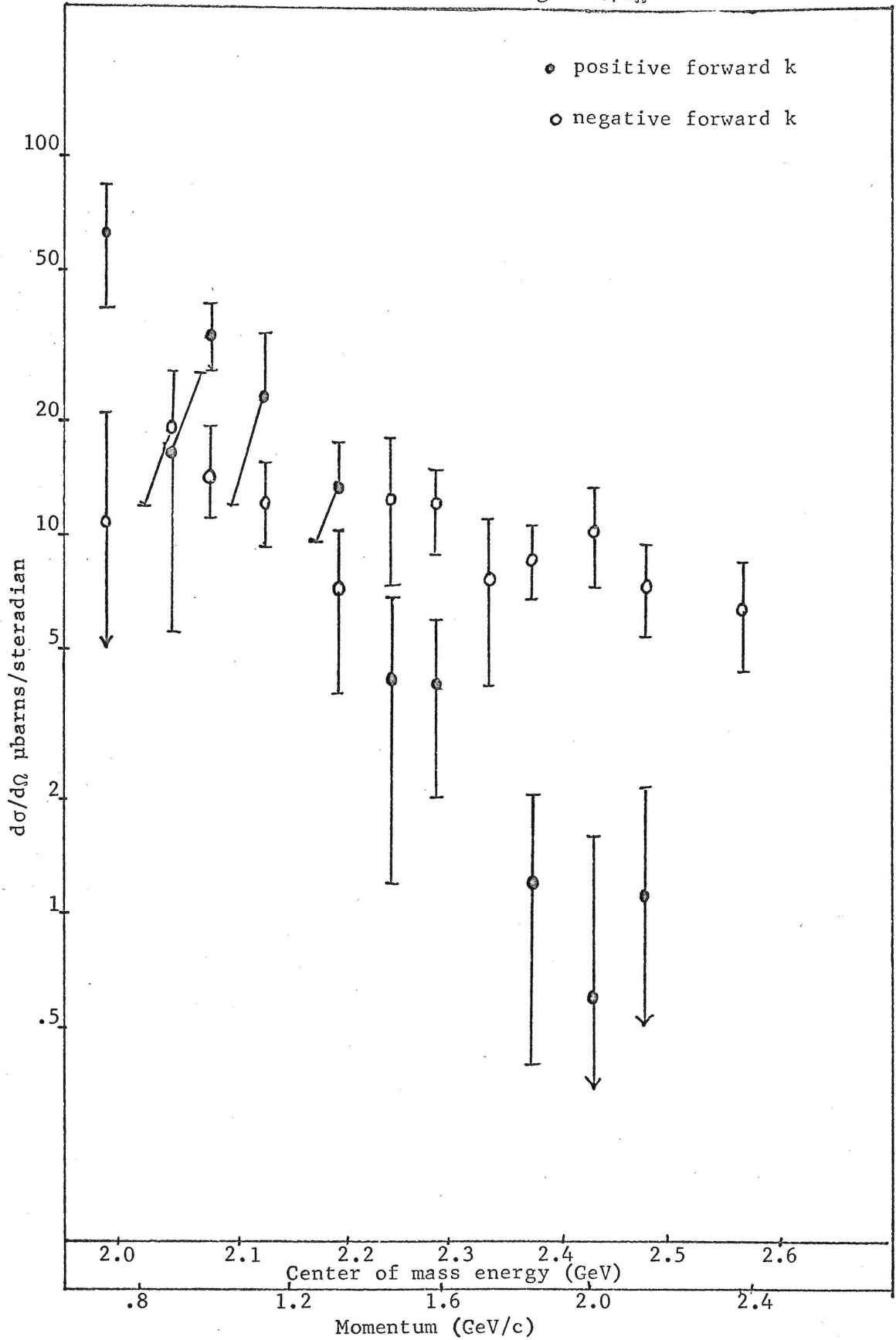


Figure 4.6: Kaon Extreme Angle $d\sigma/d\Omega$ 

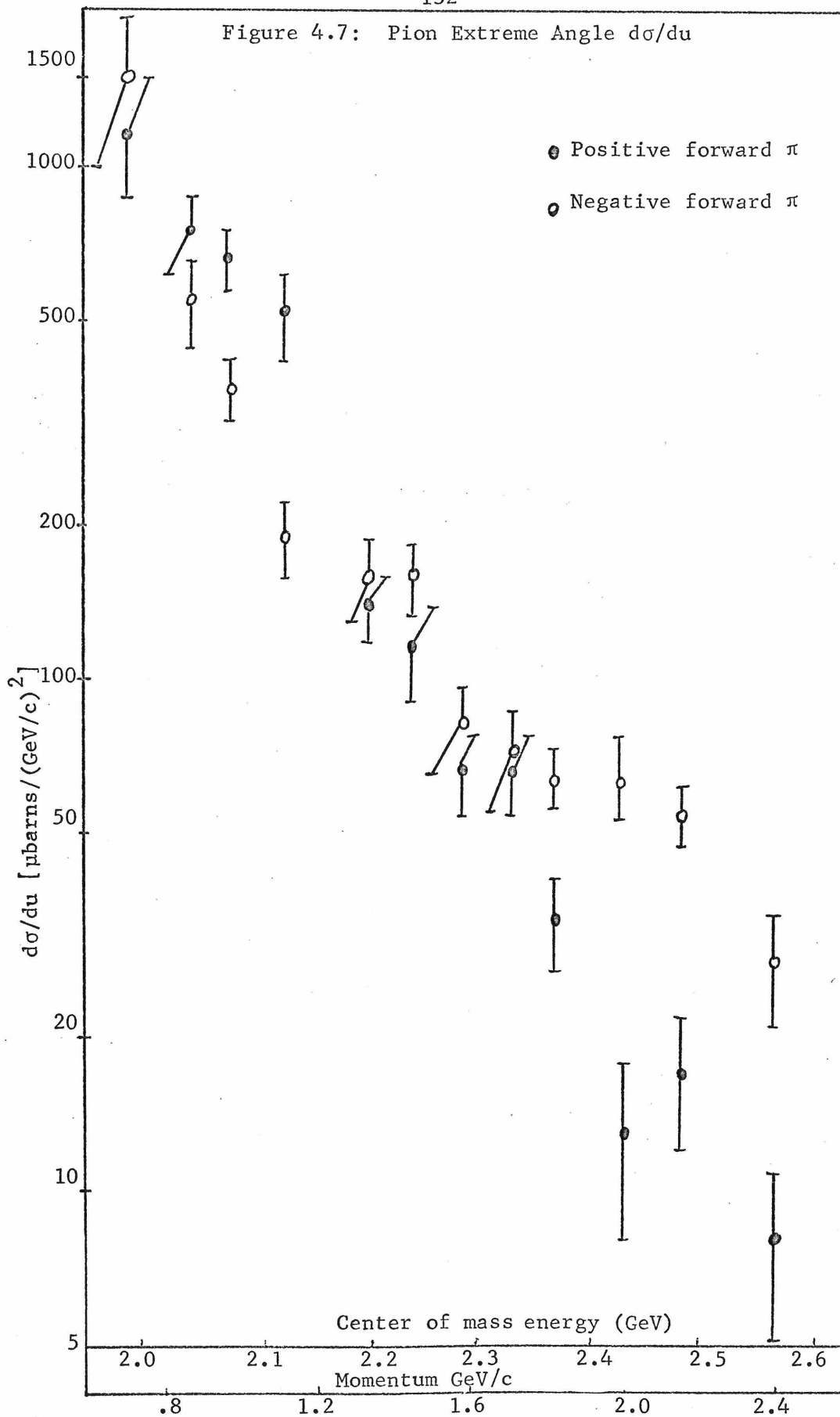


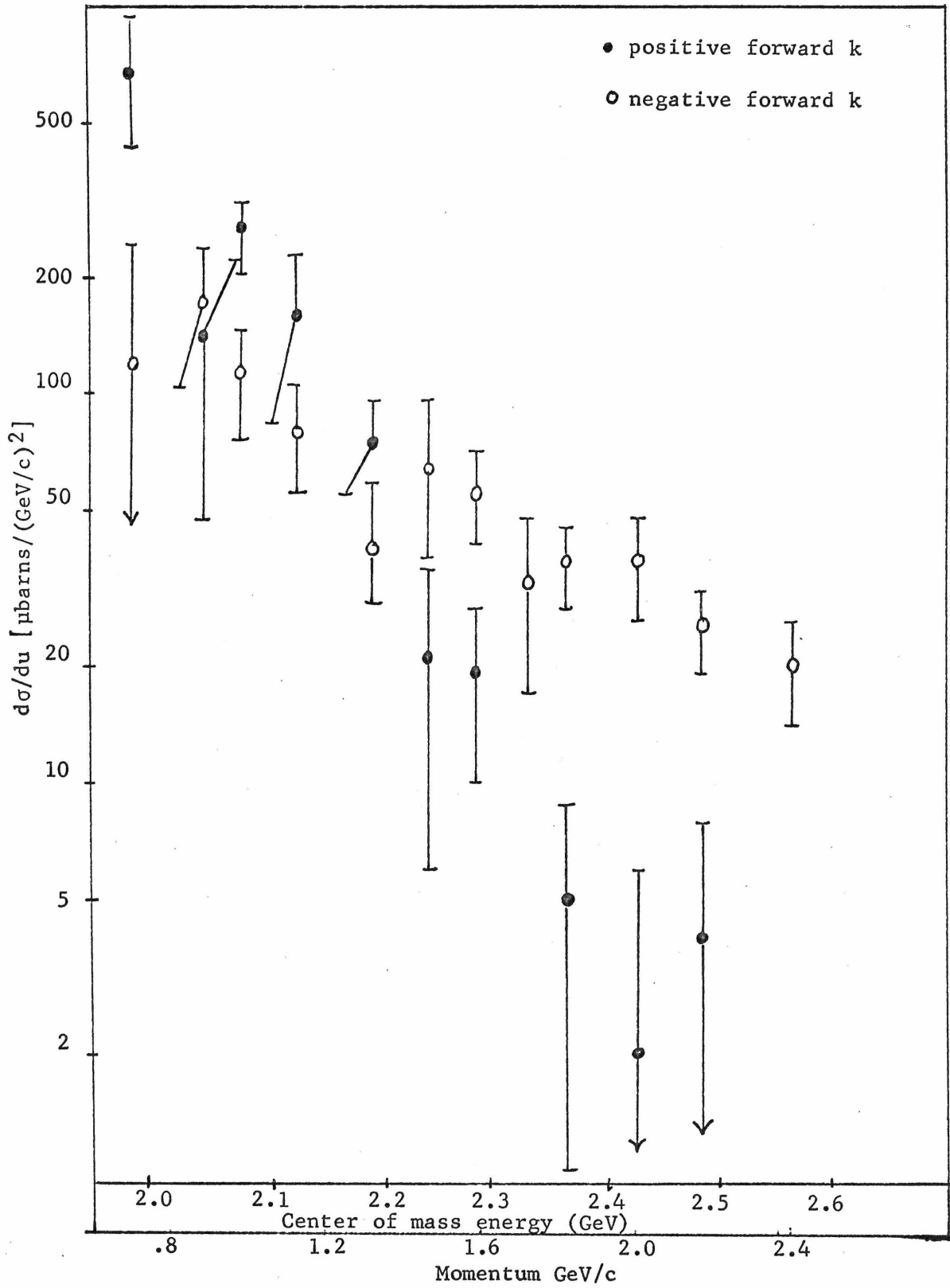
Figure 4.8: Kaon Extreme Angle $d\sigma/du$ 

Table 4.7

Total cross sections for the reactions $\bar{p}p \rightarrow \pi^+\pi^-$ and $\bar{p}p \rightarrow k^+k^-$

<u>Group</u>	Incident \bar{p} <u>Momentum (GeV/c)</u>	S^2 <u>(GeV)²</u>	$\bar{p}p \rightarrow \pi^+\pi^-$ <u>$\sigma(\mu\text{b})$</u>	$\bar{p}p \rightarrow k^+k^-$ <u>$\sigma(\mu\text{b})$</u>
Berkeley	13) 1.61	5.256	119 ± 30	55 ± 18
Michigan	14) 1.62	5.272	137 ± 16	51 ± 10
"	1.77	5.522	109 ± 14	51 ± 10
"	1.83	5.617	76 ± 12	39 ± 8
"	1.89	5.717	84 ± 11	34 ± 8
"	1.95	5.818	53 ± 10	35 ± 8
"	2.20	6.250	32 ± 8	21 ± 6

CHAPTER V

Discussion of the Results

Introduction

Because of the limited amount and the poor statistical accuracy of the data in which the sign of the charge of the forward going particle could be determined, a resonance fit to the two pion annihilation was made to the folded data only. This was considered to be a reasonable procedure for finding dominant structure in the data since

- a) The forward-backward asymmetry of the two pion annihilation is $\lesssim 2.0$ (Figure 4.5) over the entire range of incident antiproton momenta except near 2.0 GeV/c, and
- b) Energy averaged bubble chamber data between 1.6 and 2.2 GeV/c incident antiproton momentum (Figure 1.2b) show considerable symmetry about $\cos \theta_{\text{cm}} = 0$. A detailed account of the resonance model and an alternative background model is given in Section V-1.

Comparisons of the cross sections $d\sigma/du$ for $\pi^{\pm}p$ and $k^{\pm}p$ backward scattering and $\bar{p}p$ annihilations into $\pi^{+}\pi^{-}$ and $k^{+}k^{-}$ using equation (1.6) have been made and are discussed in Section V-2. Conclusions which have been drawn from this experiment are given in Section V-3.

1. Resonance and Background Interpretation of the Folded Data

In order to attempt to explain the differential and total cross section data by means of a simple model, a resonance fit was first made to the folded two pion differential cross section data. Justification for the use of a resonance model to explain the data can be found in Figure 5.1 which presents the two pion total cross sections multiplied by the squared center-of-mass antiproton momentum for the data of this experiment and the one of Bizzarri et al., (Figure 1.3), and shows a large Breit-Wigner shaped peak near 1.0 GeV/c incident antiproton momentum. Additional justification for a resonance model attempt to fit the two pion system comes from the large number of $B = 0$ structures with masses between 1990 and 2570 MeV corresponding to incident antiproton between .7 and 2.4 GeV/c which are given in Table 5.1.

The expression for the reaction amplitude partial wave decomposition for particles A and B each with arbitrary spin interacting to form particles C and D also with arbitrary spin has been derived by Blatt and Biedenharn and is given below

$$q_{\alpha's'm';\alpha,s,m}(\theta,\varphi) = \sum_{J=0}^{\alpha} \sum_{M=-J}^J \sum_{\ell=|J-s|}^{J+s} \sum_{\ell'=|J-s'|}^{J+s'} \sum_{\mu'=-\ell'}^{\ell'}$$

$$i^{\ell-\ell'} \sqrt{(2\ell+1)\pi} (ls0m_s | lsJM) (\ell's'\mu'm_s' | \ell's'JM) \\ (\delta_{\alpha'\alpha} \delta_{s's} \delta_{\ell'\ell} - S_{\alpha's'\ell'}; \alpha_{s\ell}^J) Y_{\ell'}^{\mu'}(\theta, \varphi) \quad (5.1)$$

where primes refer to final states, α refers to the channel type, s , ℓ , and J are spin, orbital angular momentum and total angular momentum quantum numbers, m_s , m_ℓ and M are the corresponding magnetic quantum numbers, $(ls0m_s | lsJM)$ and $(\ell's'\mu'm_s' | \ell's'JM)$ are Clebsch-Gordon coefficients, the $Y_\ell^m(\theta, \varphi)$ are spherical harmonics and S is the scattering matrix relating the initial to the final states.³⁶⁾ This equation can be considerably simplified by quantum numbers constraints on the initial and final states of the annihilation reaction.³⁷⁾

Charge conjugation for a particle-antiparticle pair is given by the equation

$$C = (-1)^{\ell + s} \quad (5.2)$$

while the parity of a boson-antiboson pair and a fermion-antifermion pair are given by

$$P_{\text{boson-antiboson}} = (-1)^\ell \quad (5.3)$$

$$P_{\text{fermion-antifermion}} = (-1)^{\ell + 1} \quad (5.4)$$

Since the $\bar{p}p$ system comprises a fermion-antifermion pair, the $\pi^+\pi^-$ and k^+k^- systems are boson-antiboson pairs, and the total spin J of either meson-antimeson system equals the orbital spin ℓ since the

pions and kaons have intrinsic spin s equal to zero, combining the equations 5.3 and 5.4 gives

$$J = \ell + 1 \pmod{2}. \quad (5.5)$$

Furthermore, since the maximum intrinsic spin s available in the $\bar{p}p$ system is 1, equation 5.5 further simplifies to

$$J = \ell \pm 1 \quad (5.6)$$

Assuming charge conjugation conservation in the annihilation reactions and the use of equation 5.2 yields

$$J = \ell + s \quad (5.7)$$

Equations 5.6 and 5.7 can then be used to show that the $\bar{p}p$ system can annihilate into two pion or two kaon pairs only if $s = 1$.

G parity for a state with n pions is given by

$$G_{\text{pion}} = (-1)^n \quad (5.8a)$$

and for a spinless meson-antimeson pair by

$$G_{\text{kk}} = (-1)^{J+I} \quad (5.8b)$$

Combining equation 5.8a with $n = 2$ with equation 5.8b and observing that $I = 0$ or 1 in the $\bar{p}p$ initial state produces the constraint that the G parity is $+$ and that $J + I$ is even for a pion-antipion final state. This is equivalent to requiring the amplitude to be even under the interchange of the final state pions. Since no equation

similar to 5.8a exists for the kaon-antikaon system, no G parity constraint exists, and there are twice as many available final two kaon states in the two kaon annihilation channel as in the two pion annihilation channel.

Finally, isotopic spin decompositions of the two charged pion, two charged kaon, and two neutral pions and kaons are given in Table 5.2.³⁸⁾ The convention used in this table is that the particle in the right-hand side of the bracket is the particle moving in the beam (+z) direction. The T matrix is defined in the usual way.³⁹⁾

Taking these quantum number considerations into account and using any standard reference for expressions for the Clebsch-Gordon coefficients,⁴⁰⁾ the two pion and two kaon annihilation reaction amplitudes can be written (including the factor 1/k)

$$\begin{aligned}
 a_{11,00} = & \frac{i}{k} \sqrt{\frac{\pi}{2}} \sum_{J=1}^{\infty} \{ -\sqrt{J+1} [\langle \bar{M}\bar{M} | T^{J=\ell+1} | \bar{P}\bar{P} \rangle] \\
 & + \sqrt{J} [\langle \bar{M}\bar{M} | T^{J=\ell-1} | \bar{P}\bar{P} \rangle] \} Y_J^1(\theta, \varphi)
 \end{aligned} \tag{5.9a}$$

$$\begin{aligned}
 a_{10,00} = & \frac{i}{k} \sqrt{\pi} \sum_{J=0}^{\infty} \{ -\sqrt{J} [\langle \bar{M}\bar{M} | T^{J=\ell+1} | \bar{P}\bar{P} \rangle] \\
 & - \sqrt{J+1} [\langle \bar{M}\bar{M} | T^{J=\ell-1} | \bar{P}\bar{P} \rangle] \} Y_J^0(\theta, \varphi)
 \end{aligned} \tag{5.9b}$$

$$\begin{aligned}
q_{1-1,00} &= \frac{i}{k} \sqrt{\frac{\pi}{2}} \sum_{J=1}^{\infty} \{ -\sqrt{J+1} [\langle \bar{M}\bar{M} | T^{J=\ell+1} | p\bar{p} \rangle] \\
&\quad + \sqrt{J} [\langle \bar{M}\bar{M} | T^{J=\ell-1} | p\bar{p} \rangle] \} Y_J^{-1}(\theta, \varphi).
\end{aligned} \tag{5.9c}$$

where the superscript on the T matrix refers to the relationship between total spin and initial state orbital spin and the α' and α subscripts on the quantity q have been omitted. The quantities in square brackets are given in Table 5.2. These amplitudes may then be combined in various ways to give unfolded cross sections and folded cross sections for two charged or neutral pion or kaon final states.

Specializing to pions, averaging over initial spin directions and summing over final spin directions gives the following expression for the unfolded cross section when π^- travels forward along the beam (+z) direction

$$\begin{aligned}
\frac{d\sigma}{d\Omega} &= \frac{\pi}{2k^2} [\{ | \sum_{J=1}^{\infty} [\sqrt{\frac{J+1}{2}} (\frac{1}{2} T_1^{J=\ell+1} + \sqrt{\frac{1}{6}} T_0^{J=\ell+1}) \\
&\quad - \sqrt{\frac{J}{2}} (\frac{1}{2} T_1^{J=\ell-1} + \sqrt{\frac{1}{6}} T_0^{J=\ell-1})] Y_J^1(\theta, \varphi) | \}^2] \\
&\quad + \frac{\pi}{4k^2} [\{ | \sum_{J=0}^{\infty} [\sqrt{J} (\frac{1}{2} T_1^{J=\ell+1} + \sqrt{\frac{1}{6}} T_0^{J=\ell+1}) \\
&\quad + \sqrt{J+1} (\frac{1}{2} T_1^{J=\ell-1} + \sqrt{\frac{1}{6}} T_0^{J=\ell-1})] Y_J^0(\theta, \varphi) | \}^2]
\end{aligned} \tag{5.10}$$

To obtain the expression for the folded cross section, the cross section obtained from equation 5.10 by the replacements $\theta \rightarrow \pi - \theta$, $\varphi \rightarrow \varphi + \pi$ is added to the cross section calculated from equation 5.10. To obtain the expression for the annihilations into neutral pions the amplitudes for θ, φ and $\pi - \theta, \varphi + \pi$ must be added before squaring. The resulting expression for the cross section is four times the right-hand side of equation 5.10 with T_1 set equal to zero (since the I spin of the neutral two pion system is always even).

The assumption of resonance dominance of the amplitude permits the substitution of a standard resonance form (plus constant complex background term) for the T matrix. Using the following form for the T matrix

$$T^{J=\ell+1} = \frac{A_J}{\epsilon_J - i} + A'_J \quad (5.11a)$$

$$T^{J=\ell-1} = \frac{B_J}{\epsilon_J - i} + B'_J \quad (5.11b)$$

where $\epsilon_J = - (s - m_{R_J}^2) / m_{R_J} \Gamma_J$, s is the total center-of-mass energy squared, m_{R_J} is the mass of the resonance, Γ_J is the full width of the resonance, and A_J and B_J are real numbers related to the partial production and decay widths in the two meson annihilation channels, the expression 5.10 can be fit to the folded data.⁴¹⁾

The resonance model expressions for the folded data and for the two neutral pion annihilations have been fit to the data of this experiment and the $\bar{p}p \rightarrow \pi^0 \pi^0$ data obtained from an earlier Caltech experiment which is given in Table 5.3 by means of a nonlinear

gradient fitting program using the method developed by Powell.⁴²⁾ Resonance parameters for the best attempt to fit the folded cross sections which included constant, complex background terms in the $J = 1, 2,$ and 3 partial waves and allowed strengths, masses and widths of the resonances as well as the background parameters to vary, are given in Table 5.4 along with a simple single resonance fit to the neutral two pion data. (Neither the width nor the parameters A_J or B_J were energy dependent in this simple fit.)⁴³⁾ As can be seen from the table, $J = 3$ and $J = 5$ were the dominant spins required to reproduce the folded data and $J = 2$ was the dominant spin required to reproduce the neutral two pion data. The dominant $J = 3$ and $J = 5$ contributions to the folded data, surprising at first in view of the peaking of the a_8 Legendre coefficient (Figure 4.4), are due to the fact that the spherical harmonics Y_3^1 and Y_5^1 can interfere to give a term similar to $|Y_4^0|^2$ without the strong peaking near $|\cos \theta_{\text{cm}}| = 1.0$ characteristic of this polynomial. The solid line in Figures 5.1, 5.3, 5.4 and 5.5 shows how well this resonance model fit reproduces the two pion annihilation data.

Two resonances of spin $J = 3$ and $J = 5$ are theoretically predicted to exist in this energy region in a quark model for boson resonances described by G. and S. Goldhaber⁴⁴⁾. Assuming mesons are formed from a quark-antiquark ($q\bar{q}$) pair each with spin $1/2$ and only spin excitations are allowed, various meson states can be formed with different masses and definite values of total spin J , parity P and charge conjugation C . States in which $P = (-1)^J$ (normal P) and

$C = (-1)^{J+1}$ (abnormal C) are not allowed in this model. (Normal P or C and abnormal P or C are defined to be $(-1)^J$ and $(-1)^{J+1}$, respectively.) It is assumed that states with given orbital excitations ℓ may be further split in mass by the interaction between orbital spin ℓ and the total quark spin s and that this splitting is small relative to the orbital splitting. Using the low mass boson resonances to set the scale, a diagram of predicted mass states vs. total spin J and orbital spin ℓ can be obtained (Figure 5.6).

Such a model predicts two heavy isospin 1, negative parity meson resonances with total spin 3 and 5 at s values of ~ 4.3 and ~ 4.9 , respectively, in reasonably good agreement with the resonance parameters obtained from a fit to the folded two charged pion annihilation discussed in Section V-1 (Table 5.4). Whether the model's predictions can be taken seriously however, is questionable in view of its failure to predict any resonances in the center-of-mass energy range of the $\bar{p}p \rightarrow \pi^0\pi^0$ experiment which is an $I = 0$ system.

A possible reason for the failure of this experiment to detect more of the previously reported $B = 0$ structures in the mass range of this experiment is due to lack of sufficient mass resolution to detect the narrow structures. Although the data were taken at center-of-mass intervals of 40 MeV, the total two pion and two kaon annihilation cross sections given in Chapter IV have been obtained from a Legendre polynomial fit to the combined results of this experiment and the one of Fong. Consequently, the cross section values are subject to the details of the fit to the folded angular distri-

butions and the relative normalization errors between the two experiments and it is unlikely that a resonance with a width less than 40 MeV and producing a resonance cross section less than half the measured cross section would be observed in these results.

Another possible explanation for the failure of this experiment to detect many of the reported $B = 0$ structures may be related to an angular momentum barrier for $\bar{p}p$ system⁴⁵⁾. The CERN R, S, T, and U structures fall closely along the ρ trajectory and the R and T structures might be interpreted as Regge recurrences of the ρ and the S and U structures Regge recurrences of the f_0 . However, diffraction fits to the $\bar{p}p$ elastic scattering system have required a proton interaction radius of ~ 1.0 fermi. Figure 5.7 shows that maximum total spin which can be formed in the $\bar{p}p$ system under such an assumption is smaller than the total spin required to couple to the CERN structures. In comparison, the pion nucleon system for the same nucleon interaction radius is seen to have sufficient total spin to couple to the commonly observed N^* resonances.

The nonvanishing cross sections for $\bar{p}p \rightarrow \pi^0 \pi^0$ in this momentum region, the lack of any dominant even J contributions needed to produce the observed forward backward asymmetry in the unfolded data, and the fact that the energy dependence of the widths and partial widths were neglected in the fit, indicate that the resonance model fit is only a first approximation to the physical processes involved in the annihilation. Consequently, other attempts were made to fit the T matrix elements to the data without assuming a resonance model.

Another model for the pion annihilation data which looked promising in view of the relatively smooth increase in complexity of spin dependence in the folded angular distributions with increasing incident antiproton laboratory momentum was a background model in which the target proton was treated as a scattering center with a fixed scattering radius. In this model, the maximum angular momentum obtainable in the antiproton proton system is given by the product of the scattering radius times the incident laboratory antiproton momentum,

$$L = 5.076 R_s q \quad (5.12)$$

where R_s is the scattered radius in units of 10^{-15} m, q is the center-of mass antiproton momentum in GeV/c and $L = \sqrt{\ell(\ell + 1)}$ where ℓ is the orbital angular momentum in the antiproton-proton system.

Table 5.5 gives the minimum laboratory momenta (P_0) necessary to obtain orbital angular momenta ℓ up to $\ell = 6$ for three scattering radii.

In order to obtain an analytic expression for the T^J matrix elements which could be fit to the folded pion data, it was assumed that

a) the matrix elements $T^{J = \ell - 1}$ were zero

b) the energy dependence of the matrix element $T^{J = \ell + 1}$ was given

by

$$T^{J=\ell+1} = \left(\frac{5.076 R_s q}{L} \right)^{2\ell + 1} A_\ell s^{-2.65} \quad q < \frac{L}{5.076 R_s} \quad (5.13a)$$

$$T^{J=\ell+1} = A_\ell s^{-2.65} \quad q \geq \frac{L}{5.076 R_s} \quad (5.13b)$$

where A_ℓ was an adjustable fitting parameter and the s dependence

was chosen so that the s dependence of the total two pion annihilation cross section which could be calculated from equation 5.10 agreed with the measured $s^{-6.3}$ dependence (Chapter IV). The $q^{2\ell+1}$ T matrix threshold dependence which appears in equation 5.13a is obtained from nonrelativistic scattering theory⁴⁶⁾.

Using the expressions for $T^{J=\ell+1}$ given in equation 5.13 in equation 5.10 and allowing the parameters A_ℓ and R_s to vary, an attempt was made to fit the folded pion data over the incident antiproton laboratory momentum region covered in this experiment. No quantitatively acceptable fits to the data were obtained over a wide range of parameter starting values. Although this does not rule out the possibility that a satisfactory fit to the data could be made with the background model, it suggests that the assumption of a constant proton scattering radius may not be valid for the two pion annihilation reaction over the momentum range of this experiment.

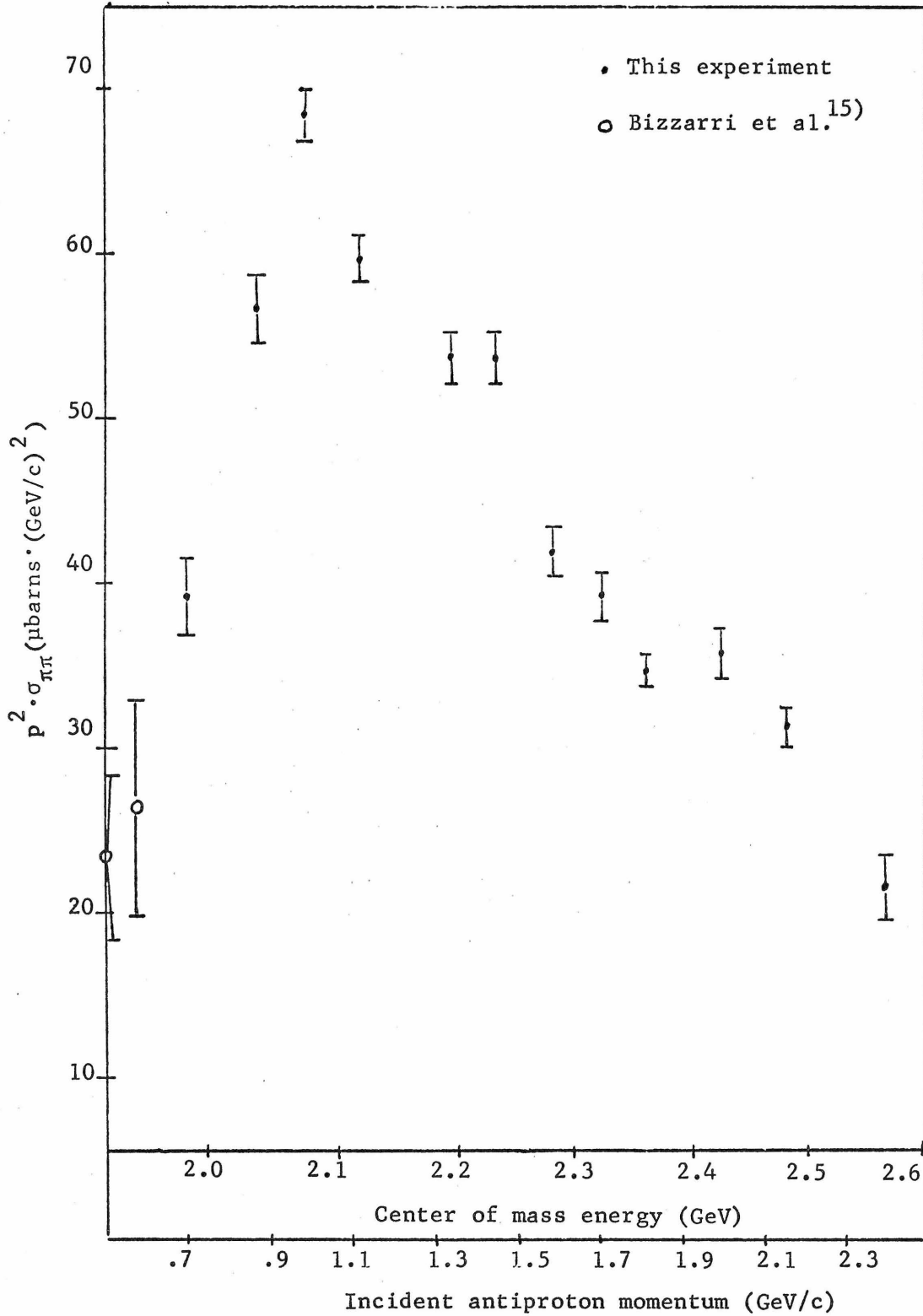
Another attempt to fit the T matrix elements directly to the data without using a model for the energy dependence was made, a method similar to that used in an energy independent phase shift analysis. However, the large number of low χ^2 solutions obtained for the low momentum data (> 10 for momenta ≤ 1.0 GeV/c) made such a procedure impractical both from time and cost considerations. Unfolded data over the entire angular region combined with polarized proton target data to sort out the correct fit from the many acceptable fits obtained from energy independent fitting procedures for high spin ($J \leq 6$) systems are needed to produce reliable T matrix

values from this type of analysis.

For completeness, the equations for the differential cross sections for the antiproton proton annihilations into two charged pion and two charged kaon for a polarized proton target in terms of the amplitudes 5.9a - 5.9c are given in Appendix E. These equations can be used to relate asymmetries in positive or negative pion or kaon production from antiproton annihilation on a polarized proton target to the T matrix elements for these annihilation reactions.

148
Figure 5.1

Center of mass antiproton momentum squared times $\bar{p}p \rightarrow \pi\pi$
total cross section



149
Figure 5.2

Center of mass antiproton momentum squared times $\bar{p}p \rightarrow k\bar{k}$
total cross section

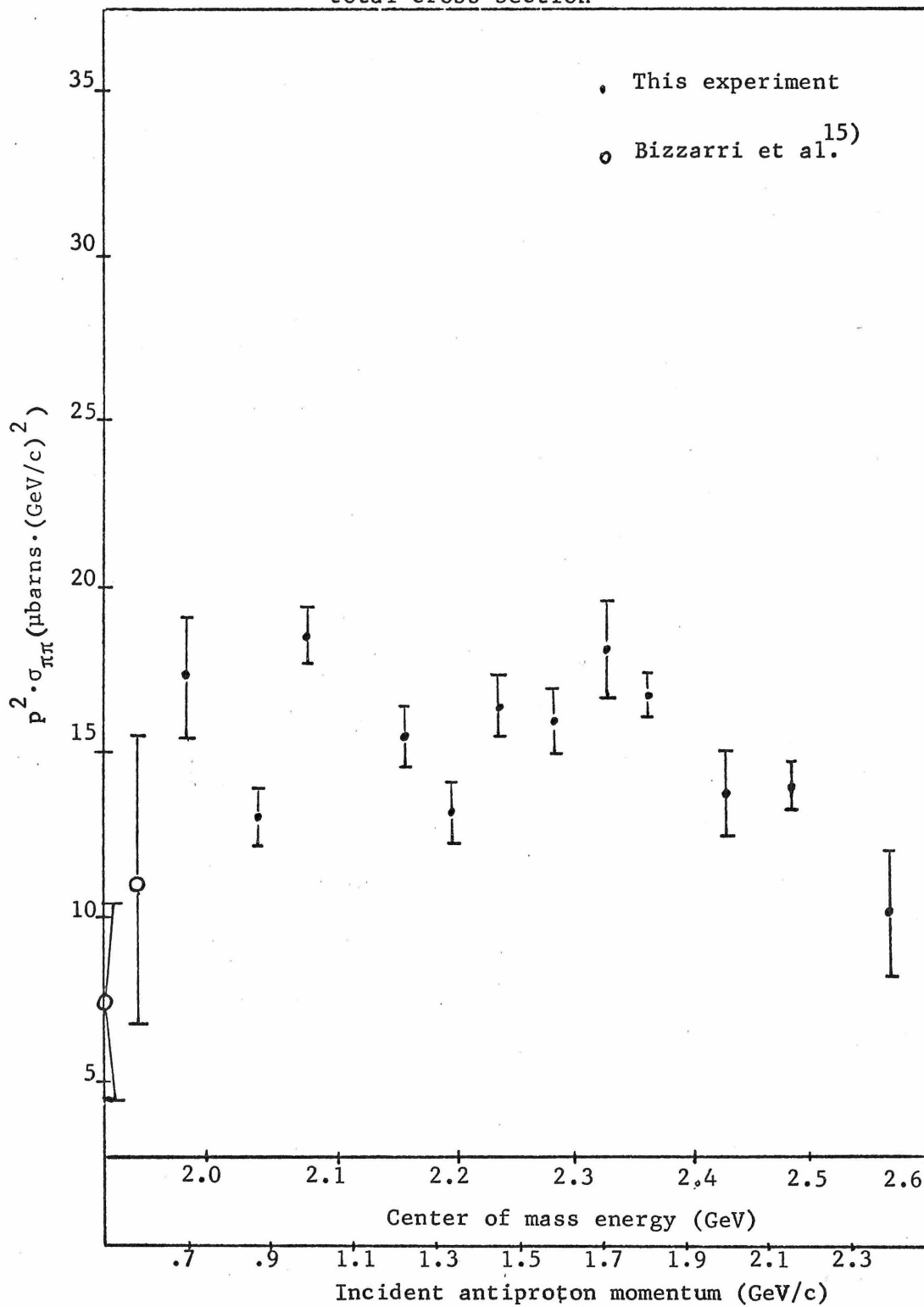


Figure 5.3: Resonance fit to pion folded differential cross sections.

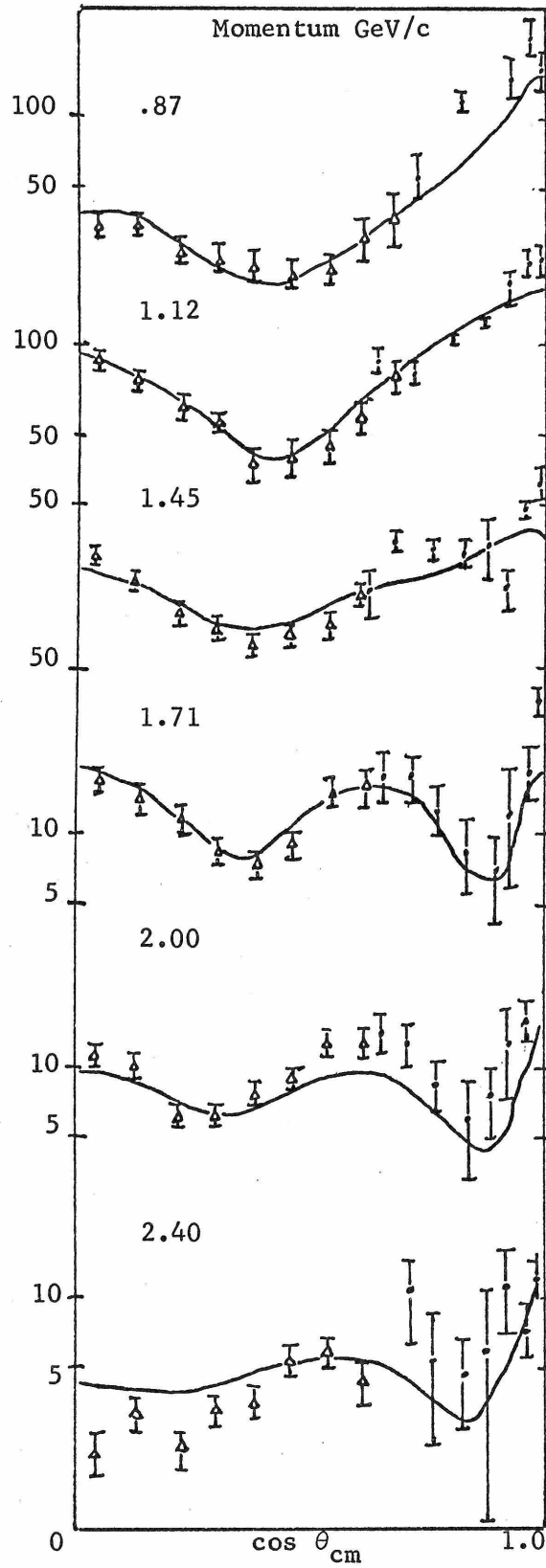


Figure 5.4

Resonance fit to pion total cross sections

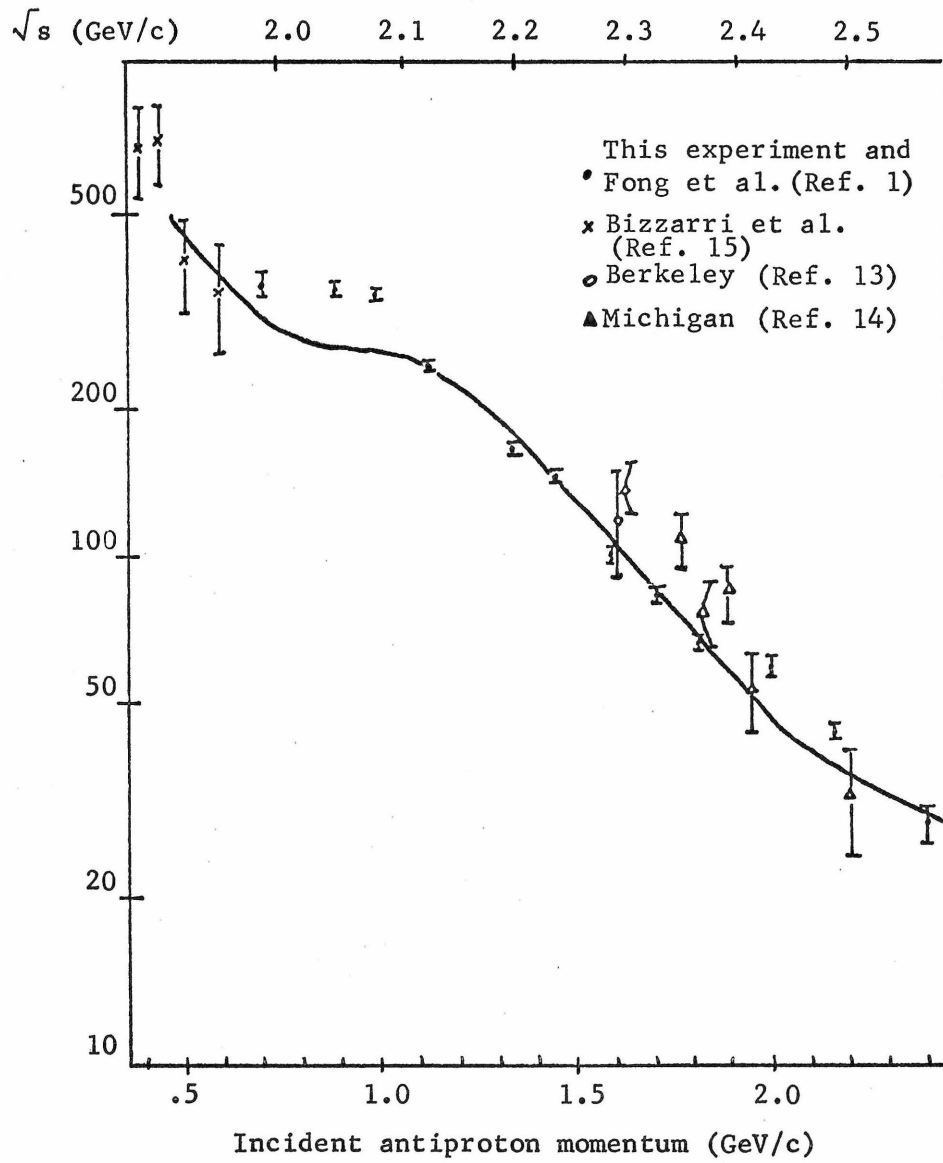


Figure 5.5: Resonance fit to Legendre expansion coefficients

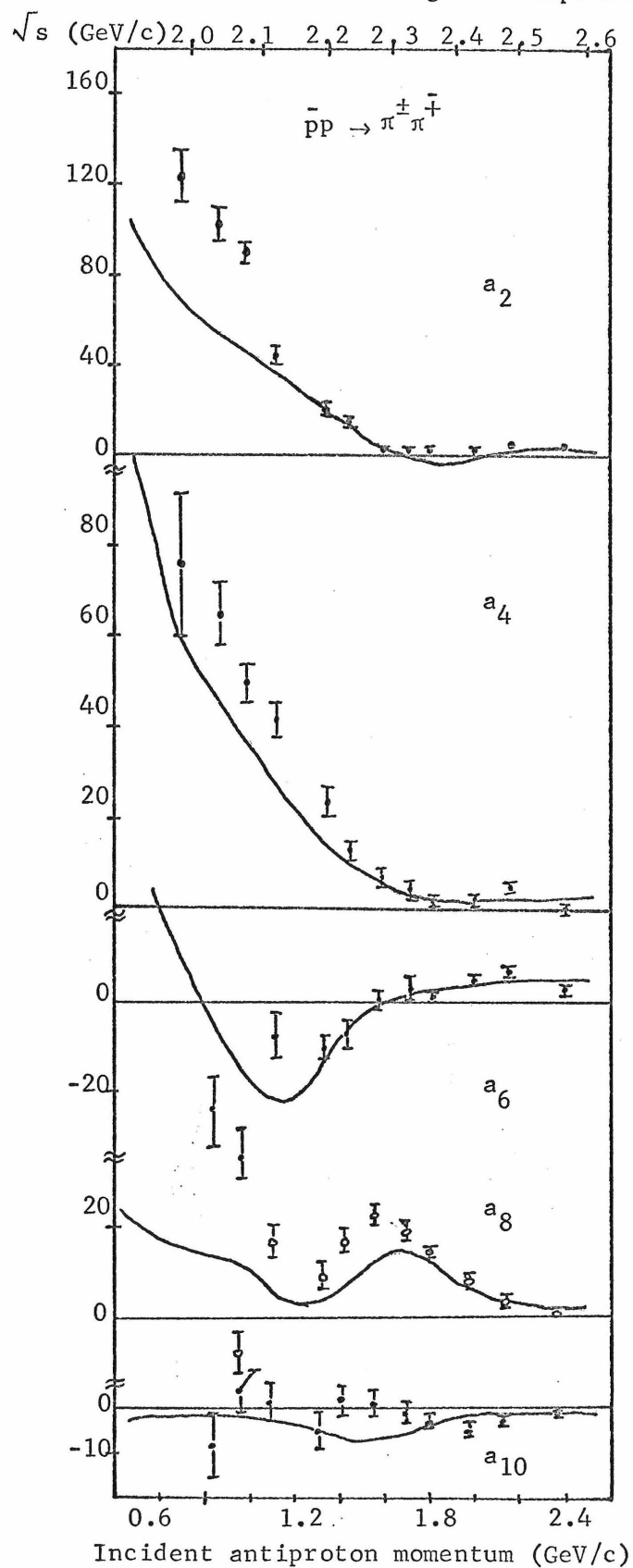


Table 5.1

Resonance parameters of reported $B = 0$ structures between 1990 and 2570 MeV.

Reaction	Group	Mass (MeV)	Width (MeV)	I Spin
$\pi^- p \rightarrow pX^-$	CERN ³⁾	1929 ± 14	≤ 35	1 or 2
$\pi^- p \rightarrow pX^-$	Anderson ⁶⁾	2086 ± 38	150	1 or 2
$\bar{p}p$	Abrams ⁵⁾	2190 ± 5	85	1
$\pi^- p \rightarrow pX^-$	CERN	2195 ± 15	≤ 13	1 or 2
$\pi^- p \rightarrow pX^-$	Anderson	2260 ± 18	≤ 25	1 or 2
$\bar{p}p$	Abrams	2345 ± 10	140	1
$\bar{p}N \rightarrow k^* \bar{k} \pi \pi$ or $\bar{p}N \rightarrow \bar{k}^* \pi \pi$	Oh ⁸⁾	2360 ± 25	≤ 60	1
$\pi^- p \rightarrow pX^-$	Anderson	2370 ± 17	57	1 or 2
$\bar{p}p$	Abrams	2380 ± 10	140	0
$\pi^- p \rightarrow pX^-$	CERN	2382 ± 24	≤ 30	1 or 2
$\pi^- p \rightarrow pX^-$	Anderson	2500 ± 32	87	1 or 2

Table 5.2

Isotopic Spin Decompositions*

$$|p\bar{p}\rangle = \frac{1}{\sqrt{2}} [|1,0\rangle + |0,0\rangle]$$

$$|\pi^\pm \pi^\mp\rangle = \sqrt{\frac{1}{6}} |2,0\rangle \pm \sqrt{\frac{1}{2}} |1,0\rangle + \sqrt{\frac{1}{3}} |0,0\rangle$$

$$|\pi^0 \pi^0\rangle = \sqrt{\frac{2}{3}} |2,0\rangle - \sqrt{\frac{1}{3}} |0,0\rangle$$

$$|k^\pm k^\mp\rangle = \frac{1}{\sqrt{2}} |1,0\rangle \pm \frac{1}{\sqrt{2}} |0,0\rangle$$

$$|k^0 \bar{k}^0\rangle = \frac{1}{\sqrt{2}} |1,0\rangle + \frac{1}{\sqrt{2}} |0,0\rangle$$

Combining the above yield

$$\langle \pi^\pm \pi^\mp | T | p\bar{p} \rangle = \pm \frac{1}{2} T_1 + \sqrt{\frac{1}{6}} T_0$$

$$\langle \pi^0 \pi^0 | T | p\bar{p} \rangle = -\sqrt{\frac{1}{6}} T_0$$

$$\langle k^\pm k^\mp | T | p\bar{p} \rangle = \frac{1}{2} T_1 \pm \frac{1}{2} T_0$$

$$\langle k^0 \bar{k}^0 | T | p\bar{p} \rangle = \frac{1}{2} T_1 + \frac{1}{2} T_0$$

* The convention used is given in Section V-1.

Table 5.3

$\bar{p}p \rightarrow 2\pi^0$ Data†

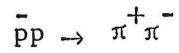
Momentum GeV/c

	1.00	1.25	1.50	1.75	2.00	2.50
$\cos \theta_{\text{cm}}$	$d\sigma/d\Omega$ *					
.0872	4.5 + 1.1	5.8 + 1.2	5.0 + 0.8	2.2 + 0.5	1.3 + 0.2	0.29 + 0.08
.0588	4.5 + 1.4	4.4 + 1.1	2.1 + 0.6	1.0 + 0.4	0.3 + 0.3	0.25 + 0.09
.4226	1.0 + 0.7	1.8 + 0.8	1.2 + 0.6	0.7 + 0.5	0.6 + 0.2	0.19 + 0.13
.5736		3.7 + 2.4	1.6 + 1.2	0.2 + 0.2	0.4 + 0.3	1.2 + 1.5

* Cross sections in microbarns-steradians.

† This data obtained from Alvin V. Tollestrup.

Table 5.4

Resonance Parameters of Best Fits to $\pi\pi$ Annihilation Data

$$A'_1 = -.062 - i .015$$

$$B'_1 = -.041 - i .011$$

$$A_2 = .019 + i .00$$

$$B_2 = .023 + i .00$$

$$A'_3 = .022 + i .091$$

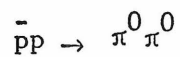
$$B'_3 = -.024 + i .128$$

$$A_3 = - .426 \quad B_3 = - .093 \quad M_3 = 2.132 \quad \Gamma_3 = .320 \quad s = 4.52$$

$$A_5 = .048 \quad B_5 = - .065 \quad M_5 = 2.287 \quad \Gamma_3 = .159 \quad s = 5.24$$

Since these resonances decay into two pions

$I = 1$, $P = -$ and $G = +$ for both



$$A_2 = .114 \quad B_2 = .075 \quad M_2 = 2.217 \quad \Gamma_2 = .356 \quad s = 4.90$$

Since this resonance decays into two neutral pions

$I = 0$, $P = +$ and $G = +$.

Table 5.5

Minimum antiproton momenta required to produce an angular momentum ℓ as a function of proton scattering radius R_s (in units of 10^{-15} m).

ℓ	L	$R_s = 1$		$R_s = 1.5$		$R_s = 2.0$	
		q_0^*	P_0^*	q_0^*	P_0^*	q_0^*	P_0^*
0	.0	.0	.0	.0	.0	.0	.0
1	1.41	.282	.60	.186	.380	.141	.285
2	2.45	.490	1.11	.327	.692	.245	.500
3	3.46	.692	1.72	.462	1.030	.346	.740
4	4.47	.892	2.48	.597	1.415	.447	.995
5	5.48	1.095	3.40	.730	1.850	.547	1.265
6	6.49	1.295	4.45	.864	2.346	.647	1.570

* Units are GeV/c

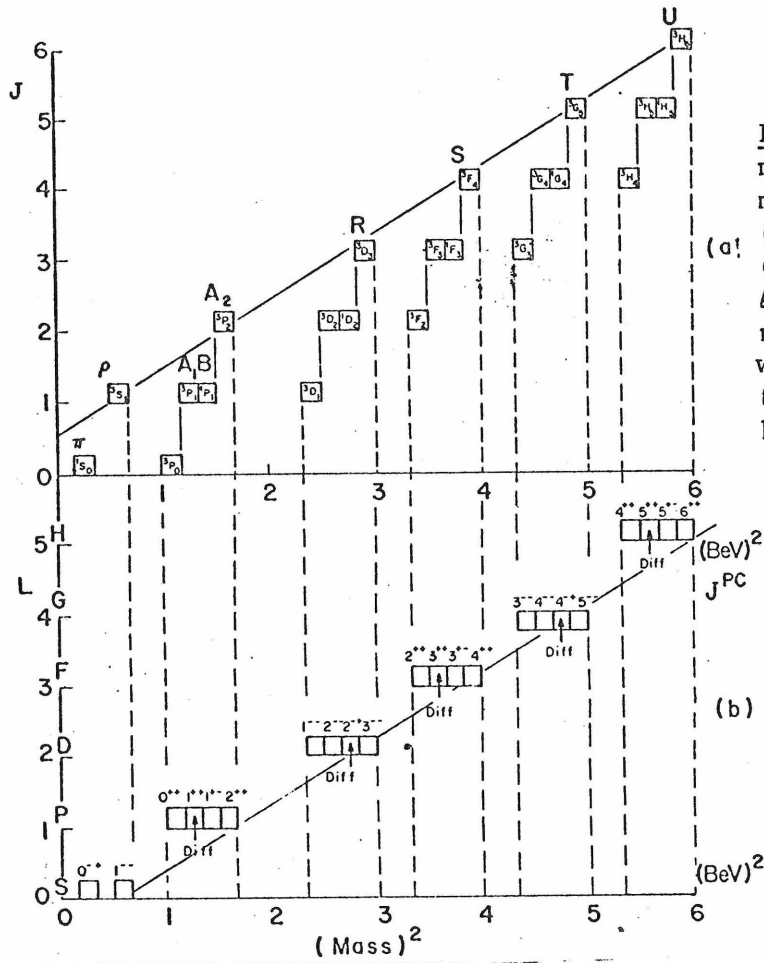
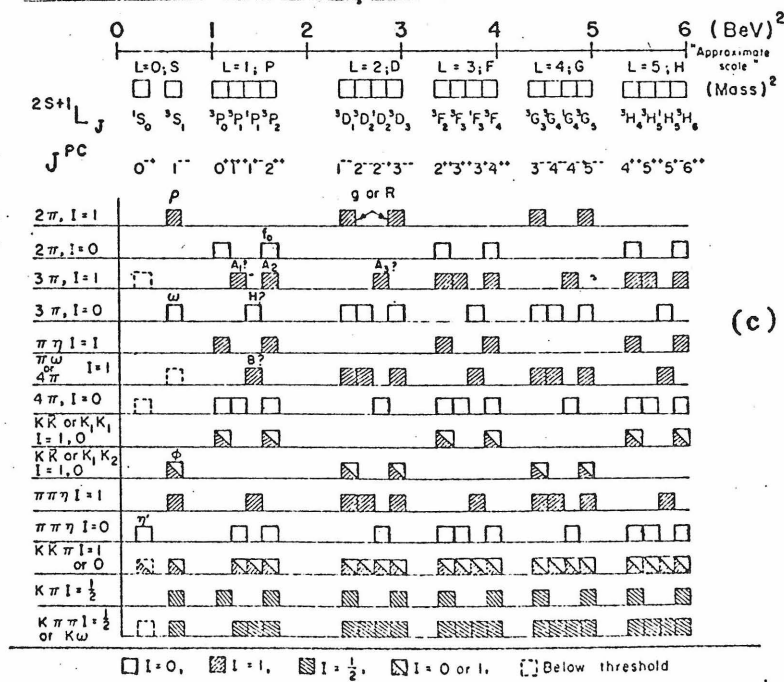


Figure 5.6. Expected mass states of the qq model plotted against (a) J , and (b) L , and (c) allowed decay modes. All masses are approximate. These figures were taken from an article by G. & S. Goldhaber (Ref. 44).



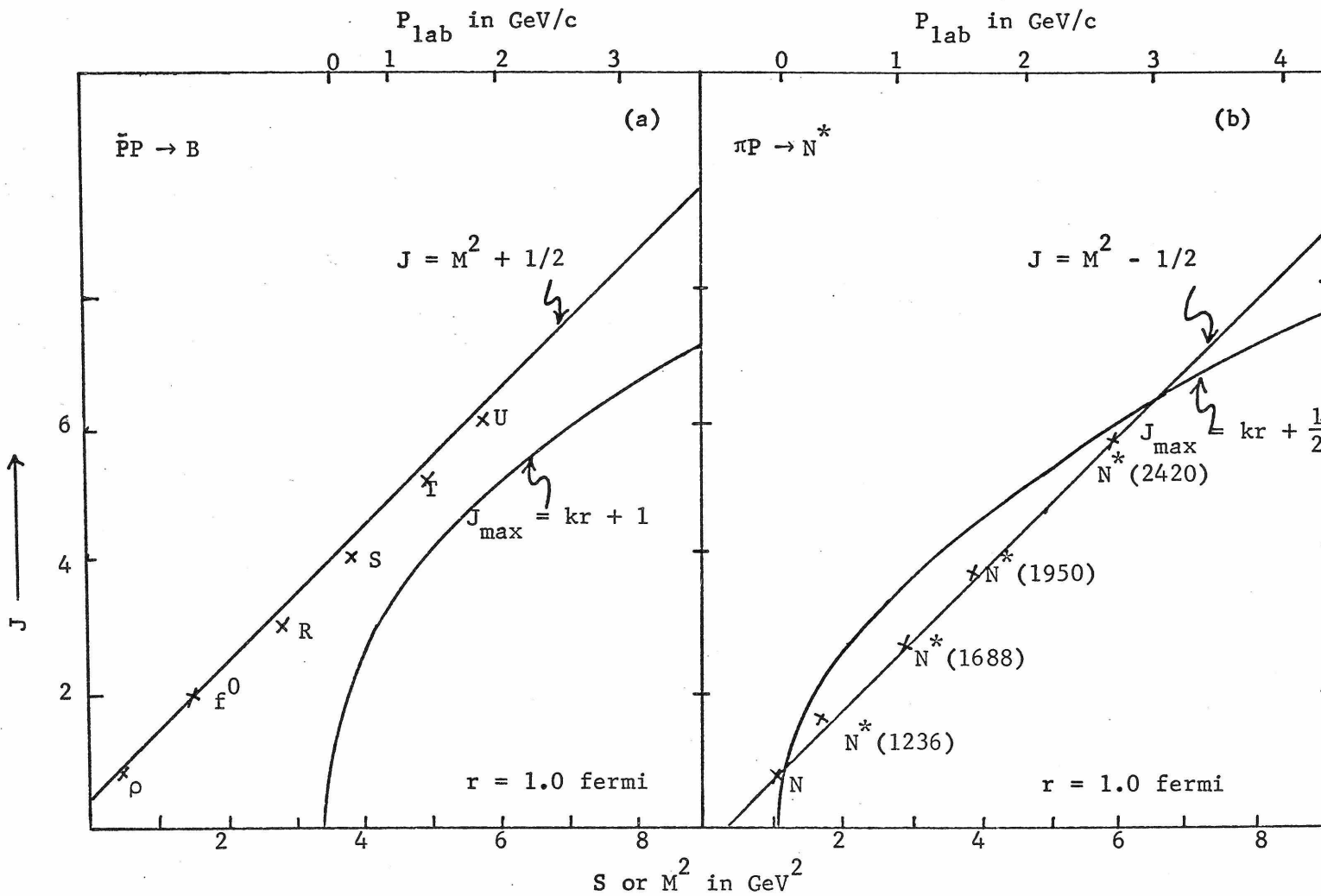


Figure 5.7: Angular momentum barrier for the (a) $\bar{p}p$ and (b) πN systems

2. Comparison of the Extreme Angle Annihilation Data with πp and kp Backward Scattering Data Using Crossing Relations

The concept of crossing which in the case of two-body scattering relates the amplitudes between processes for which a pair of particles is exchanged from the initial to the final state is a fundamental assumption of the S-matrix theory of strong interactions.⁴⁷⁾ In order to apply these relations, it is necessary either to measure the cross sections at asymptotic energies or to make assumptions about the analytic form of the scattering amplitudes in order to do the analytic continuation necessary for crossing.

In the energy regions in which Regge trajectories of the same signature or exchange degenerate trajectories dominate the u channel scattering amplitude and the scattering amplitude is even under the replacement $\sqrt{u} \rightarrow -\sqrt{u}$, equation 1.6 can be used to compare the annihilation cross sections $d\bar{\sigma}/du$ to previously measured backward elastic cross sections $d\sigma/du$ as illustrated in Figure 1.1b. This comparison, shown in Figure 5.6, has been made at fixed $\cos \theta_{cm} = .98$ instead of fixed u to increase the range of s in the comparison; u varies in value between -.44 and -.20 for the two pion annihilation and between -.30 and -.14 (GeV/c)² for the two kaon annihilation over the incident antiproton momentum range of this experiment. The backward scattering cross sections shown in Figure 5.8 have been multiplied by the kinematic crossing factor on the right-hand side of equation 1.6, and all errors are statistical.^{48,49)}

The comparison of the $\bar{p}p \rightarrow \pi^- \pi^+$ to $\pi^+ p \rightarrow p \pi^+$ (reaction 1) shows reasonable agreement everywhere except near $s = 5.0$ (GeV/c) where there is a strong dip in the backward $\pi^+ p$ cross section. Considering the many resonances and the large number of possible exchanges, the comparison is somewhat better than might be expected a priori. It is also interesting to note that both cross sections show a similar shoulder at $s \sim 6.0$ (GeV/c)².

In the comparison of $\bar{p}p \rightarrow \pi^+ \pi^-$ to $\pi^- p \rightarrow p \pi^-$ (reaction 2), direct channel effects, specifically the $N^*(2190)$, eliminate any quantitative agreement between them. Good agreement for these reactions would not be expected except at high momenta where the influence of the direct channel resonances in πp scattering give only small contributions to the complete scattering amplitude.

The agreement in the comparisons of $\bar{p}p \rightarrow k^- k^+$ to $k^+ p \rightarrow p k^+$ (reaction 3) and $\bar{p}p \rightarrow k^+ k^-$ to $k^- p \rightarrow p k^-$ (reaction 4) is striking especially in view of the low momenta at which the comparison is being made. The agreement for reaction 3 is not surprising since the backward $k^+ p$ scattering data can be fit with an exchange degenerate $\Lambda_\alpha, \Lambda_\gamma$ exchange which satisfies the requirements for equation 1.6 to be valid.⁵⁰⁾ However, the good agreement for reaction 4 is not expected since it is usually believed that $k^- p$ backward scattering is dominated by direct channel amplitudes.⁵¹⁾

At high momenta comparisons can be made between the above pairs of cross sections as a function of u for fixed s . The results of these comparisons are shown in Figure 5.9 where the annihilation

data have been averaged over four different momenta (ranging from $s = 5.4$ to $s = 6.2$ $(\text{GeV}/c)^2$ in order to improve the statistics and the backward scattering data have been multiplied by the crossing factor in equation 1.6 as before. For reactions 2 and 4 there is no significant disagreement over the range of u . While the agreement is generally good near $\theta_{\text{cm}} = 180^\circ$ for reactions 1 and 3, there is a marked deviation away from this point, possibly because the scattering amplitude is no longer even in the replacement of \sqrt{u} by $-\sqrt{u}$ away from the extreme center of mass angles.

Figure 5.8

Comparison of annihilation and backward scattering reactions at extreme angles as a function of s .

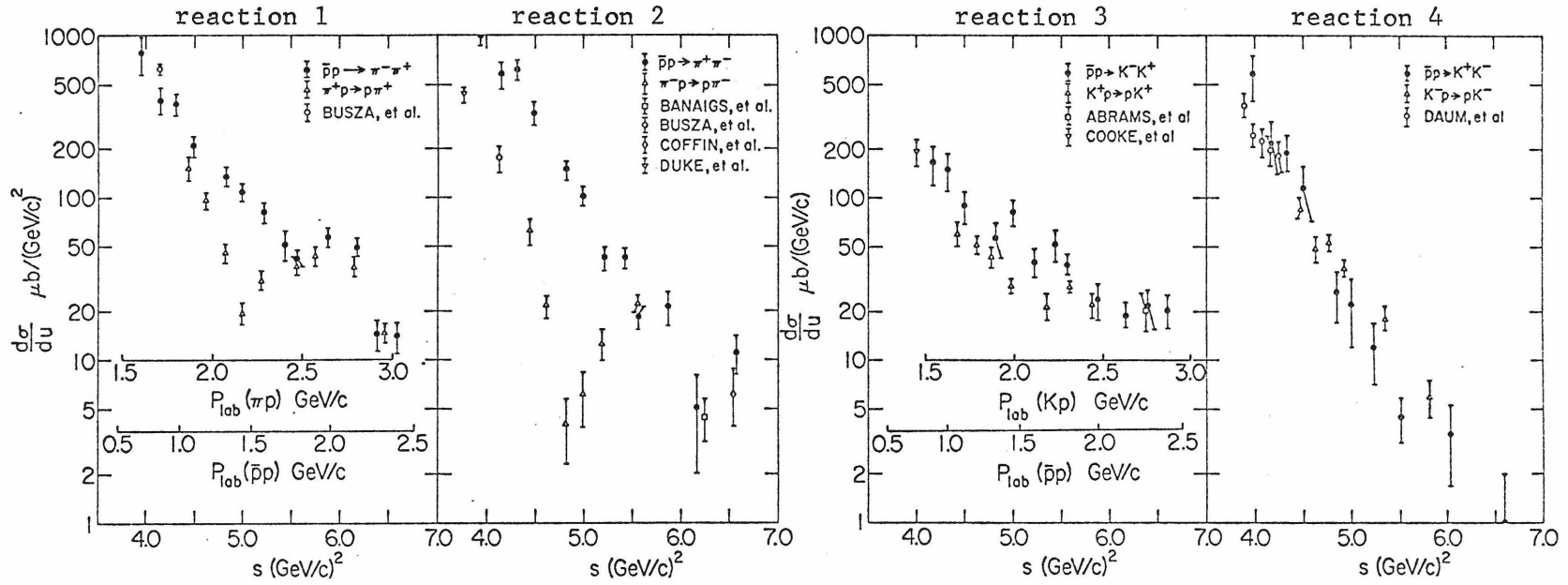
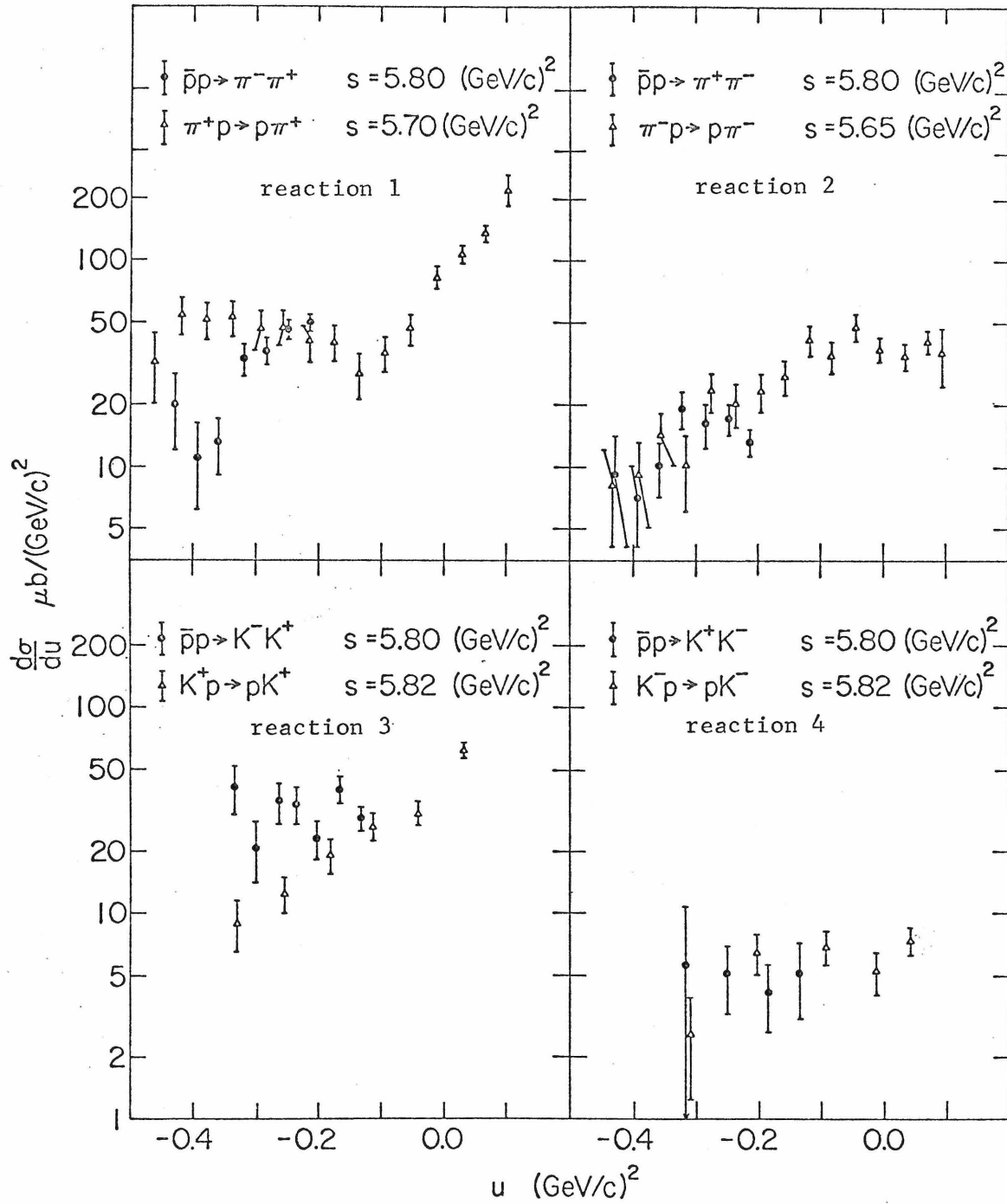


Figure 5.9

Comparison of annihilation and backward scattering reactions at extreme angles as a function of u .



3. Conclusions

The two pion annihilation data obtained in this experiment have been found to be consistent with the interpretation that the direct channel (resonance) effects dominate the amplitude over the momentum region covered by this experiment. Evidence for these resonances has been obtained from the strong peaking in the total pion annihilation cross section near 1.0 GeV/c shown in Figure 5.1, the reasonable fit to the folded angular distributions obtained from a simple $J = 3$ and $J = 5$ two resonance model shown in Figures 5.3, 5.4 and 5.5, and the poor agreement between the comparison of the two pion annihilation reactions with the pion nucleon backward scattering reactions assuming exchange dominance of the scattering amplitudes. Furthermore, the resonance parameters of the low mass resonance (2.12 GeV) obtained in the resonance fit to the folded pion annihilation data are in reasonable agreement with the resonance parameters of the $B = 0$ structure observed by Anderson et al. at a mass of 2.09 GeV (Table 5.1). The stable parameters of this resonance with variations in numbers of resonances and backgrounds included in the fitting procedure are the mass ($2.12 \pm .05$) and the spin $J = 3$.

Although the position of the upper mass resonance (2.28 GeV) is sensitive to background contributions and varies between 1.6 and 2.2 GeV/c depending on the type of resonance model used, a large spin 5 contribution is needed in the amplitude to reproduce the folded data in the vicinity of 1.7 GeV/c where bubble chamber data

have shown the complete unfolded distribution to be relatively symmetric about $\cos \theta_{\text{cm}} = 0$ (Figure 1.2b). More complete data are needed to determine whether the upper mass resonance is real or whether it is merely a dominant background spin at the higher momenta.

All attempts to test the uniqueness of the resonance model have failed because of the complexity of the pion annihilation scattering amplitude containing up to six partial waves ($J \lesssim 6$). Complete data over the entire angular region combined with data from a polarized proton target will ultimately be needed to unambiguously determine the form of the pion annihilation scattering amplitudes in this energy region.

The two kaon annihilation data obtained in this experiment have been found, in contrast, to be consistent with the interpretation that exchange effects dominate the amplitude over the momentum region of the experiment. Although the two kaon folded differential cross sections have been fit with the two pion resonances and an additional spin 4 resonance with variable parameters, the simplicity of the folded angular distributions would not seem to warrant such complexity a priori. (A resonance with negative G parity would not couple to the two pion annihilation channel.) There is no evidence of direct channel structure either in the total two kaon annihilation cross sections (Figure 5.2) or the extreme angle differential cross sections (Figure 4.6). Furthermore, good agreement has been obtained between the extreme angle two kaon

annihilation data and the kp backward scattering data assuming the amplitudes are dominated by u channel exchanges.

The statistical accuracy of the two kaon data obtained in this experiment is too poor to warrant a Regge fit to the data. More complete and accurate data will be needed before reliable parameters in exchange amplitude fits to the data can be obtained.

If the amplitudes of the reactions $k^-p \rightarrow pk^-$ and $\bar{p}p \rightarrow k^+k^-$ are dominated by an exchange, the exchanged particle or trajectory must be exotic (mesons which cannot be formed from a quark-antiquark pair). Presently available experimental information does not exclude the possibility of a Reggeized Z^{*++} ($S = 1$, $B = 1$) exchange with $\alpha(0) \approx -4.0 \pm 1.0$ ⁵²⁾. If such a trajectory had a slope of 1 $(\text{GeV}/c)^{-2}$, it would pass through the vicinity of the higher $I = 1$ peaks of the k^+p total cross section.⁵³⁾

To summarize, the two pion annihilation data show strong resonance behavior in the energy region of this experiment. A simple resonance model fit to the folded pion data has been found which reproduces all the qualitative features of the folded data and requires a resonance of mass 2.12, spin $J = 3$ whose resonance parameters are in reasonable agreement with a previously observed $B = 0$ structure. More detailed fits to the pion annihilation data to verify or invalidate the present resonance model interpretation will require considerably more detailed data because of the large number of partial wave contributions to the annihilation amplitude in the energy region of this experiment.

The two kaon annihilation data show no dominant s channel effects in the amplitude in the energy range of this experiment. And comparisons with kp backward scattering data suggest that the two kaon annihilation amplitudes are dominated by exchanges. The experiment provides no experimental evidence to rule out the possibility of a Reggeized Z^* exchange.

Appendix A

The Beam Transport System

The beam transport system used in this experiment was the short branch of partially separated beam No. 5 at the Brookhaven National Laboratory Alternating Gradient Synchrotron (AGS). The system, consisting of 7 quadrupoles, 3 dipoles, 2 electrostatic beam separators, 2 beam stops, a mass slit and a vacuum system, is shown in Figure 2.1 of Chapter II.

The Brookhaven AGS accelerated between $.7$ and 1.5×10^{12} protons every 2.4 seconds. These were made to strike a Be wire 1 mm in diameter at the 10th magnet of the G superperiod which was flipped into and swept across the beam in approximately 400 msec. The Be wire was angled 10° away from the first set of three quadrupoles to present the smallest possible source to the beam 5 transport system.

The first three quadrupoles Q_1 , Q_2 , and Q_3 were special magnets with most of their materials above and below the beam line enabling them to be located close to the AGS main ring. They focused into a parallel beam all particles with angles with respect to the main ring beam center line of $10^{\circ} \pm 14$ mr in the horizontal plane and $0^{\circ} \pm 9$ mr in the vertical plane. Particles of the selected momentum p_0 were then bent 6° by the first dipole bending magnet D_1 .

Quadrupoles Q_4 and Q_5 focused all beam particles of momentum p_0 horizontally at H_0 and, when the beam separators BS1 and BS2 were off, vertically at V (Figure A.1). To eliminate all particles

with momenta differing by more than 3% from p_0 from the beam lead was placed in the horizontal plane on either side of H_0 to form a momentum slit. The electrostatic beam separators BS1 and BS2 using crossed electric and magnetic field further improved the beam by vertically deflecting all particles of momentum p_0 with masses different from the antiproton mass. Lead above and below the vertical focus point V formed a mass slit and removed these particles (pions and kaons) from the beam. Pion background was reduced in this way by more than a factor of 50.

Dipole magnet D_2 was used to bend the beam to the short branch of the system. The sextupole S was not used. Dipole magnet D_3 was then used to further bend the beam away from the other (long) branch of the system and to bend low momenta particles created at the mass slit out of the beam. Finally, quadrupoles Q_6 and Q_7 focused the remaining beam at the target area.

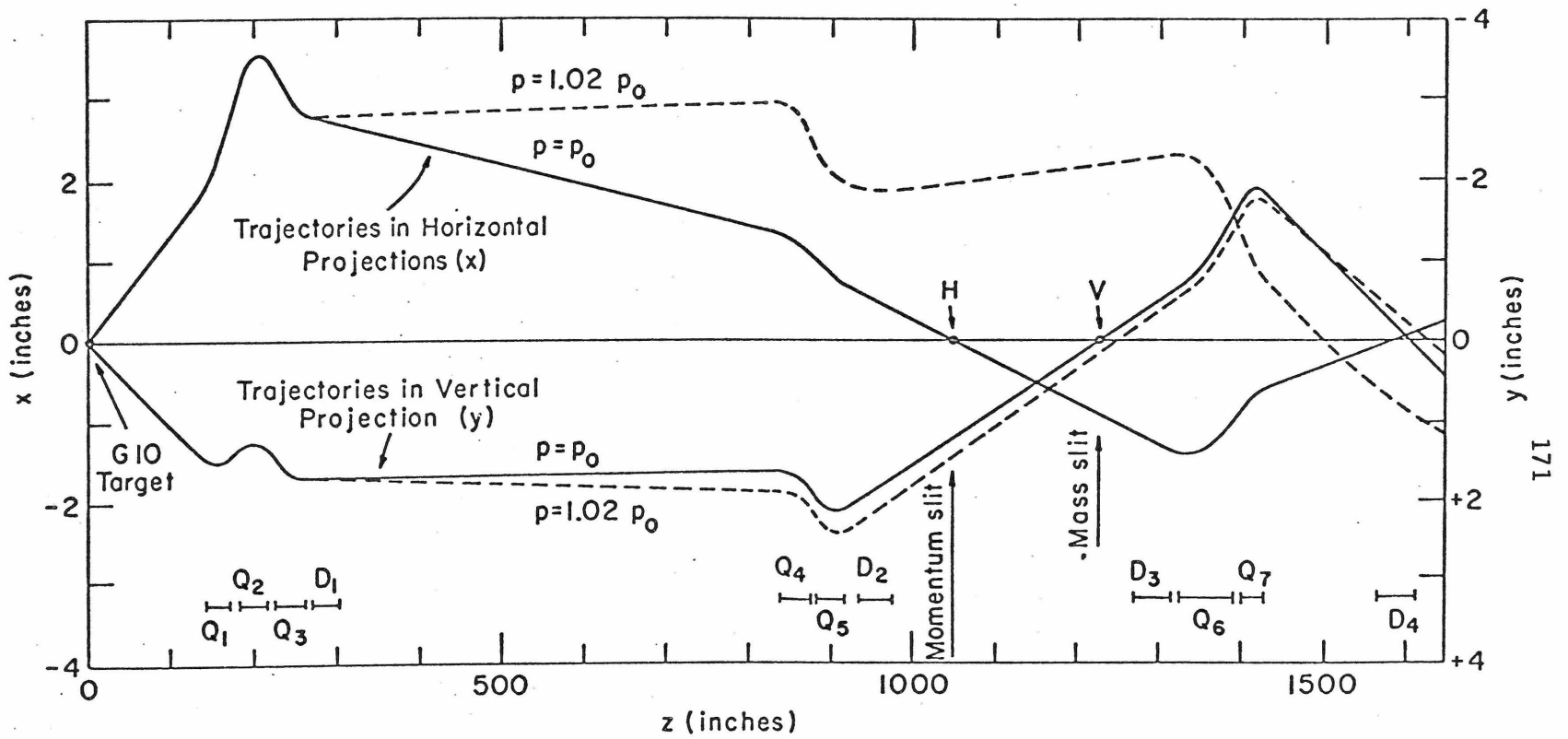


Figure A.1

Ray traces of the trajectories of extreme angle particles passing through the beam transport system.

Appendix B

The Wire Spark Chambers

B-1. Memory Time and D.C. Clearing Field

The memory time of a wire spark chamber is defined as the time during which the electrons and ions formed along the path of transit of a high energy particle through a chamber, lower the electrical resistance between the two wire planes of that chamber enough so a spark is produced at a point on that particle's path when the chambers are pulsed. It can be varied by applying DC electric fields of varying strength across the wire planes of the chambers since the higher the field, the sooner the ions are removed from the chamber and the shorter the memory time.

In this experiment a 17 volt DC clearing field was used and produced a memory time of about 1 μ sec in each chamber. Since the chambers were not pulsed until $\sim .3$ μ sec after a trigger producing event occurred, the memory time was required to be considerably greater than .3 μ sec; however, since there were the order of 200K beam and beam halo particles every 400 msec at the higher momenta on the average a beam particle traversed the chambers every 2-3 μ sec at these momenta. The 1 μ sec memory time produced by the 17 volt DC clearing field was considered an acceptable compromise.

To test whether the clearing field reduced the efficiency of the chambers, the delay before pulsing was artificially increased to 400 nsec. No decrease in efficiency was observed.

B-2. Recovery Time

After the chambers were pulsed and avalanche sparking occurred, electrons, ions and metastable atoms were produced along high energy particle transit paths through the chamber. If the chambers had been pulsed again before those particles were swept away, avalanche sparking would have occurred at the same points that sparking occurred in the initial pulsing. The time necessary for these particles to be swept away is called the recovery time.

Electron mobility in the neon helium gas mixture used in this experiment was of the order of $10^3 \text{ cm}^2/\text{sec-volt}$ giving a clearing time of 10 μsec for the 17 volts across the 1/4" gap.⁵⁴⁾ Ion mobility however, was much slower at $2-5 \text{ cm}^2/\text{sec-volt}$ giving clearing time of $\sim 10 \text{ msec}$ under the same conditions. To reduce this clearing time by a factor of 4 a pulsed clearing field of several hundred volts was applied to the chambers.

Metastable atoms stored residual discharge energy and could produce delayed ionization for 100 msec. However, the isopropanol vapor in the neon-helium gas mixture, which ionized easily, absorbed this energy from the metastable atoms and dissipated it in $\sim 10 \text{ msec}$.

B-3. Spark Formation and Track Resolution

The formation of a spark avalanche in a wire spark chamber was a complicated process and the position of the spark formation deviated from the actual path of the ionizing particle for many reasons. Gas composition, DC clearing field strength, delay between

event occurrence and chamber pulsing, and the angle of incidence of the ionizing particle all affected the spark formation position and the inherent resolution for particle tracks in the chamber.

The use of isopropanol alcohol in the gas composition restricted the spark avalanche to the region of primary ionization electrons along the path of the ionizing particle. To help compensate for shift in spark positions due to electron drift produced by the DC clearing field, the direction of the DC clearing field electric field vector was alternated for adjacent pairs of chambers.

In addition to the inherent track resolution limitations, the 1.25 mm wire spacing on the wire planes and the 10 megacycle digitizing frequency affected the over-all track resolution of the chambers. Since more than one wire could current couple to a spark and the coupling strength depended on proximity of the spark to the wire, the readout resolution was expected to be somewhat better than 1.25 mm.

Experimentally, the limitation on the over-all resolution was determined by the 10 megacycle digitizing scalars which quantized the position in steps of .52 mm. A study of the distribution of chamber sparks for straight beam tracks showed that the over-all track resolution (1 standard deviation from the mean beam line) of the wire spark chambers was $\sim .9$ mm.).

B-4. Two Track Resolution

Two track resolution was important in this experiment only in the upstream wire spark chambers (1-4) which had to support a

beam track and a backward scattered track. Factors affecting the two track resolution of the chambers were the width of the output signal from the magnetostrictive line pickup coils ($\sim 1 \mu\text{sec}$) and the ability of two sparks to form at close separations. In this experiment the over-all two track resolution was experimentally found to be $\sim 3.0 \text{ mm}$.⁵⁵⁾

Appendix C

PDP-8 Wire Spark Chamber Efficiency Calculation

The PDP-8 wire spark chamber efficiency calculation was performed separately for each set of 4 chambers (8 coordinates). This Appendix describes the details of this calculation for a given set of chambers.

Each event in a run was classified as an n spark event ($0 \leq n \leq 4$) where n was defined as the maximum number of sparks shared by at least two coordinates for that event. With the total number of n-spark events at the end of a run defined as $N(n)$ and the number of sparks on the i^{th} coordinated of the j^{th} n-spark event defined as $N_j^i(n)$, the efficiency of the i^{th} coordinate for an n-spark event was defined to be $e^i(n)$ where

$$e^i(n) = \frac{\sum_j N_j^i(n)}{n N(n)} .$$

When $N_j^i(n) > n$, $N_j^i(n)$ was set equal to n.

Appendix D

The Wire Spark Chamber Efficiency Calculation

When each wire spark chamber of a set of four comprising a trackfinding region was working efficiently, a particle traversing the sensitive area of each chamber produced 4 sparks which could be used for trackfinding in that region. Since, however, only three sparks were required to define a track in each region, inefficiencies in each chamber of a trackfinding region which were uncorrelated with inefficiencies in the other chambers of that region could be calculated from the pattern of missing sparks for several thousand reconstructed tracks. This procedure, described in detail below, was used to calculate the wire spark chamber efficiencies given in Table 2.5. Studies described in Section III-4 have shown that this calculation was good to within $\sim 1-2\%$. The reconstruction inefficiency correction described in Section III-4 includes the correlated wire spark chamber inefficiencies which have not been included in this calculation.

Define the following probabilities:

c_j = the probability that no spark occurs in chamber j ,

x_j = the probability that if a spark occurs in chamber j , coordinate x fails to record, and

y_j = the probability that if a spark occurs in chamber j , coordinate y fails to record.

c_j is actually the probability that a spark be below the threshold

for producing a pulse in the magnetostrictive lines for both x and y.

The following four patterns of events in four chambers are used in the efficiency calculation:

1. The number of events in which only one spark in one of the four x coordinates misses, but none of the y coordinates miss (N_{x_j});
2. The number of events in which only one spark in one of the four y coordinates misses, but none of the x coordinates miss (N_{y_j});
3. The number of events in which both the x and y coordinates of the same chamber miss (N_{xy_j}), and
4. The number of events in which neither of the coordinates of any of the chambers miss (N_4).

The ratios of N_{x_j} , N_{y_j} , and N_{xy_j} with N_4 can then be written in terms of the x_j , y_j and c_j and are given in equations D-1, D-2, and D-3.

$$\frac{N_{x_j}}{N_4} \equiv R_{x_j} = \frac{x_j \prod_{i \neq j}^4 (1 - x_i) \prod_{i=1}^4 (1 - y_i)(1 - c_i)}{\prod_{i=1}^4 (1 - x_i)(1 - y_i)(1 - c_i)} = \frac{x_j}{1 - x_j} \quad (D.1)$$

$$\frac{N_{y_i}}{N_4} = R_{y_i} = \frac{y_i}{1 - y_i} \quad (D.2)$$

$$\begin{aligned}
\frac{N_{xy_j}}{N_4} = Rc_j &= \frac{c_j \prod_{i \neq j}^4 (1 - c_i)(1 - x_i)(1 - y_i)}{\prod_{i=1}^4 (1 - c_i)(1 - x_i)(1 - y_i)} \\
&+ \frac{x_j y_j \prod_{i \neq j}^4 (1 - x_i)(1 - y_i) \prod_{i=1}^4 (1 - c_i)}{\prod_{i=1}^4 (1 - c_i)(1 - x_i)(1 - y_i)} \quad (D.3) \\
&= \frac{c_j}{(1 - c_j)(1 - x_j)(1 - y_j)} + \frac{x_j y_j}{(1 - x_j)(1 - y_j)} .
\end{aligned}$$

The horizontal coordinate, vertical coordinate, and correlated coordinate efficiencies are given below

$$(1 - x_j) = \frac{1}{1 + Rx_j} \quad (D.4)$$

$$(1 - y_j) = \frac{1}{1 + Ry_j} \quad (D.5)$$

$$1 - c_j = \frac{1}{\{[Rc_j - Rx_j Ry_j] (1 - x_j)(1 - y_j)\} + 1} \quad (D.6)$$

The wire chamber efficiencies could thus be calculated from the ratios Rx , Ry , and Rc_j .

The probability for finding a track in a given region (P_T) is the probability for finding at least three out of four sparks. It is

given by the equation

$$\begin{aligned}
 P_T = & \prod_{i=1}^4 (1 - c_i) \cdot \left[\prod_{j=1}^4 (1 - x_j) + \sum_{j=1}^4 \left(x_j \prod_{\ell \neq j}^4 (1 - x_\ell) \right) \right] \\
 & \left[\prod_{k=1}^4 (1 - y_k) + \sum_{k=1}^4 \left(y_k \prod_{m \neq k}^4 (1 - y_m) \right) \right] \quad (D.7) \\
 & + \sum_{j=1}^4 \left[c_j \prod_{i \neq j}^4 (1 - c_i) (1 - x_i) (1 - y_i) \right] .
 \end{aligned}$$

The first term of this equation is the probability that a spark formed in chamber j or chamber k failed to be recorded and the second term is the probability that no spark was formed in chamber j .

Appendix E

Annihilation Reaction Asymmetry Produced by a Polarized Proton Target

Let the beam travel in the +z direction and assume complete target polarization in the y direction. The eigenstates of σ_y are given by

$$|y\rangle = \frac{1}{\sqrt{2}} \left| \frac{1}{2} \right\rangle + \frac{i}{\sqrt{2}} \left| -\frac{1}{2} \right\rangle \quad (\text{E.1a})$$

$$|-y\rangle = \frac{1}{\sqrt{2}} \left| \frac{1}{2} \right\rangle - \frac{i}{\sqrt{2}} \left| -\frac{1}{2} \right\rangle. \quad (\text{E.1b})$$

Since a beam particle has an amplitude to be in a spin up state of $1/\sqrt{2}$ and an equal amplitude to be in a spin down state for an unpolarized beam, the amplitude to form a state in which an up spinning beam particle combined with a target particle polarized in the $\pm y$ direction is

$$\frac{1}{2} \left| \frac{1}{2} \right\rangle \left| \frac{1}{2} \right\rangle \pm \frac{i}{2} \left| \frac{1}{2} \right\rangle \left| -\frac{1}{2} \right\rangle \quad (\text{E.2a})$$

where the first bracket refers to the beam particle. The corresponding amplitude for a down spinning beam particle is

$$\frac{1}{2} \left| -\frac{1}{2} \right\rangle \left| \frac{1}{2} \right\rangle \pm \frac{i}{2} \left| -\frac{1}{2} \right\rangle \left| -\frac{1}{2} \right\rangle \quad (\text{E.2b})$$

Combining spin states in the usual way allows equations E.2a,b to be rewritten

$$\frac{1}{2} |1,1\rangle \pm \frac{i}{2} \left(\frac{1}{\sqrt{2}} |1,0\rangle + \frac{1}{\sqrt{2}} |0,0\rangle \right) \quad (\text{E.3a})$$

$$\frac{1}{2} \left(\frac{1}{\sqrt{2}} |1,0\rangle - \frac{1}{\sqrt{2}} |0,0\rangle \right) \pm \frac{i}{2} |1,-1\rangle . \quad (\text{E.3b})$$

Equations E3a,b are the two initial states which can be formed from an unpolarized beam and a polarized target. To obtain the cross section, the states $|1,1\rangle$, $|1,0\rangle$, and $|1,-1\rangle$ are replaced by the reaction amplitudes for $\bar{p}p$ annihilations into two pion or kaon final states $q_{11,00}$, $q_{10,00}$ and $q_{1-1,00}$, respectively. The state $|0,0\rangle$ is replaced by zero since the amplitude for these annihilations from an $s = 0$ initial $\bar{p}p$ state is zero. Then squaring the magnitude of the reaction amplitude for each initial state and adding, the cross section for the target polarized up (+ sign) or down (- sign) is found to be

$$\begin{aligned} \frac{d\sigma}{d\Omega} \uparrow\downarrow = & \frac{1}{4} |q_{11,00}(\theta, \varphi) \pm \frac{i}{\sqrt{2}} q_{10,00}(\theta, \varphi)|^2 \\ & + \frac{1}{4} \left| \frac{1}{\sqrt{2}} q_{10,00}(\theta, \varphi) \pm i q_{1-1,00}(\theta, \varphi) \right|^2 \end{aligned} \quad (\text{E.4})$$

Since the cross section without target polarization is

$$\frac{d\sigma}{d\Omega} = \frac{1}{4} |q_{11,00}(\theta, \varphi)|^2 + \frac{1}{4} |q_{10,00}(\theta, \varphi)|^2 + \frac{1}{4} |q_{1-1,00}(\theta, \varphi)|^2 \quad (\text{E.5})$$

Equation E.4 may be rewritten

$$\begin{aligned}
\frac{d\sigma}{d\Omega} \uparrow\downarrow &= \frac{d\sigma}{d\Omega} \pm \frac{i}{4\sqrt{2}} \{ q_{11,00}^* q_{10,00} - q_{10,00}^* q_{11,00} \} \\
&\pm \frac{i}{4\sqrt{2}} \{ q_{10,00}^* q_{1-1,00} - q_{1-1,00}^* q_{10,00} \}
\end{aligned} \tag{E.6}$$

Finally the asymmetry A is given by

$$\begin{aligned}
A &= \frac{\frac{d\sigma}{d\Omega} \uparrow - \frac{d\sigma}{d\Omega} \downarrow}{\frac{d\sigma}{d\Omega} \uparrow + \frac{d\sigma}{d\Omega} \downarrow} \\
&= \frac{\frac{i}{2\sqrt{2}} \{ q_{11,00}^* q_{10,00} - q_{10,00}^* q_{11,00} \} + \frac{i}{2\sqrt{2}} \{ q_{10,00}^* q_{1-1,00} - q_{1-1,00}^* q_{10,00} \}}{2 \frac{d\sigma}{d\Omega}}
\end{aligned} \tag{E.7}$$

Appendix F

Notation

This appendix gives a brief description of the notation used in this thesis. Particle notations are consistent with the 1970 Particle Property tables and are given below.

<u>Particle Group</u>	<u>Examples</u>	<u>Strangeness</u>	<u>I Spin</u>
Z*	Z ^{*++}	1	1
N*	N ¹¹ (1700)	0	1/2
Δ	Δ ⁺⁺ (1236)	0	3/2
Λ	Λ ⁰ (1115.6)	-1	0
Σ	Σ ^{+ 0 -}	-1	1

Regge trajectories are defined in terms of particles of a particular particle group. The notation given below is consistent with the notation used by Barger and Cline.

Signature τ is $(-1)^{J-1/2}$ for fermion trajectories and $(-1)^J$ for meson trajectories.

<u>Fermion Trajectory</u>	<u>Strangeness</u>	<u>I Spin</u>
Z*	1	1
N	0	1/2
Δ	0	3/2
Λ	-1	0
Σ	-1	1

In addition there are four types of poles depending on signature and parity.

<u>Type of Pole</u>	<u>Signature</u>	<u>Parity</u>
α	+	+
β	+	-
γ	-	-
δ	-	+

For example, fermion trajectories have

α, β poles with $J = 1/2, 5/2, 9/2, \text{ etc.}$

γ, δ poles with $J = 3/2, 7/2, 11/2, \text{ etc.}$

The notation $N(\bar{N})$ refers to a nucleon (antinucleon) and $M(\bar{M})$ to a meson (antimeson). In this work the symbol M used for a meson refers to a charged pion or kaon unless otherwise specified.

FOOTNOTES AND REFERENCES

1. D. Fong, Ph.D. thesis, California Institute of Technology, 1968.
2. Folded is used here to mean the summed cross sections $d\sigma/d\Omega(\theta) + d\sigma/d\Omega(\pi-\theta)$.
3. M.N. Focacci, W. Kienzle, B. Levrat, B.C. Maglic, and M. Martin, Phys. Rev. Letters 17, 890 (1966).
4. (k^-p) A.S. Carroll et al., Phys. Rev. Letters 23, 887 (1969).
 (k^+p) A.S. Carroll et al., Phys. Rev. Letters 21, 1282 (1969).
 (π^+p) A.S. Carroll et al., Phys. Rev. Letters 20, 607 (1968).
 ($k^\pm p \rightarrow pk^\pm$) A.S. Carroll et al., University of Rochester report UR-875-254 (1968).
5. R.J. Abrams et al., Phys. Rev. Letters 18, 1209 (1967).
6. E.W. Anderson et al., Phys. Rev. Letters 22, 1390 (1969).
7. M.N. Focacci et al., see Ref. 3.
8. B.Y. Oh et al., Phys. Rev. Letters 24, 1257 (1970).
9. R.J. Abrams et al., Phys. Rev. Letters 18, 1211 (1967).
10. L. Van Hove, Physics Letters 5, 252 (1963).
11. V. Barger and D. Cline, Physics Letters 25B, 415 (1967).
12. This is equivalent to the assumption that the trajectory can be represented as $\alpha = a + bu$ and the Regge residue γ is constant. See V. Barger and D. Cline, Phys. Rev. 155, 1792 (1967).
13. G.R. Lynch et al., Phys. Rev. 131, 1287 (1963).
14. J.W. Chapman et al., Phys. Rev. Letters 21, 1718 (1968).
15. R. Bizzarri et al., Istituto di Fisica dell'Università di Roma, Nota Interna No. 213, 1969 (unpublished).

16. The k^+p backward scattering has been fit by the exchange degenerate $\Lambda_\alpha, \Lambda_\gamma$ trajectory. S.K. Tewksbury, Ph.D. thesis, University of Rochester, 1969.
17. This beam was designed by B. Barish of Caltech and T. Kycia of Brookhaven National Laboratory. A beam with similar objectives has been designed and built at CERN, Fidecaro et al.
18. The terms upstream and downstream are in reference to the beam direction.
19. The liquid differential Čerenkov counter was constructed by B. Leontic and associates of BNL.
20. J.K. Yoh, Ph.D. thesis, California Institute of Technology (1970), p. 16.
21. S.K. Tewksbury, Ph.D. thesis, University of Rochester, 1969, p. 205.
22. Chronetic logic modules used in the fast logic were on loan from BNL High Energy Electronics Pool.
23. The wire spark chambers were constructed by J. Fischer of the Instrumentation Division of BNL. See J. Fischer "Digitized Spark Chambers in High Energy Physics", BNL report 11031.
24. This gate was designed by F. Lobkowicz of Rochester University.
25. The interfacing, digitizer, and PDP-8 programs were written by H. Pate and modified by A. Etenberg (Rochester University), B.C. Barish and A.V. Tollestrup.
26. The first stage analysis program was written by A.S. Carroll of BNL.

27. Copunctuality was defined by the equation

$$\text{Copunctuality} = \sqrt{\frac{\sum_{i=1}^3 (\vec{x}^i + \vec{e}^i a_i - \vec{a})^2}{3}}$$

where \vec{x}^i is $z = 0$ intercept of track i , \vec{e}^i is the unit vector of track i , and \vec{a} is the vertex for the three tracks. a_i and \vec{a} are obtained by solving the simultaneous equations

$$a_i = \vec{e}^i \cdot (\vec{a} - \vec{x}^i) \quad i = 1, 3$$

$$\vec{a} = \frac{1}{3} \left(\sum_{i=1}^3 a_i \vec{e}^i + \vec{x}^i \right) .$$

28. Coplanarity was defined by the equation

$$c = \frac{(\vec{e}_b \times \vec{e}_B)}{|\vec{e}_b \times \vec{e}_B|} \cdot \vec{e}_F$$

where \vec{e}_b is the unit vector of the beam track; \vec{e}_B is the unit vector of the backward scattered track; and \vec{e}_F is the unit vector of the forward scattered track.

29. In the plane of the scattering the forward scattered particle was required to be within 1 radian of the angle calculated from the angle of the backward scattered particle assuming a two pion or kaon final state annihilation reaction.
30. The Monte Carlo program was originally written by Yori Nagashima to calculate kp backward scattering experimental efficiencies and was later modified to do $\bar{p}p \rightarrow \pi\pi$ and $\bar{p}p \rightarrow kk$ annihilations.

31. The wire chamber efficiency calculation was worked out by A.S. Carroll of BNL.
32. π^{\pm} p cross section data were taken from "A Compilation of Pion-Nucleon Scattering Data", G. Giacomelli et al., CERN/HERA 69-1 and, S. Gasiorowicz "Elementary Particle Physics" (John Wiley and Sons, Inc., 1966, p. 306. Pion cross sections on carbon and aluminum are given in M. Crozon et al., Nuclear Phys. 64, 567 (1965).
33. R. J. Abrams et al., ref. 5.
34. D. Fong, ref. 1, pp. 132-133. These cross sections have been found by Fong to be too large by a factor of 2. All comparisons between Fong's cross sections and the cross sections obtained in this experiment have been made with Fong's cross sections divided by 2 and without the radiative correction ($\sim 6\%$).
35. J.W. Chapman et al., Ref. 14.
36. J.M. Blatt and L.C. Biedenharn, Rev. Mod. Phys. 24, 258 (1952), equation 3-14.
37. The constraints on quantum numbers are discussed in "Meson and Baryon Spectroscopy" by D.B. Lichtenberg (Springer-Verlag, New York, 1965).
38. S. Gasiorowicz "Elementary Particle Physics" (John Wiley and Sons, New York), p. 246, and "Elementary Particle Physics", G. Kallen (Addison-Wesley Pub. Co. Inc. 1964), p. 265.

39. S. Gasiorowicz, see Ref. 38, p. 336.
40. These Clebsh-Gordon coefficients are also given in J.M. Blatt and V.F. Weisskopf, "Theoretical Nuclear Physics" (John Wiley and Sons, 1952) p. 792.
41. Similar expression for the resonance amplitudes are used by Barger and Cline, Phys. Rev. 155, 1792 (1967). For details see W. Layson (Nuovo Cimento 27, 724 (1963) and J.D. Jackson, *ibid*, 34, 1644 (1964).
42. M.J.D. Powell, The Computer Journal 4, 303 (1965).
43. Energy dependent widths are discussed by S.L. Glashow, Physics Letters 2, 251 (1962) and J.D. Jackson, Nuovo Cimento 34, 1644 (1964). For short lived resonances which decay into two particles, the energy dependence of the partial ($\Gamma_{\alpha}(\omega)$) and total ($\Gamma(\omega)$) widths are given by

$$\Gamma_{\alpha}(\omega) \approx (\omega - \omega_0 + Q_{\alpha})^{\ell + 1/2}$$

and

$$\Gamma(\omega) \approx \Gamma_0 \left(\frac{q}{q_0} \right)^{2\ell + 1}.$$

In these equations $\Gamma = \sum_{\alpha} \Gamma_{\alpha}$, ω and q are total energy and final state particle momenta in the center of mass (subscript 0 means evaluated at the resonance energy), ℓ is the orbital angular momentum of the final state particles, and Q_{α} is the energy interval in which $\Gamma_{\alpha}(\omega)$ undergoes significant variation.

44. G. and S. Goldhaber in "Advances in Particle Physics" edited by Cool and Marshak, Interscience, New York (1968).
45. This argument was originally due to A.S. Carroll.

46. L. Schiff "Quantum Mechanics", 3rd ed. (McGraw Hill, New York),
p. 124.
47. S.C. Frautschi "Regge Poles and S Matrix Theory" (Benjamin Inc.)
1963; L. Van Hove, CERN Lecture 68.31 (1968)(unpublished).
48. See Ref. 4 for backward scattering data.
49. G.S. Abrams et al., Phys. Rev. Letters 21, 1407 (1968);
J. Banaigs et al., Nuclear Phys. B9, 640 (1969);
W. Busza et al., Rutherford Laboratory Preprint RPP/4/49 (1969);
C.T. Coffin et al., Phys. Rev. 159, 1169 (1967);
P.J. Duke et al., Phys. Rev. 166, 1448 (1968);
V. Cook et al., Phys. Rev. 129, 2743 (1963); and
C. Daum et al., Nuclear Phys. B6, 273 (1968).
50. See Ref. 21, Section 5-7.
51. Duality arguments may explain this agreement. See
R. Dolen, D. Horn and C. Schmid, Phys. Rev. 166, 1777 (1968).
52. A Regge cut gives neither the correct energy dependence nor
magnitude. C. Michael, University of Wisconsin Preprint
(Feb. 1969); submitted to Phys. Rev. Letters.
53. R.J. Abrams et al., Phys. Rev. Letters 19, 259 (1967).
54. The general properties of optical spark chambers are described
in O.R. Frisch (editor), "Progress in Nuclear Physics", vol. 9,
(MacMillan, New York, 1964), pp. 3-26.
55. Ref. 21, Section 2-8.